Electronic Properties of Atomically Precise Graphene Nanoribbons

Dissertertion

zur

Erlangung der naturwissenschaftlichen Doktorwürde

(Dr. sc. nat.)

vorgelegt der

Mathematisch-naturwissenschaftlichen Fakultät

der

Universität Zürich

von

Hajo Söde

aus

Deutschland

Promotionskomitee:

Prof. Dr. Thomas Greber (Vorsitz)

Prof. Dr. Leonhard Grill

Dr. Pascal Ruffieux (Leitung der Dissertation)

Zürich, 2015

I like friends who have independent minds because they tend to make you see problems from all angles.

Nelson Mandela, 1975

Abstract

This thesis presents a study on the growth and the electronic properties of several different classes of graphene nanoribbons (GNRs). The GNRs were studied primarily through low temperature scanning tunneling microscopy and spectroscopy (STM/STS) as well as non-contact atomic force microscopy (nc-AFM) measurements in ultra high vacuum conditions are presented.

Graphene nanoribbons are narrow stripes of graphene, which have been grown here via a bottom-up synthesis on crystalline gold surfaces. This bottom-up approach requires specifically predesigned monomer precursors, which fully determine the final structure. In this work, one known precursor was studied in more detail as well as two novel monomers are introduced. The growth of atomically precise armchair GNRs with seven carbon dimer rows in width has been analyzed in terms of polymerization temperature and ambient hydrogen and argon partial pressure. Determination of the activation energies of the involved reactions provides insight into the polymerization process, suggesting, in particular, an influence of imperfections of the gold(111) surface. Additionally, structural details and cross-coupling between GNRs have been studied. The two novel monomer precursor molecules both result in armchair GNRs with nine carbon dimer rows in width. In this case, all growth steps from the deposition of the initial precursor monomer to the final GNRs have been investigated, uncovering a partially cyclodehydrogenated polymer chain with high structural order. The successful fabrication of a second armchair GNR with high quality, finally supports the prediction that the bottom-up technique can indeed be used for the fabrication of GNR structures with various well-defined widths.

The electronic structures of the GNRs were unveiled by Fourier-transform STS, making use of scattering processes which occur at the termini. This technique makes it possible to probe a single structure whose chemical structure is precisely known, rather than averaging over several hundreds or thousands of structures of varying structural

quality, which is the case in various photoemission spectroscopy experiments. The electronic frontier bands have been observed and their analysis is in good agreement with density functional theory simulations. This means, that the newly fabricated $N = 9$ armchair GNR has indeed a band gap of a size which is highly interesting for electronic and optoelectronic applications. Ultimately, the utilization of Fourier-transform STS has proven to produce significant and reproducible results and it can be expected that it will be applied to other nanostructures in the future. The combination with theory further suggests that the decay of the wavefunction perpendicular to the surface needs to be taken into account for an accurate determination of the energy values of electronic states using STS. This and some other presented results could only be understood by the extensive combination of experimental work and theory

GNR heterojunctions have been synthesized using two different approaches. In the first approach, the temperature for cyclodehydrogenation was increased, leading to a random fusion of GNRs with sections of twice the regular width. In the second approach, the cyclodehydrogenation temperature is lowered, resulting in GNRs with sections that are cyclodehydrogenated on only one side, while in the other parts cyclodehydrogenation is complete. Analysis of the electronic structure of the heterojunctions revealed extremely sharp transitions of the electronic bands at the interfaces. The resulting electric field is about two orders of magnitude larger than in tradition semiconductor p-n junctions. GNR heterojunctions therefore have great potential to increase efficiency in numerous p-n junction devices.

Zusammenfassung

Diese Arbeit umfasst die Untersuchung der Herstellung und der elektronischen Eigenschaften von Graphenebändern (GNRs) mit armchair-Rändern und einer Breite von etwa einem Nanometer. Hauptsächlich Tieftemperatur-Rastertunnelmikroskopie und -spektroscopie (STM/STS) aber auch Nich-Kontakt-Rasterkraftmikroskopie (nc-AFM) Experimente im ultra-hoch Vakuum werden präsentiert.

Graphenebänder sind schmale Streifen des Basismaterials Graphene, welche in einer Bottom-up-Synthese auf einer kristallinen Goldoberfläche gewachsen werden. Dieser Bottom-up-Ansatz erfordert eigens designte Vorproduktmonomere, welche die Endstruktur vollständig bestimmen. In dieser Arbeit wurde ein bekanntes Monomer wurde ausführlicher untersucht und zwei neuartige Monomere für die Bottom-up-Synthese wurden vorgestellt. Das Wachstum der atomar genauen armchair GNRs mit sieben Kohlenstoffdimerreihen in der Breite wurde in Bezug auf die Polymerisierungstemperatur und den Umgebungspartialdruck von Wasserstoff und Argon hin überprüft. Die Bestimmung der Aktivierungsenergien der beteiligten Reaktionen erweitert das Verständnis des Polymerisierungsprozesses und legen insbesondere einen Einfluss der Fehlordnungen der Gold(111)-Oberfläche nahe. Zusätzlich wurden strukturelle Details und Querverbindungen zwischen GNRs untersucht. Die zwei neuartigen Monomere ergeben armchair GNRs mit neun Kohlenstoffdimerreihen in der Breite. Hier wurden alle Wachstumsschritte von der Ablagerung der Ausgangsmonomere auf der Oberfläche bis hin zur finalen GNR-Struktur erforscht, welches eine teildehydrierte Polymerkette mit hoher struktureller Ordnung hervorbrachte. Die erfolgreiche Herstellung eines zweiten armchair-Graphenebandes mit hoher Qualität, bestätigt nun die Vorhersage, dass die Bottom-up-Synthese tatsächlich eine Herstellung von Graphenebandstrukturen mit unterschiedlichsten, wohl-definierten Breiten möglich macht.

Die elektronische Struktur der GNRs wurde mittels Fourier-transformierter STS untersucht, welches sich die Streuungsprozesse an den Enden der GNRs zu Nutze

macht. Diese Methode macht es möglich einzelne Strukturen zu messen, dessen chemische Struktur exakt bekannt ist, anstatt über mehrere hunderte oder tausende Strukturen mit variierender struktureller Qualität zu mitteln, welchen der Fall ist in verschiedenen Spektroskopieexperimenten. Die elektronischen Grenzbänder wurden gemessen und analysiert und sind in guter Übereinstimmung mit Dichtefunktionaltheoriesimulationen. Dies bedeutet, dass das neu hergestellte $N = 9$ armchair-Grapheneband eine Bandlücke besitzt, welche von grossem Interesse sind für die Anwendung in der Elektronik und Optoelektronik. Schlussendlich hat sich die Verwendung der Fourier-transformierten STS gezeigt, dass diese sinnvolle und reproduzierbare Ergebnisse liefert und es kann daher erwartet werden, dass diese Technik in Zukunft auch auf andere Nanostrukturen übertragen wird. Die Verknüpfung mit der Theorie zeigt ausserdem, dass der Zerfall der Wellenfunktion senkrecht zur Oberfläche mit in Betracht genommen werdenmuss bei der korrekten Ermittlung von Energieweerten von elektronischen Zuständen mittels STS.

GNR-Heterostrukturen wurden mittels zwei unterschiedlichen Ansätzen hergestellt. Im ersten Ansatz wurde die Dehydrierungstemperatur erhöht, so dass sich zufällig GNRs verbinden, welches GNRs mit Abschnitten mit doppelter Breite zur Folge hat. Im zweiten Ansatz wurde die Dehydrierungstemperatur verringert, so dass die Dehydrierung unvollständig ist und somit einige Abschnitte der GNRs nur auf einer Seite dehydriert sind, während die anderen Abschnitte vollständig dehydriert sind. Die Analyse der elektronischen Struktur der Heterostrukturen offenbarte sehr scharfe Übergänge der elektronischen Bänder und den Grenzflächen. Das dort entstehende elektrische Feld ist etwas zwei Grössenordnungen grösser, als in traditionellen Halbleiter p-n Übergängen. GNR Heterostrukturen haben daher grosses Potential die Effizienz in unterschiedlichsten p-n Bauelementen zu erhöhen.

Preface

This work was realized within the framework of several research programs from the Swiss National Science Foundation, the European Science Foundation, The Office of Naval Research and BASF SE. This thesis is a report on the results that I have obtained during my time at the Swiss Federal Laboratories for Materials Science and Technology (Empa) under the supervision of Pascal Ruffieux. Most of the results have been or are about to be published in scientific journals and have been presented at several conferences and workshops, all of them are documented in the List of Publications on page 115.

This thesis makes use of high resolution scanning tunneling microscopy and spectroscopy and non-contact atomic force microscopy, all of which represent powerful techniques to determine structural as well as electronic properties of surfaces and adsorbates. The high degree of combining DFT simulations with the experimental work is the result of a close collaboration with Leopold Talirz.

Outline

Chapter 1 gives an introduction to the topic and discusses all relevant background knowledge.

Chapter 2 summarizes the most relevant aspects of the experimental techniques for the measurements performed during this thesis.

Chapter 3 investigates the synthesis of 7-AGNRs, 9-AGNRs and fused GNRs in detail and the structural features of the final structures.

Chapter 4 is concerned with the electronic properties of 7- and 9-AGNRs which were investigated in Chapter 4. The main focus was put on the measurements of

the electronic band structure using Fourier-transform scanning tunneling spectroscopy.

Chapter 5 presents the electronic band shifting in two GNR heterojunctions.

Chapter 6 summarizes the results obtained in the previous chapters. The results are reflected and open questions, that require further research to be answered, are pointed out.

Appendix A is a collection of small side projects and less successful experiments from which important conclusion were drawn.

Contributions by others

Several presented results are the outcome of collaborations and, hence, were not solely obtained by myself. Concerning the rationalization of the experimental findings within the frameworks of tight binding and DFT, the close and interactive collaboration with the atomistic simulations subdivision had been essential. In particular, all DFT-based modeling efforts were carried out by Leopold Talirz except the STM simulations that overlay Fig. 3.15(a) and (b), which were made by Prashant Shinde. Both precursor monomers for the fabrication of the 9-AGNRs were synthesized in the group of Klaus Müllen at the Max Planck Institute for Polymer Research. Other contributions are the following:

Chapter 3: The recipe for the 7-AGNR synthesis in Section 3.1 forms the starting point of this thesis and its description is therefore a review of previous works. The investigation into the termini and the growth conditions are, however, my own work with one exception: The STM and nc-AFM images in Fig. 3.4 were measured at the Physics department of the University of Basel together with Shigeki Kawai. The image in Fig. 3.17(b) was recorded by Shiyong Wang; The measurement of the Raman spectrum in Fig. 3.18(a) was recorded by Juan Ramon Sanchez-Valencia.

Appendix A: Section A.3 is about the decoupling of GNRs, where the relocation of GNRs onto monolayers of NaCl, KCl and graphene was tested. The fabrication of the graphene sample and the transfer of the 7-AGNRs onto it was done by Manuela Garnica from the Autonomous University of Madrid and Jinming Cai while the transferred 7-AGNRs were fabricated by myself. The STM measurements of the 7-AGNRs transferred onto the graphene sample were done jointly by Manuela Garnica and me.

Table of Contents

List of Figures

Notation and Measurement Parameters

The chapters, sections and subsections in the main body of this thesis are consecutively numbered. Deeper level sections are not numbered nor do they appear in the Table of Contents. Figure and table numbers start with the number of the chapter they are in, followed by a consecutive number.

If not mentioned otherwise, the time of any annealing is 10 minutes. The lock-in amplifier settings resulted in a 860 Hz sinusoidal modulation with peak-peak modulation of $\approx$ 56 meV. The image sizes are given in curly brackets at the end of the figure captions, or sub-captions for images of different sizes. Images showing topography have a black-grey-white scale, while images showing electronic maps have a black-purple-yellow-white scale. The measurement parameters for all shown, experimentally acquired images are given on pages XVIIIf. In molecular models carbon atoms are grey, hydrogen atoms are white and bromine atoms are red.

Below, the abbreviations and symbols used throughout this thesis are summarized.

Abbreviations

Ag	Silver
Au	Gold
CB	Conduction band
CO	Carbon monoxide
Cu	Copper
DBBA	10,10'-dibromo-9,9'-bianthryl
DBTP	3',6'-dibromo-1,1':2',1"-terphenyl
DITP	2',5'-diiodo-1,1':4',1"-terphenyl
FT-STS	Fourier-transform scanning tunneling spectroscopy
fcc	Face-centered cubic
GNR	Graphene nanoribbon
hcp	hexagonal close-packed
HOMO	Highest occupied molecular orbital
KCl	Potassium chloride
LDOS	Local density of states
LUMO	Lowest unoccupied molecular orbital
N-AGNR	$N = 7, 9$ armchair graphene nanoribbon
NaCl	Sodium chloride
nc-AFM	Non-contact atomic force microscope
PA	polyanthracene
RBLM	Radial-breathing-like mode
STM	Scanning tunneling microscope
STS	Scanning tunneling spectroscopy
UHV	Ultra high vacuum
VB	Valence band

Physical constants

a	Length of the armchair GNR unit cell [4.3×10^{-10} m]
d_{CC}	Carbon-carbon bond length in graphene [1.46×10^{-10} m]
e	Elementary charge [1.602×10^{-19} C]
$\hbar$	Reduced Planck constant [1.054×10^{-34} Js]
k_B	Boltzmann constant [8.617×10^{-5} $\frac{\text{eV}}{\text{K}}$]
m_0	Electron rest mass [9.109×10^{-31} kg]
α	Lattice constant of graphene [2.46×10^{-10} m]
ε_0	Vacuum permittivity [8.854×10^{-12} $\frac{\text{F}}{\text{m}}$]

Physical quantities

A	Oscillation amplitude [m]
$\frac{dI_t}{dV_B}$	Differential conductance $[\frac{\mathrm{A}}{\mathrm{V}}]$
E	Energy [J]
E_a	Activation energy [J]
E_F	Fermi energy [J]
E_{CB}	Energy of conduction band minimum [J]
E_{VB}	Energy of valence band maximum [J]
f_0	Resonance frequency [Hz]
I_t	Tunnel current [A]
$\mathbf{k}$	Vector in k-space $[\frac{1}{\mathrm{m}}]$
k_0	Stiffness $[\frac{\mathrm{N}}{\mathrm{m}}]$
$k_{x,y}$	x, y-component of $\mathbf{k}$
m^*	Effective mass [kg]
N and M	Quantity [1]
$n_{s,t}$	Local electron density of the substrate,tip $[\frac{1}{\mathrm{m}^3}]$
Q	Electric charge [C]
R_p	Propagation rate $[\frac{1}{\mathrm{s}}]$
R_t	Termination rate $[\frac{1}{\mathrm{s}}]$
$\mathbf{r}$	Vector in x-y-z-space [m]
T_p	Polymerization temperature [K]
t	Time [s]
V_B	Bias voltage [V]
V_{CG}	Coulomb gap voltage [V]
v_F	Fermi velocity $[\frac{\mathrm{m}}{\mathrm{s}}]$
x and y	Cartesian coordinates in-plane of the surface [m]
z	Cartesian coordinate perpendicular to the surface [m]
β	Growth probability [1]
γ_0	Hopping parameter [J]
Δf	Resonance frequency shift [Hz]
ϵ_j	Energy of the Kohn-Sham orbital ϕ_j [J]
κ	Inverse decay length $[\frac{1}{\mathrm{m}}]$
λ	Wave length [m]
Φ_{eff}	Effective potential [V]
Φ_{xc}	Exchange-correlation potential [V]
ϕ_j	Kohn-Sham orbital [V]
φ	Electric potential [V]

Measurement parameters

Figure 1.4	(a)	$V_B = 1.8$ V; $I_t = 0.3$ nA	spectra setpoint
Figure 2.2		$V_B = -1.0$ V, $I_t = 0.2$ nA	topography setpoint
Figure 3.1		$V_B = 2.1$ V, $I_t = 0.3$ nA	topography setpoint
Figure 3.4	(a)	$V_B = 0.1$ V, $I_t = 0.01$ nA	topography setpoint
	(b)	$f_0 = 23.57$ kHz, $A = 0.07$ nm	force image setpoint
	(c)	$V_B = 0.1$ V, $I_t = 0.01$ nA	topography setpoint
	(d)	$f_0 = 23.57$ kHz, $A = 0.07$ nm	force image setpoint
Figure 3.6	(a)	$V_B = 0.1$ V, $I_t = 0.01$ nA	topography setpoint
	(b)	$V_B = 0.1$ V, $I_t = 0.01$ nA	spectrum setpoint
	(c)	$V_B = 0.1$ V, $I_t = 0.01$ nA	topography setpoint
Figure 3.7	(a)	$V_B = 1.0$ V, $I_t = 0.2$ nA	topography setpoint
	(b)	$V_B = 1.0$ V, $I_t = 0.2$ nA	topography setpoint
	(c)	$V_B = 1.0$ V, $I_t = 0.2$ nA	topography setpoint
Figure 3.13	(a)	$V_B = 1.0$ V, $I_t = 0.2$ nA	topography setpoint
	(b)	$V_B = 0.1$ V, $I_t = 0.5$ nA	topography setpoint
Figure 3.14	(a)	$V_B = 0.5$ V, $I_t = 0.2$ nA	topography setpoint
	(b)	$V_B = 0.2$ V, $I_t = 0.05$ nA	topography setpoint
	(c)	$V_B = 0.2$ V, $I_t = 0.01$ nA	topography setpoint
	(d)	$V_B = -0.4$ V, $I_t = 0.2$ nA	topography setpoint
Figure 3.15	(a)	$V_B = 0.1$ V, $I_t = 0.05$ nA	topography setpoint
	(b)	$V_B = 0.05$ V, $I_t = 0.25$ nA	topography setpoint
	(c)	$V_B = 0.2$ V, $I_t = 0.01$ nA	topography setpoint
	(d)	$V_B = 0.1$ V, $I_t = 0.5$ nA	topography setpoint
Figure 3.16	(a)	$V_B = 0.2$ V, $I_t = 0.5$ nA	topography setpoint
	(c)	$V_B = 0.2$ V, $I_t = 0.5$ nA	spectrum setpoint
	(c)	$V_B = 1.0$ V, $I_t = 0.5$ nA	topography setpoint
Figure 3.17	(a)	$V_B = 0.1$ V, $I_t = 0.5$ nA	topography setpoint
	(b)	$f_0 = 23.57$ kHz, $A = 0.07$ nm	force image setpoint
	(c)	$V_B = 0.05$ V, $I_t = 0.08$ nA	topography setpoint
Figure 3.18	(a)	$\lambda = 785$ nm	laser wave length
Figure 3.19	(g)	$f_0 = 23.57$ kHz, $A = 0.07$ nm	force image setpoint
	(h)	$f_0 = 23.57$ kHz, $A = 0.07$ nm	force image setpoint
Figure 4.1	(b)	$V_B = 3.0$ V; $I_t = 0.6$ nA	spectra setpoint
	(c)	$V_B = 0.01$ V; $I_t = 0.01$ nA	topography setpoint
	(d)	$V_B = -1.5$ V; $I_t = 0.2$ nA	spectra setpoint

Measurement parameters (continued)

Figure 4.3	(a)	$V_B = 3.0$ V; $I_t = 0.6$ nA	spectra setpoint
	(b)	$V_B = 1.9$ V; $I_t = 0.4$ nA	spectra setpoint
Figure 4.9	(a)	$V_B = -1.6$ V; $I_t = 0.3$ nA	spectra setpoint
	(c)	$V_B = 2.7$ V; $I_t = 0.6$ nA	spectra setpoint
Figure 4.12		$V_B = 2.7$ V; $I_t = 0.6$ nA	spectra setpoint
Figure 4.13	(a)	$V_B = 2.5$ V, $I_t = 0.3$ nA	conductance setpoint
		$V_B = 2.5$ V, $I_t = 0.3$ nA, $z = z_0 + 0.2$ nm	constant z setpoint
	(b)	$V_B = 1.8$ V, $I_t = 1.0/3.0$ nA	spectra setpoint
	(c)	$V_B = 1.8$ V, $I_t = 3.0$ nA	spectra setpoint
Figure 4.16		$V_B = -0.5$ V; $I_t = 10.0$ nA	spectra setpoint
Figure 4.17	(a)	$V_B = -1.5$ V; $I_t = 10$ nA	spectra setpoint
	(c)	$V_B = 2.5$ V; $I_t = 0.8$ nA	spectra setpoint
Figure 5.1	(a)	$V_B = 1.8$ V, $I_t = 0.2$ nA	topography setpoint
	(c)	$V_B = 1.9$ V, $I_t = 0.4$ nA	spectra setpoint
	(d)	$V_B = 1.9$ V, $I_t = 0.4$ nA	spectra setpoint
Figure 5.2	(a)	$V_B = 1.9$ V; $I_t = 0.4$ nA	spectra setpoint
Figure 5.3	(a)	$V_B = 1.9$ V; $I_t = 0.5$ nA	spectra setpoint
Figure 5.4		$V_B = 1.8$ V; $I_t = 0.3$ nA	spectra setpoint
Figure 5.5	(a)	$V_B = -1.0$ V; $I_t = 0.1$ nA	topography setpoint
	(c)	$V_B = -1.0$ V, $I_t = 0.3$ nA	spectra setpoint
Figure A.1	(a)	$V_B = 0.2$ V; $I_t = 0.01$ nA	topography setpoint
	(b)	$V_B = 0.2$ V; $I_t = 0.01$ nA	topography setpoint
Figure A.2		$V_B = 2.7$ V; $I_t = 0.6$ nA	spectra setpoint
Figure A.4	(a)	$V_B = -1.5$ V, $I_t = 0.3$ nA	topography setpoint
	(b)	$V_B = -1.5$ V, $I_t = 0.3$ nA	topography setpoint
Figure A.5	(a)	$V_B = -0.8$ V, $I_t = 0.02$ nA	topography setpoint
	(b)	$V_B = -1.0$ V, $I_t = 0.15$ nA	topography setpoint
	(c)	$V_B = 0.05$ V, $I_t = 0.015$ nA	topography setpoint
Figure A.6	(a)	$V_B = -1.0$ V, $I_t = 0.05$ nA	topography setpoint
	(b)	$V_B = -1.5$ V, $I_t = 0.02$ nA	topography setpoint
	(c)	$V_B = -1.0$ V, $I_t = 0.04$ nA	topography setpoint
Figure A.7	(a)	$V_B = -1.0$ V, $I_t = 0.04$ nA	topography setpoint
	(b)	$V_B = -3.0$ V, $I_t = 0.04$ nA	topography setpoint
	(c)	$V_B = -1.0$ V, $I_t = 0.04$ nA	topography setpoint

Chapter 1

Review

1.1 Introduction

The industrial revolution began with the introduction of steam-powered technology. The transition of hand production methods to machines was set into motion. This new technology transformed the printing industry into the primary communication and information industry because it greatly increased the speed of printing and significantly reduced the cost. The second industrial revolution that introduced combustion engines enabled the beginning of mass production. This made it possible to introduce electrical communication technology. Telephone lines were installed, and radio and television were introduced, creating a communication grid that recast social life. Today, the technological advancement has let to yet another drastic change in the communication and information sector. The modern computer-based information technology has already changed the communication industries with significant impact on our everyday life. This technology has the potential to trigger fundamental changes in all different kind of industries. The changes that are happening today, are sometimes already called the third industrial revolution [1].

The modern information technology is based on the rapid growth of processing power in computer chips. Since the 1960's this rapid growth has substantially kept pace with Moore's law. Gordon Moore predicted that the number of transistors that can be placed inexpensively on an integrated circuit is doubled approximately every two years [2]. Mainly due to miniaturization of transistors, it has been possible that Moore's law proves valid until today. For the past 50 years the end of such rapid advancement has been proposed many times due to allegedly insurmountable obstacles. With commercially available feature sizes of 22 nm and fabrication plants using 14 nm-technology in construction [3], a new obstacle is rapidly approaching: With

feature sizes approaching 5 to 7 nm, it will be difficult to operate transistors utilizing the traditional CMOS design since quantum tunneling through the transistor channel will occur. This constitutes a fundamental physical limit and might mark the end of the silicon-era in information technology. And it might be reached within the next ten years.

Going beyond this limit requires the use of new concepts and materials. Besides allowing a further miniaturization of devices, novel concepts like molecular electronics, spintronics [4] or quantum computation [5] may be employed. The latter would be able to ultimately increase computational performance by going beyond the boolean on/off paradigm. All of these concepts require at least a partial rejection of silicon. One material that has the potential to be used in post-silicon electronic devices is graphene. The discovery of this single sheet of carbon earned Andre Geim and Konstantin Novoselov the Nobel prize in physics in 2010. The discovered mechanical and electronic properties were outstanding and triggered a massive amount of research into this novel material. However, all these properties do not make graphene an ideal candidate in electronic switching devices per se. As a semimetal, it is a zero band gap semiconductor and hence only useful in transporting information but not processing them. Reducing the feature size of a graphene structure to a few nanometers, induces quantum effects which prevail the functionality of a device. As a result, graphene nanostructures may have band gaps [6, 7], carry spin states [8] or even behave like a magnet [9] without significantly compromising the outstanding bulk properties. All these effects depend on the size, shape and the chemical structure of the edges.

The major obstacle for the experimental investigation into such structures is the synthesis. As quantum effects can be altered by adding, removing or substituting single atoms within a nanostructure, it is of critical importance to have full control over the exact structure of the final nanostructure. The top-down method, that has been utilized in the fabrication of many nanometer sized structures, cannot provide the required precision. There are, for example, numerous ways of fabricating carbon nanotubes, but non of them has the capability of controlling the exact diameter and other structural properties [10]. Only very recently a bottom-up approach was able to achieve a controlled synthesis of selective carbon nanotubes [11]. The bottom-up method uses specifically designed molecules as building blocks for creating nanostructures. Despite these simple instructions, the large scientific interest into bottom-up fabricated nanostructures started only a couple of years ago [12–16].

The possibility of the bottom-up fabrication of nanostructures, which make use of graphene's outstanding properties, is the technological motivation for the work on graphene nanoribbons presented in this thesis.

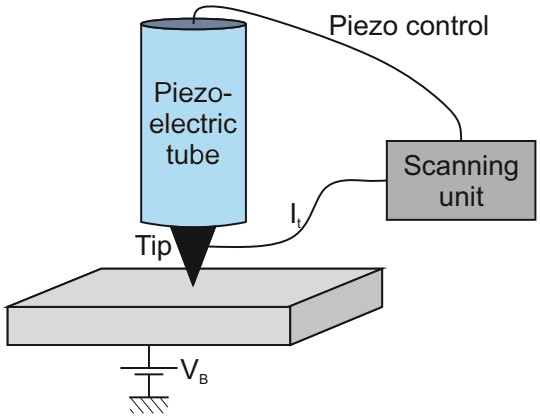

Figure 1.1 Schematic of an STM showing the main components.

1.2 Scanning tunneling microscopy

In 1959, later Nobel laureate Richard Feynman gave a talk with the title: There's Plenty of Room at the Bottom. This talk is considered path-breaking in the development of nanotechnology. Feynman presented ideas of microscopes than could see small molecules and of technological prospects if one would be able to manipulate matter at the atomic scale. He proposed that when device sizes reach the region of quantum mechanics, unprecedented functionalities would be achieved. The vision of Feynman came to reality with the invention of the scanning tunneling microscope (STM) by Binnig and Rohrer in 1982 [17], which allowed the imaging of single atoms and the ability to move them around as demonstrated by Eigler in 1990 [18].

This technique is a real space, nanoscale imaging method utilizing electron tunneling between a sharp tip and the sample whose surface is imaged. A schematic diagram of a scanning tunneling microscope (STM) is shown in Fig. 1.1. The main features are: the piezoelectric tube, which holds the tip and allows controlled nanoscale movements; the scanning unit, which controls the measurement and collects the data; and the feedback loop, which keeps the tip at a constant distance from the sample.

1.2.1 Imaging using tip-sample tunneling

Electron tunneling is a quantum mechanical phenomenon forbidden in classical mechanics. It denotes electrons traveling between two electrodes trough an insulating barrier. In an STM the electrodes are the tip and the sample; these must be conductors and/or semiconductors. There is a finite probability of electrons traveling through the classically impenetrable barrier due to their wave-like nature, which leads to the electron wave functions of tip and sample decaying into the barrier. A narrow

enough barrier allows the wave functions to overlap enabling electron tunneling. The application of a bias voltage results in the flow of a tunnel current.

In the simplest case, the electron tunneling may be mathematically described by a one-dimensional rectangular potential barrier. This problem is extensively discussed in most introductory books on quantum mechanics. A more thorough theoretical treatment of the tunneling phenomenon for a small electron transmission barrier may be applied using time dependent perturbation theory [19]. The Wentzel-Kramers-Brillouin approximation gives an expression for the transmitted tunnel current I_t, which relies on the distance z between the electrodes and the local densities of states of the substrate n_s and the tip n_t [20]. This solution may be written as:

$$I_t = \int_0^{eV} n_s(E)\, n_t(-eV_B + E)\, T(z) dE, \tag{1.1}$$

where $T(z) \propto \exp(-2\kappa z)$, κ denotes the inverse decay length of the electron wavefunctions at the sample, e the elementary charge, V_B the bias voltage and E the energy relative to the Fermi energy E_F. From this treatment it can be seen that, assuming n_t is constant for a metal tip, the local density of states (LDOS) at energy E of the surface is detected and contributes to the measured tunnel current in the STM. The tunneling properties of a specific tip-sample system are represented by $\kappa = \sqrt{\frac{2m_e\hat{E}_t}{\hbar^2}}$, which comprises the average work function of the tip and sample in the tunneling barrier $\hat{E}_t$.

The tip is positioned at a certain distance above the surface and a tunnel current is thus established. The tunneling current is exponentially dependent on the distance between tip and surface, so any change in distance induces a large difference in I_t, which can be measured experimentally.

The STM tip raster-scans the surface, while the x-y-z motion is controlled with a piezo-scanner. An electronic feedback loop is established which prevents the tip from crashing and keeps the spacing z constant at about 0.5 nm and with it I_t at its set value. The acquired z data is used to make topographic images. This feedback loop assisted scanning technique is called constant-I_t mode. A second option, which is usually only used together with spectroscopy experiments, is to let the tip scan across the surface on a fixed plane parallel to the surface. This way I_t changes according to the corrugation underneath the tip. As the tip only moves in x and y directions, it is called constant-z mode.

There are, however, some drawbacks in the described method. STM generally has a poor time resolution. The scan speed has to be slow enough that the feedback has sufficient time to adjust the tip to the height differences while scanning. That is why recording an image with a resolution of 300 $\times$ 300 points takes about 5 minutes.

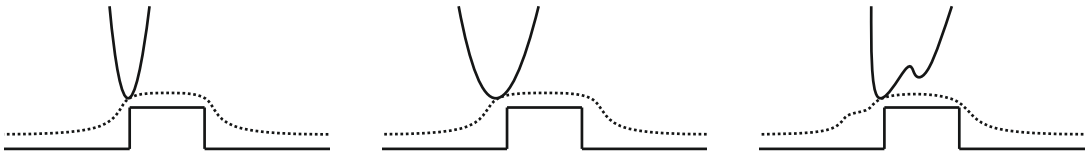

(a) Sharp tip **(b)** Blunt tip **(c)** Double tip

Figure 1.2 Effect of tip shapes on STM images. (a) A sharp tip can move across the surface and pick out small features in the surface. (b) A blunt tip cannot accurately trace the surface topography. (c) A double tip effectively images the sample twice resulting in ghost features.

Probably the biggest demerit of STM is the lack of chemical sensitivity. It is almost impossible to identify atoms as elements or the chemical structure of molecules using STM.

Tip shape

An ideal tip terminates in a single atom. As the measured tunnel current depends exponentially on the tip-sample spacing, atoms further away from the surface than the terminal tip atom will contribute negligibly to the overall tunneling current. The macroscopic geometry of the tip also has a direct effect on the images obtained. A sharp tip is desirable in order to clearly resolve surface corrugations, as shown in Fig. 1.2(a). STM image resolution is lower if the tip has a blunt apex, as in Fig. 1.2(b), because the tip cannot accurately trace the surface corrugation in detail and images appear blurred. If images of the surface contain lots of identical ghost features, and large surface features such as step edges and adsorbates appear to have a twin shadow, the tip most likely has a double tip end, as shown in Fig. 1.2(c). In this case tunneling occurs first through the tip end closer to the sample, then when that tip end has passed the step edge, tunneling occurs through the second tip end. However, the resulting tip shape is purely random.

Tips can become contaminated by attracting loosely bound adatoms or molecules which are then dragged across the surface. The tip may be cleaned by passing a voltage pulse through it or lightly crashing the tip into the surface to remove any adhered adatoms. These kind of conditioning can also change the profile of the tip end and may remove a double tip, or cause the tip to become sharper.

1.2.2 Organic molecules

When imaging organic molecules adsorbed on a metallic surface, the electron tunneling occurs between the tip and the occupied or unoccupied molecular orbitals. As STM provides a representation of the LDOS of a surface, one can determine an individual molecules by examining its representation in an STM image. The imaged shape of the molecule is the shape of the the lowest unoccupied molecular orbital (LUMO) and the highest occupied molecular orbital (HOMO) for positive and negative sample bias voltages, respectively. However, interaction with the surface can lead to changes in the electronic structure. Within the gap between the LUMO and HOMO levels, the shape of the molecule is still imaged. This is due to a changed decay of the metal states in the presence of the molecule. Therefore not only the electronic properties of the free organic molecule but the entire adsorbate-surface system has to be considered carefully for interpretation. This is especially relevant for flat molecules. The effects of the surface will be described in more detail in the following section.

1.3 Scanning tunneling spectroscopy

The STM is a versatile tool not only to get information about the geometry of a surface and adsorbed molecules, but also about the electronic structure and dynamic processes. Several parameters can be measured and controlled in addition to the position on the sample (x-y): tunneling current (I_t), bias voltage (V_B), time (t) and tip-sample distance (z). In latter one, only differences in z can be measured accurately, the absolute value is not accessible and can only be estimated. Depending on which parameters are kept constant and which ones are varied several different physical properties of the surface and its adsorbents can be derived. The measurements can be performed on a single point, points along a line or on a grid of points. This technique of gaining insight into various properties is commonly known as scanning tunneling spectroscopy (STS). In order to obtain spectroscopy curves at specific locations, the tip of the STM is fixed over the desired location on the surface. At this position one of the initial parameters is varied while one or more of the other parameters are measured simultaneously. Despite the various option, mainly three spectroscopy types are used:

- Current-voltage, $I_t(V_B)$, spectroscopy is used to determine the electronic properties of a surface and its adsorbents. Usually at a fixed tip-surface distance, V_B is modulated while I_t is recorded. This way it is possible to gain information on the LDOS, which is proportional to the differential conductance $\frac{dI_t}{dV_B}(V_B)$.

- Time-resolved current, $I_t(t)$, spectroscopy is used to investigate dynamic effects on a surface. Any dynamic event in the proximity of the tip is reflected in I_t. The time resolution of $I_t(t)$ spectroscopy is in the order of μs.
- Current-distance, $I_t(z)$, spectroscopy is used to estimate the work function of a surface and the barrier height of the tip-sample junction.

In this work, STS was solely used to determine electronic properties and, hence, in the following only for $I_t(V_B)$ spectroscopy a theoretical background will be given and its experimental realizations explained.

1.3.1 Current-voltage spectroscopy

The most common use of $I_t(V_B)$ spectroscopy is the determination of $\frac{dI_t}{dV_B}$. As it can be seen from Equation 1.11, $\frac{dI_t}{dV_B}$ gives information about the LDOS at a particular point on the sample. In principle, the measurement of the $I_t(V_B)$ dependence followed by a numerical derivation would be sufficient. However, even a tiny background noise in the signal can have a crucial effect on the obtained $\frac{dI_t}{dV_B}$. The quality can be improved greatly by using a lock-in amplifier, which allows a direct measurement of $\frac{dI_t}{dV_B}$ and higher order derivatives.

A small, high frequency sinusoidal voltage is superimposed onto the constant V_B. The frequency is chosen higher than the bandwidth of the feedback loop, so that the z-positioning of the tip is not affected. The varying component of I_t is recorded, and the component in-phase with the sample bias modulation yields $\frac{dI_t}{dV_B}$ directly. Another major advantage of using a lock-in amplifier is the possibility of recording complete LDOS maps simultaneously to the topographic images.

Typically, for STS measurements the feedback loop, that automatically adjusts the z-position of the tip, is switched off. This leaves the z-direction of the tip fixed and freezes the tip-sample spacing. In particular, this is necessary when crossing $V_B = 0$, which would cause a feedback controlled tip to crash into the surface. A schematic of such an STS experiment is shown in Fig. 1.3. For large voltage ranges, I_t may vary over several orders of magnitude. This cannot be captured by the electronics and for such cases the feedback loop must not be turned off.

Instead of recording single spectra at specific positions, electronic states at a specific energy can be mapped simultaneously to a topography measurement. The lock-in amplifier needs an integration time in the order of 20 ms, which in this case constrains the minimum time the tip is placed at each measured position. The maps of electronic states at specific energies allow to reveal their location within the resolution limit of the STM.

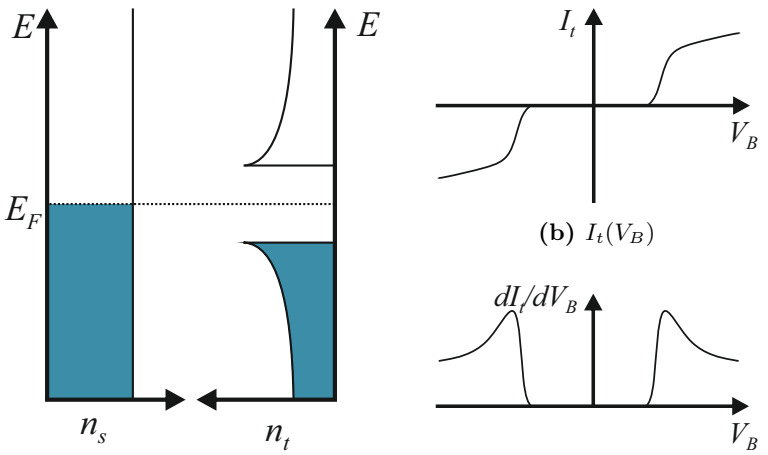

(a) n_s and n_t **(b)** $I_t(V_B)$ **(c)** $\frac{dI_t}{dV_B}(V_B)$

Figure 1.3 STS of a semiconducting organic molecule. (a) The sample shows an electronic gap around E_F, while n_t is assumed constant. An applied V_B would increase or lower E_F.(b) Corresponding $I_t(V_B)$-curve: I_t is zero for small V_B, since there are no states available electrons could tunnel into. When passing an electronic state the current raises due to the now available tunneling channels in the sample. The actual onset of the current is shifted closer to E_F because of a finite temperature and experimental limitations. (c) The derivative of the $I_t(V_B)$-curve in (b) reproduces the broadened LDOS.

Influence of the surface on organic molecules

The underlying substrate has several influences on the STS experiments on organic molecules. In flat molecules, the electronic structure of the surface can be seen through the molecule. The STS spectra then show components of both, the organic molecule and the surface. An example with a single-atomic layer flat 7-AGNR on a Au(111) surface is shown in Fig. 1.4(a) (see Section 1.6 for more information on the organic structure). The most pronounced electronic state is the Au(111) surface state at about 0.45 eV. This states also appears in the spectra taken on top of the 7-AGNR. The intensity of the surface state is in fact higher than on top of the Au surface itself. This proves an extension of the decay distance of the surface state's wave function through the 7-AGNR. Another observation is the energetic shift of the state towards E_F by about 0.15 eV. This shift can be observed by using angle-resolved photoemission spectroscopy, too, which excludes it from being a sole effect of the STS technique [21].

Another major influence of the surface arises when measuring the energetic positions of the electronic states by STS. When an organic molecule is near a metal surface a correlation effect called surface screening takes place which changes the surface po-

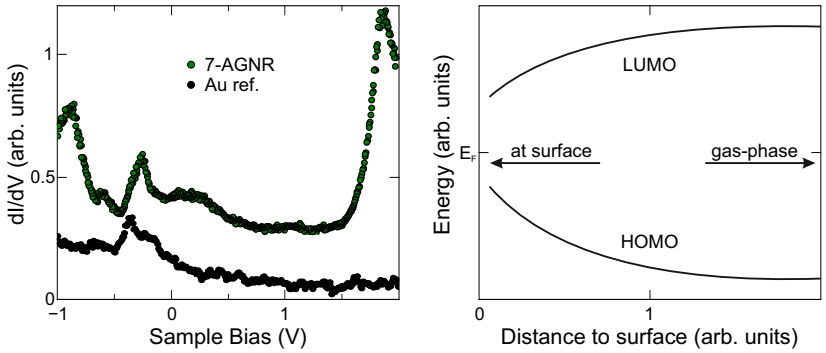

(a) Surface states in spectra **(b)** Surface polarization

Figure 1.4 Contributions of a metal surface in STS. (a) Two $\frac{dI_t}{dV_B}(V_B)$ spectra recorded on a 7-AGNR (green) and on the Au(111) surface for reference (black). (b) Scheme illustrating the evolution of the HOMO and LUMO levels as a function of the metal surface-molecule distance, due to image charges and a potential at the interface.

tential and at the same time the energy levels of the molecular orbitals. A way of illustrating how the HOMO and LUMO levels shift as a function of the metal surface-organic molecule distance is to consider the definitions of the LUMO and HOMO levels, which are defined by

$$E_{HOMO} = E(N) - E(N-1); \tag{1.2}$$

$$E_{LUMO} = E(N+1) - E(N), \tag{1.3}$$

where $E(N)$ is the ground state energy of the system with N electrons. When measuring the HOMO, an electron in extracted from the system, which adds a positive charged hole to the system. This extra positive charge induces an opposite image charge in the metal, adding an extra contribution to $E(N-1)$ which can be approximated by $\frac{e^2}{4d_{ms}}$, with molecule-surface distance d_{ms} [22]. This indicates that the initial HOMO level E_{HOMO} is shifted up by surface potential effects. Similarly, the LUMO level, E_{LUMO}, is shifted down due to an extra contribution of approximately $-\frac{e^2}{4d_{ms}}$. This simple argument shows that the organic molecule energy gap on a metal surface is reduced as a function of metal surface-organic molecule distance as illustrated in Fig. 1.4(b).

Another influence of the surface on the electronic structure of organic molecules is indicated in Fig. 1.4(b): the shift of the molecular E_F. In the gas-phase, E_F of an organic molecule is described by the charge neutrality level, which is a marker of the direction and magnitude of charge transfer to other materials. It is therefore similar

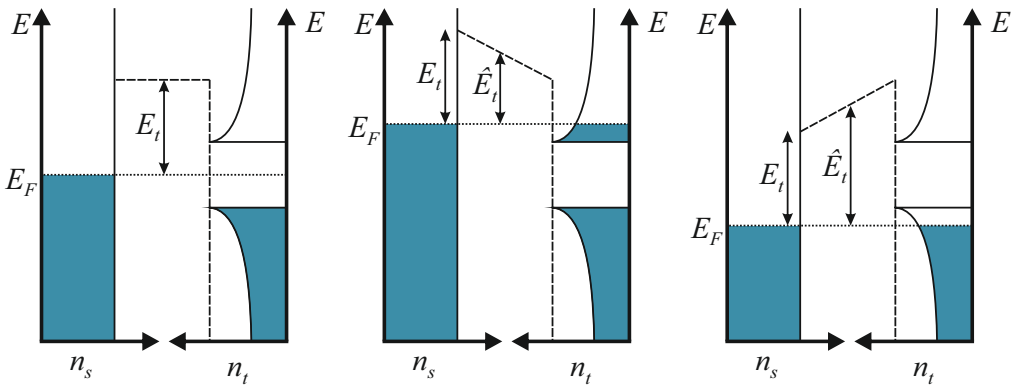

(a) $V_B = 0$ **(b)** $V_B > 0$ **(c)** $V_B < 0$

Figure 1.5 Average tunneling barrier. (a) The is a tunneling barrier E_t between tip and sample, which hinders tunneling. (b) Measuring the unoccupied states lowers $\hat{E}_t$, the average tunneling barrier. (c) Measuring the occupied states increases $\hat{E}_t$.

to Paulings electronegativity [23]. In most organic molecules, the charge neutrality level can be approximated reasonably well by the midgap energy. However, in the case of tetracyanoquinodimethane (TCNQ), e.g., which has two groups with strong electrophilic character, the charge neutrality level is closer to the LUMO level than the mid gap energy [22, 24–26]. The direction and magnitude of charge transfer at a organic molecule-metal interface, is determined by the difference between the charge neutrality level and E_F of the metal surface. This induces a potential difference, which shifts the positions of the molecular E_F level with respect to the charge neutrality point.

In Fig. 1.4(a), it can be observed, that states of the 7-AGNR are measured with various intensity. There are several reasons for different $\frac{dI_t}{dV_B}$ intensities of different states. A major one is a difference in the decay of the electronic state's wave function in z-direction. This will be demonstrated by experiments and computational simulations in Section 4.1.4. A more general effect when measuring structures with a band gap is illustrated in Fig. 1.5. The spectra of the exemplary STS experiment in Fig. 1.3 assumes the absence of a tunneling barrier. In experimental spectra this finite tunneling barrier changes the measured intensity depending on the shape of n_s and n_t. The effective tunneling barrier $\hat{E}_t$ is lowered when $V_B < 0$ and the current flows from the tip with a constant n_t to the molecule with a gap in n_s (Fig. 1.5(b)). On the other hand, $\hat{E}_t$ is raised when measuring the occupied states with $V_B < 0$ (Fig. 1.5(c)). A tunneling barrier hinders tunneling by increasing $\kappa = \sqrt{\frac{2m_e\hat{E}_t}{\hbar^2}}$ and thus decreasing I_t

as evidenced by Equation 1.1. Consequently, the measured intensities are generally lower for the occupied states.

1.4 Non-contact atomic force microscopy

Numerous surfaces have been imaged with atomic resolution using STM. The atomic structure of an individual molecule, however, cannot be resolved as STM images the frontier molecular orbitals, which are caused by, but do not resemble, the chemical structure. The information about frontier molecular orbitals is of great importance, because it reflects the electronic properties of the molecule. In order to image the chemical structure, the inner electrons with energy levels much lower than E_F would have to be probed, as they reveal the positions of single atoms and bonds between them.

Non-contact atomic force microscopy (nc-AFM) is based on a similar scanning probe approach as STM, however relies on a different interaction between tip and sample. The tip is mounted on a mechanical resonator, see Fig. 1.6, which oscillates at its resonant frequency f_0. The main observable is the frequency shift Δf of the resonance, which arises due to the forces acting between tip and sample. It is used as imaging signal of the forces when mapping an x-y plane. In the first approximation, the functioning of a nc-AFM can be understood in terms of a force-gradient model [27]. According to this model, in the limit of small amplitudes, a tuning fork approaching a sample undergoes a shift, Δf, in its natural frequency, f_0 by

$$\Delta f = -\frac{f_0}{2k_0}\frac{\partial F(z)}{\partial z}, \tag{1.4}$$

where k_0 is the nominal stiffness of the tuning fork in the presence of a force gradient $\frac{\partial F(z)}{\partial z}$ that arises due to the tip-sample interactions. Chemical interactions have a short range, which require small amplitudes in the order of 0.1 nm [28]. The tip, which is attached to the free prong of a tuning fork, has a separate tip wire to measure I_t, hence enabling the use in STM mode.

Because short-range forces that are measured, the tip is generally closer to the molecule in nc-AFM than in STM. This increases the influence of the exact atomic geometry of the tip and it increases the probability of displacement or pick-up of an atom or a molecule by the tip. These problems can be minimized by functionalizing the tip apex with different atoms or molecules. The effect of various atomic tips (metal-terminated, chlorine, pentacene etc.) on the nc-AFM contrast has been studied. As of now, the highest lateral resolution was observed with carbon monoxide (CO) functionalized tips [29, 30]. Further investigations have shown that a CO-functionalized

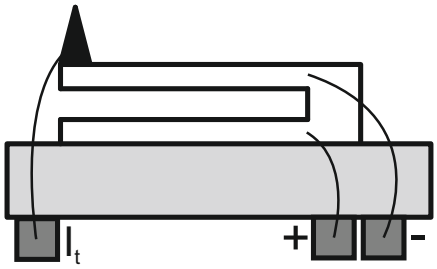

Figure 1.6 Schematic of the nc-AFM tip mount. The tip is connected to the piezoelectric tube via a mechanical resonator. The surrounding is the standard STM setup.

tip shows significant p-wave tip contributions in STM which causes the increased resolution [31].

Three different forces act on the tip: electrostatic forces, van der Waals forces, and Pauli repulsive forces. The first two contributions are attractive and show little lateral corrugation on the atomic scale. However, they give rise to a halo surrounding the molecules in the Δf maps. The atomic resolution is therefore achieved by entering the regime of repulsive forces. The Pauli repulsion forces become substantial when regions of high electron density overlap. This happens at bonds and near atomic positions if tip-sample distances are sufficiently small (~ 0.5 nm) [29]. As a result a nc-AFM image is related to the overall electron density, which is similar in STM in which the electron orbitals near the Fermi energy are probed.

1.5 Bottom-up fabrication

As described in Section 1.1, the feature size of transistors that are commercially available has been reduced to 22 nm. This miniaturization relies on the ability to control materials on very small length scales. So far, this has been accomplished through so-called top-down techniques. This means using a larger raw material and trimming away some of the material to leave the final product. This approach has been used for numerous products like building a table from lumber or fabricating a microchip. Transistors in a computer chip are currently fabricated using photolithography. This technique uses light to make patterns in a photoresist to be used as an etch mask. Corrosive methods are then used to etch the photoresist patterns onto the desired target material (traditionally silicon).

A massive benefit of photolithography is the possibility to produce in parallel. A single light mask can be used to produce millions of microchips with all features on

a single wafer patterned in a single exposure. With the demand for more powerful devices, smaller transistor sizes are required, which is quite a technical challenge. Photolithography is limited by diffraction, the scattering of light when it encounters obstacles comparable in size to its wavelength. So far, the main solution has been to decrease the radiation wavelength, but the demand for smaller transistors makes ever shorter wavelengths necessary. However, there are many issues associated with each step to a shorter wavelengths.

As previously mentioned, future computer chips will have to face and control quantum effects. Due to the sensitive nature of these effects, the transistor will need to have atomic precision. The smallest structure size achieved with lithography is 2 nm [32], in which case, an electron beam exposed the pattern on photoresist. However, it is not even close to the needed atomic precision.

A solution to this problem is the bottom-up technique, which constructs the desired structures from fundamental building blocks, in contrast to removing material in the top-down approach. A common example of this technique is building a house out of bricks. At the nanoscale, the building blocks are molecules and atoms and the construction usually happens spontaneously through self-assembly, without the need for patterning. This means the final atomically precise structures are fully dictated by the properties of the building blocks and their interaction with the surface or solution. An additional benefit is the possibility that structures can be fabricated in parallel (similar to photolithography). The ability to design and apply self-assembly into nanofabrication requires full understanding of the mechanisms of how self-assembly works in a system. Today, the predesigned growth of complex structures is sill in the fledgling stages, but the potential is enormous: the human body is build this way.

1.5.1 Self-assembly on solid surfaces

Self-assembly is a spontaneous physical or chemical process by which objects, initially distributed at random, arrange into well-defined patterns exclusively via local interactions and without external intervention (Fig. 1.7. Usually this happens in a liquid phase or on a solid substrate due to the mobility requirement on the building blocks. The physics underlying the self-assembly processes have been studied for decades and have attracted increasing attention, especially in the recent decade with the emergence of nanoscience [33]. Until now, many self-assembly processes are suffering from defects and inadequate control of repeatability. At the nanoscale, the properties of the self-assembled structures highly depend on the composition of building blocks and the surface or liquid at or in which the process occurs. Developing efficient and robust

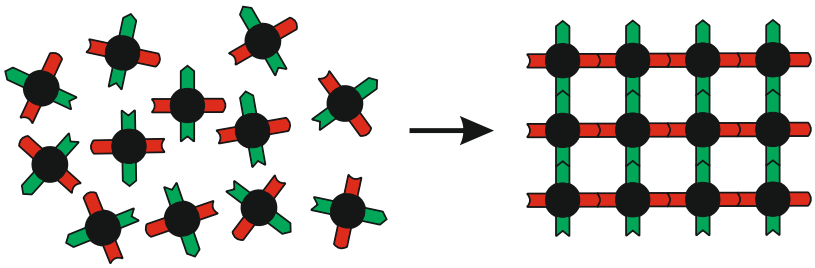

Figure 1.7 Schematic representation of molecular self-assembly. Organic molecules equipped with particular functional groups (red and green areas) at the peripheral positions of the molecule can interact in specific ways to control the ordering of the molecular building blocks.

ways of assembling the building blocks into well-defined nanostructures is therefore crucial.

Because self-assembly is a spontaneous process, the associated free Gibbs energy change during the process must be negative according to thermodynamics. However, external energy from radiation or thermal energy can cause the final structure to not be in its energetically most favorable state [34]. A change in the Gibbs free energy ΔG can be broken down into a change in enthalpy ΔH and a change in enthropy ΔS:

$$\Delta G = \Delta H - T\Delta S, \tag{1.5}$$

with T the temperature of the system. Equation 1.5 provides a reasonable description of self-assembling systems, where a (local) minimum in Gibbs free energy corresponds to a meta-stable state of the overall system.

The self-assembly of building blocks is driven by interactions such as van der Waals forces, electrostatic forces [35] and magnetic forces [36], being either attractive or repulsive. In addition, the building blocks are governed by Brownian motion in a liquid. This thesis will focus on self-assemblies which occur on solid surfaces. In this case the interaction of the building blocks with the surface plays a major role as the alignment along certain surface reconstructions may be preferred and influences the out-coming network [37]

1.5.2 On-surface polymerization

After self-assembling, the molecules are usually fixed by relatively weak interactions between each other. For the fabrication of stable nanostructures it is necessary to form covalent bonds between them. One very reliable approach is on-surface polymerization. The building blocks of the final nanostructures have predefined bonds, which

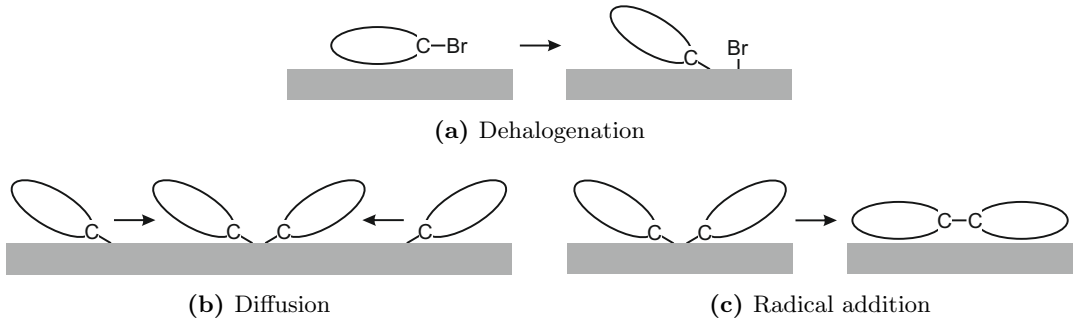

(a) Dehalogenation

(b) Diffusion **(c)** Radical addition

Figure 1.8 Reaction schematic of the on-surface polymerization steps. (a) Dehalogenation of a precursor monomer, initiating the polymerization. Organometalic and halogenmetalic complexes are formed. (b) diffusion of the radical monomer units on the surface. (c) Radical addition of two radiacal monomer units.

are designed to be activated at elevated temperatures [38,39] or voltage pulses with an STM tip [40] while the remaining molecule stays intact. The predetermined bond position is realized through halogen atoms whose binding energies are lower than all other binding energies of the molecule. Average carbon-carbon single and double bonds have binding energies of 3.61 eV and 6.33 eV, respectively, and a carbon-hydrogen bond has a binding energy of 4.29 eV, whereas carbon-bromine and carbon-iodine bonds have energies of only 2.94 eV and 2.22 eV, respectively [41]. In highly delocalized electron systems, these values for single bonds can be higher by a factor of 1.5 [42]. After dehalogenation, a free dangling bond is left at each of the former positions of the halogen atoms and surface-stabilized radicals are created. Through radical addition, covalent bonds can be formed.

The basic idea of on-surface polymerization is to combine self-assembly with the radical addition reaction on a surface. Depending on the design of the molecular building blocks, in particular concerning the position of the halogens, the resulting structure can be defined. Precursor molecules with two halogens can form polymer chains [12,43], on the other hand, precursor molecules with three or four halogens can form two-dimensional networks [12,44]. Using different halogens in the same molecule enables a stepwise growth due to the different dissociation energies.

The surface plays an important role in the dehalogenation process and the subsequent diffusion of the radical monomer und until the coupling of two of them by radical addition. In Fig. 1.8, these three reaction steps are illustrated. The biphenyl synthesis from bromobenzene and iodobenzene has been studied computationally as a model system to describe dehalogenation, diffusion and radical addition on closely

packed (111) surfaces of gold (Au), silver (Ag) and copper (Cu) [42].

In vacuum, dehalogenation of bromobenzene into phenyl and atomic halogen is strongly suppressed, because the resulting radicals have a 3.85 eV higher energy than the starting molecule. On a metal surface, the radical products are stabilized by the creation of organometallic and halogenmetallic complexes, respectively [45, 46]. These complex compounds result in a reduction of the total energy by 0.16 eV (Au), 0.50 eV (Ag) and 0.68 eV (Cu) compared to the initial bromobenzene and with a energy barrier for dehalogenation of 1.02 eV (Au), 0.81 eV (Ag) and 0.66 eV (Cu) [42]. In the case of iodobenzene, all these values are about shifted by about -0.3 eV.

The dehalogenation has shown the highest reactivity for the Cu(111) surface and the lowest reactivity for the Au(111) surface, which also influences the diffusion of the radical monomers on the respective surfaces. Phenyls havs a diffusion barrier of 0.22 eV (Au), 0.29 eV (Ag) and 0.44 eV (Cu) and it can be expected that other radical monomers have the lowest diffusion barrier on Au(111) and the highest on Cu(111).

In order for the polymerization to proceed, the radical addition of two radical sites needs to lower the energy of the starting organometallic complexes and the energy barrier for the reaction needs to be sufficiently low. In the case of radical addition of two phenyls, the energy of the resulting biphenyl is 2.41 eV (Au), 2.56 eV (Ag) and 2.01 eV (Cu) lower and the energy barrier is 0.25 eV (Au), 0.46 eV (Ag) and 0.19 eV (Cu).

The examples of bromobenzene and iodobenzene illustrates the significance of the metal surface during polymerization. In fact, most on-surface polymerizations require the stabilization of radical intermediates by a metal substrate, but it has been shown, that this surface stabilization is not required for at least some halide-substituted monomers [47].

1.6 Graphene and graphene-based structures

Graphene is a single layer of carbon atoms arranged in a hexagonal honeycomb lattice as displayed in Fig. 1.9(a). It can be understood as a two-dimensional crystal with a two-atomic basis of a periodic lattice. The distance between neighboring carbon atoms is $d_{CC} = 0.146$ nm [48]. Figure 1.9(b) shows the reciprocal lattice which has again a honeycomb lattice, however rotated by 90°. This results in a hexagon shaped first Brillouin zone. The six corners are referred to as K-points with two nonequivalent species K and K'.

The huge interest in graphene results from the many superlatives to its name [49]. Of all ever measured materials it is the thinnest and the strongest, has the highest

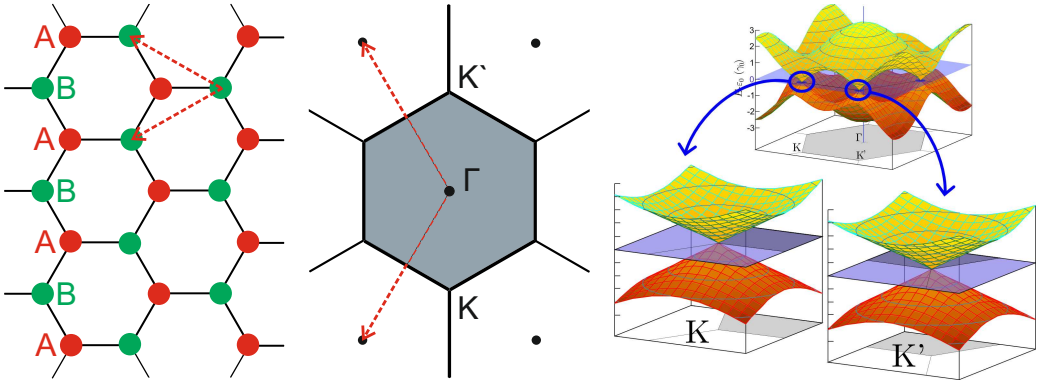

(a) Real space **(b)** Reciprocal space **(c)** Band structure

Figure 1.9 The honeycomb structure of graphene (a) along with its first Brillouin zone (blue) in reciprocal space (b). With the real space lattice vectors at 60° against each other and each of length $\alpha = \sqrt{3}d_{CC} = 0.246$ nm, the reciprocal lattice vectors are at an angle of 120° and of length $\frac{4\pi}{\sqrt{3}d_{CC}} = 0.511\ \frac{1}{\text{nm}}$, with d_{CC} being the carbon-carbon bond length. (c) Band structure of graphene and zoom into the band structure around each of the two non-equivalent K-points. The E_F-surface is diminish to E_F-points at the K-points. The bands can be approximated by axially symmetric cones with slope v_F.

electron mobility, thermal conductivity and second largest stiffness only excelled by diamond, another allotrope of carbon. Additionally it can sustain current densities six orders of magnitude higher than copper and is impermeable to gases.

Today there are two basic approaches to producing graphene. The first is the isolation by exfoliation of a single layer from graphite, a stack of multiple graphene layers [50]. The second is to grow it epitaxially by depositing one layer of carbon onto another material [51]. Today several versions of these two approaches exist. Single layer graphene used to be considered thermodynamically unstable [52] which is why there were hardly any attempts to fabricate it until its discovery in 2004 [53]. There the exfoliation approach was taken by using adhesive tape to peel monolayers off graphite.

The unique electronic structure of graphene is the basis in understanding the electronic properties of graphene nanostructures. As it will be shown in the last part of this section, the electronic band structure of one-dimensional graphene nanoribbons are simply one-dimensional cuts in graphene's two-dimensional band structure.

Each one of the carbon atoms is sp^2-hybridized and links with its three neighbors

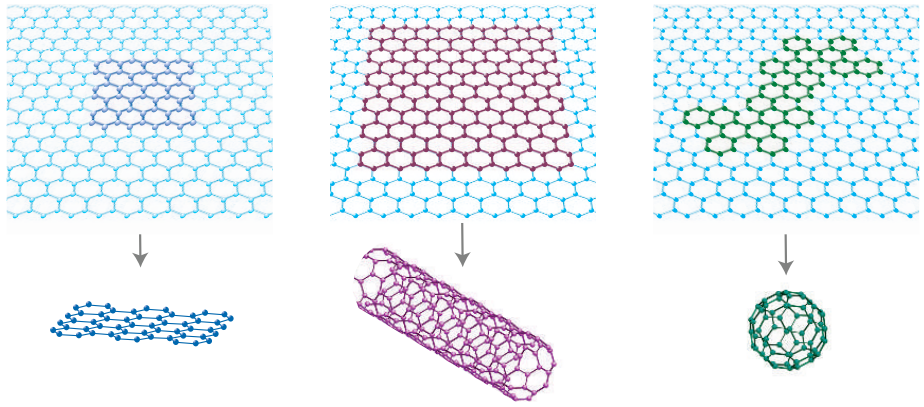

(a) Flake **(b)** Nanotube **(c)** Buckyball

Figure 1.10 Theoretical construction of graphene-based nanostructures. It can be cut into flat two-dimensional structures, rolled into one-dimensional nanotubes or wrapped up into zero-dimensional buckyballs. (Images adapted from [50])

via strong covalent bonds. The corresponding σ-bands (bonding and anti-bonding) are split to high absolute energy values and can therefore be neglected, when investigating the low energy band structure. The remaining valence electron in the p_z orbital leads to the formation of another pair of bands, the so-called π-bands. Within the tight-binding approximation it is possible to derive the band structure of graphene [54]:

$$E(\mathbf{k}) = \pm\gamma_0 \sqrt{1 + 4\cos\left(\frac{k_y\alpha}{2}\right)\cos\left(\frac{\sqrt{3}k_x\alpha}{2}\right) + 4\cos^2\left(\frac{k_y\alpha}{2}\right)}, \tag{1.6}$$

with hopping parameter γ_0 and the lattice constant $\alpha = \sqrt{3}d_{CC} = 0.246$ nm. The characteristic shape of the resulting band structure with its constant energy mirror symmetry plane is displayed in Fig. 1.9(c). The π-bands of (undoped) graphene are half-filled, so E_F is exactly at the energy of the symmetry plane, resulting in an exact electron-hole symmetry within the π-bands. This is also the region of most physical relevance. Here, VB and CB touch at the K-points, forming axially symmetric double-cone structures, which can be approximated by a linear dispersion relation:

$$E(K^{(\prime)} + \mathbf{k}) = v_F\hbar\mathbf{k}, \tag{1.7}$$

with the Fermi velocity v_F (see Fig. 1.9(c)). In this special situation, where $E_F = E_{VB} = E_{CB}$, a material is called semimetallic. The energy where the graphene bands touch is referred to as charge neutrality point.

Graphene has a high suitability for possible applications in electronic devices [50]. Electrons can travel for micrometers without scattering at room temperature, together with low contact resistances without a Schottky barrier should allow fast switching times. However, the on-off ratios are limited by the absence of a band gap. For high-frequency application, this does not present a fundamental problem, as IBM presented a 100 GHz transistor made from graphene on a silicon carbide wafer which showed a higher cut-off frequency than the best silicon MOSFET at the same gate length [55]. For logic applications, however, the absence of a band gap is a problem, and needs to be overcome. A band gap can be induced by spatial confinement seen in nanostructures.

Nanostructures based on graphene can come in very different ways. Figure 1.10 shows three very different structures, a flat flake, a nanotube and a buckminsterfullerene which is often just called buckyball. When breaking graphene into small flat pieces, two kinds of edges border the structures. Zigzag edges, which carry an electronic edge-state [56,57] and armchair edges which carry edge phonons [58]. These edges become especially relevant for finite width ribbons.

1.6.1 Graphene nanoribbons

Graphene nanoribbons (GNRs) are narrow stripes of graphene. The armchair and zigzag edges and the definition of the width of both forms are illustrated in Fig. 1.11. In the case of ideal GNRs, with no disorder and perfect edges, the band structure is very sensitive to its edge type and to its exact width [59]. Nanoribbons with zigzag edges have flat energy bands near E_F, corresponding to extended edge states. Depending on the precise width of the ribbon, armchair GNRs can be either metallic or semiconducting with an electronic band gap inversely proportional to the ribbon width.

The band structures of both GNR types are closely related to the band structure of two-dimensional graphene. The boundary conditions at the armchair edge are compatible with the unperturbed electronic structure of graphene. The wave function obtained from placing armchair GNRs side by side also exists in graphene. The band structure of N-AGNRs can thus be obtained from slicing the band structure of graphene at N equidistant wave numbers. The highest occupied band is always given by the cut that comes closest to the Dirac point of the graphene Brillouin zone. The whole derivation of this can be found in reference [59]. In the armchair case, equation

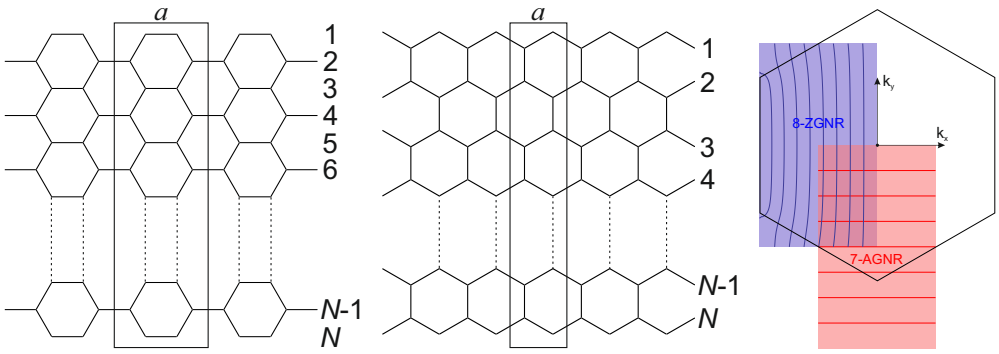

(a) Armchair GNR **(b)** Zigzag GNR **(c)** Brillouin zones

Figure 1.11 Armchair and zigzag GNRs. (a) and (b) The unit cell a and the definition of the GNR width N is shown for both cases. (c) The Brillouin zones of a 7-AGNR and an 8-ZGNR as slices of the graphene band structure and its Brillouin zone.

1.6 reduces to a one-dimensional structure with discrete k_y:

$$E(k_x) = \pm\gamma_0\sqrt{1 + 4\cos(p)\cos\left(\frac{k_x}{2}\right) + 4\cos^2(p)}, \tag{1.8}$$

with $p = \frac{r}{N+1}\pi$, $r \in \{1 \dots N\}$.

Contrary to the case of the armchair GNRs, the boundary condition for the zigzag edge is incompatible with the graphene lattice. However, it was shown that the spectrum of all bands but one of the zigzag GNRs can still be obtained by slicing the band structure of graphene, however, these N slices do not follow straight lines. The one band which cannot be sliced completely has an imaginary component in the cutting line that corresponds to the partial flat bands of the edge states [59]. In the zigzag case, the π-bands of the extended states are given by:

$$E(k_y) = \pm\gamma_0\sqrt{1 + 4\cos\left(\frac{k_y}{2}\right)\cos(p) + 4\cos^2\left(\frac{k_y}{2}\right)}, \tag{1.9}$$

where p are the N solutions of the equation

$$\sin(pN) + 2\cos\left(\frac{k_y}{2}\right)\sin(p(N+1)) = 0. \tag{1.10}$$

The cutting lines in the band structure of graphene for an $N = 7$ armchair GNR and an $N = 8$ zigzag GNR is displayed in Fig 1.11(c). In this figure, the one band which cannot be sliced completely corresponds to the left most cutting line. The parts missing to the k_y-borders of the highlighted Brillouin zone $\left(\pm\frac{\pi}{a}\right)$ is the imaginary

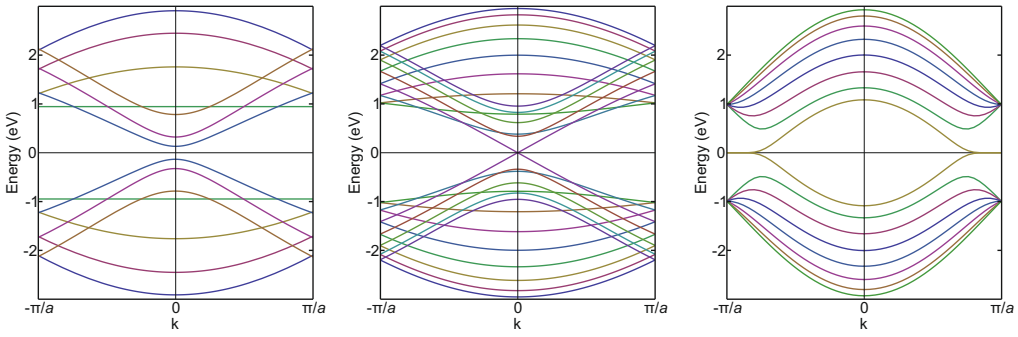

(a) 7-AGNR **(b)** 14-AGNR **(c)** 8-ZGNR

Figure 1.12 Band structure of GNRs calculated from equations 1.8, 1.9 and 1.10 with $\gamma_0 = 1$ eV. (a) Band structure of a semiconducting $N = 7$ armchair GNR within the first Brillouin zone and (b) the same for a semimetallic $N = 14$ armchair GNR. (c) Band structure of an $N = 8$ zigzag GNR within the first Brillouin zone. Note the different definitions of a in armchair and zigzag GNRs (see Fig. 1.11).

component which exhibits a flat band structure. The number of cuts is determined by N and the spacing between them will be $k_y = \frac{4\pi}{3d_{CC}(N+1)} = \frac{28.69}{N+1}\ \frac{1}{\text{nm}}$ for armchair GNRs and $k_x = \frac{2\pi}{\sqrt{3}d_{CC}(N+1)} = \frac{24.84}{N+1}\ \frac{1}{\text{nm}}$ at $k_y = 0$ for zigzag GNRs. Three examples of the band structure of GNRs, including the ones of an $N = 7$ armchair GNR and an $N = 8$ zigzag GNR, are depicted in Fig 1.12. The band structure of the $N = 8$ zigzag GNR (c) clearly exhibits the described flat band near the Brillouin zone border at $E = E_F$. The hopping parameter γ_0, which linearly scales the energy axis and the band gap, was chosen as unity for convenience. For a correct value, γ_0 needs to be fitted to experimental data.

Just like in graphene, the π-bands of GNRs are half filled and E_F is exactly at the energy of the symmetry plane. The VB and CB arise from the cut closest to the K-points. Due to the π-band symmetry, all armchair GNRs have a direct band gap. The band gap is inversely proportional to the ribbon width, however, as shown in Fig 1.13(a) it is split into three families, which are classified according to whether $N = 3p$, $3p + 1$, or $3p + 2$. The $3p$ and $3p$+1 families are semiconducting, while the $3p$+2 family is semimetallic because the cut in the graphene band structure which corresponds to the VB and CB goes through the K-point. In Fig. 1.12(a) and (b) examples of a semiconducting and a semimetallic armchair GNR's band structure are shown. The semimetallic 14-AGNR clearly shows the same linear dispersion near $k_y = 0$ as graphene. The presented tight binding model is based on equivalent carbon-carbon bonds throughout the graphene and GNRs. However, the hydrogen passivation

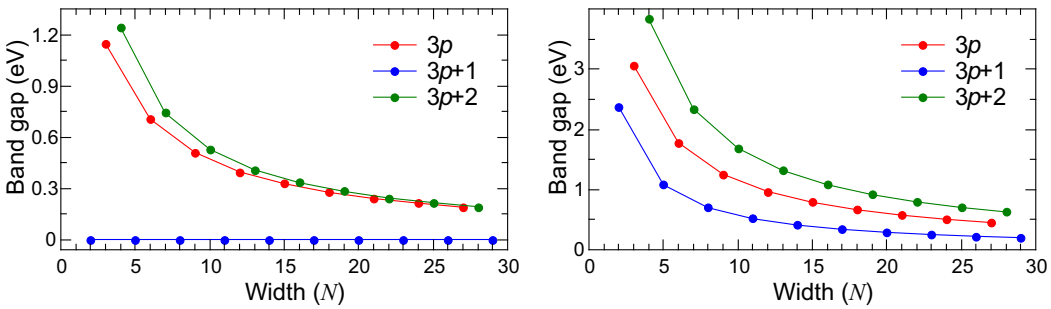

(a) Band gap tight binding

(b) Band gap DFT

Figure 1.13 Variation of band gaps with the width of N-AGNRs obtained (a) from the tight binding equation 1.8 with $\gamma_0 = 3$ eV (a good approximation for graphene structures) and (b) from the LDA formula given in [65]. The three families of AGNRs are represented by different colors.

at the GNR edges alters the bonds of the passivated carbon atoms. When these non-equivalent carbon-carbon bonds are included into the tight binding calculation a band gap opens in the semimetallic $3p$+2 armchair GNR family [60, 61]. This band gap is inversely proportional to the ribbon width too, but smaller than the band gap of the other two families.

Narrow GNRs of few nanometer widths have been fabricated by lithography [62], sonochemical cutting from large graphene sheets [63] and unzipping carbon nanotubes [64] amongst others. However, atomic precision is needed for reproducible electronic properties, but non of the above techniques has been able to fully control the edges. In 2010 atomically precise straight 7-AGNRs were first reported which had been synthesized via the bottom-up approach [43]. The growth will be analyzed in detail in Chapter 3.

1.7 Density functional theory

Since part of the experimental data is supported by theory, a small introduction to the used methods will be given here.

The calculation of quantum mechanical properties of matter is a solution to the Schrödinger equation. Only for hydrogen-like atoms this is strictly possible, in many-electron systems approximations must be introduced. The first important one is the Born-Oppenheimer approximation [66], which allows the separation of the Hamiltonian into nuclear and electronic terms. However, this simplification is not suitable to treat large scale systems due to the complexity of the integrals describing the electron-

electron interaction. A way to circumvent this problem was proposed by Thomas [67], Fermi [68] and Dirac. The accuracy of their approaches was however too low. In 1965 Kohn and Sham [69] developed a method using functionals of the electron density (hence the name density functional theory (DFT)), which has since then been widely applied and refined in its details. The DFT approach to describe the ground state properties of an N-atom system is to replace the wavefunction (depending on $3N$ variables) with the electron density, which only depends on 3 variables. In fact, the Hohenberg-Kohn theorems [70] state that the energy and all observables of the ground state of a multi-electron system are functionals of the electron density, and the minimization of the energy with respect to the electron density yields the actual ground state energy of the system. Furthermore, Kohn and Sham proposed a method to minimize the energy functional by treating the electrons in the system as if they were non-interacting. This leads to the Kohn-Sham equation

$$\left(-\frac{1}{2}\nabla^2 + \Phi_{eff}(\mathbf{r})\right)\phi_j(\mathbf{r}) = \epsilon_j\phi_j(\mathbf{r}) \tag{1.11}$$

where the Schrödinger equation is reduced to a system of single-particle equations. Here, ϵ_j is the orbital energy of the corresponding Kohn-Sham orbital, ϕ_j. The electron density n_s is obtained by the sum over all electron densities in the N-particle system:

$$n_s(\mathbf{r}) = \sum_{j=1}^{N} |\phi_j(\mathbf{r})|^2 \tag{1.12}$$

The effective potential Φ_{eff} depends on the density:

$$\Phi_{eff}(\mathbf{r}) = \Phi_{ext}(\mathbf{r}) + \int \frac{n_s(\mathbf{r})}{|\mathbf{r}-\mathbf{r}'|} d^3r' + \Phi_{xc}(n_s(\mathbf{r})) \tag{1.13}$$

Φ_{ext} denotes the external potential given by the nuclei, the second term describes the electrostatic interaction between the electrons and the last term Φ_{xc} is the so called exchange-correlation potential. As Φ_{eff} depends via n_s (1.13) on ϕ_j (1.12), which in turn depends on Φ_{eff} (1.11), the solving of the Kohn-Sham equation has to be done in an iterative way. The standard procedure is to start with a guess for $n_s(\mathbf{r})$, calculate $\Phi_{eff}(\mathbf{r})$ and then solves the Kohn-Sham equations for $\phi_j(\mathbf{r})$. The resulting $\phi_j(\mathbf{r})$ is then used to calculate a new n_s. This procedure is then repeated until convergence is reached.

A major challenge in using DFT are adequate approximations of the unknown exchange-correlation potential $\Phi_{xc}(\mathbf{r})$. It depends not only on n_s at point $\mathbf{r}$, but in fact on n_s at all points. For computational reasons, the local density approximation (LDA) $\Phi_{xc}(\mathbf{r}) = \Phi_{xc}(n_s(\mathbf{r}))$ is still widely used and leads satisfactory results in many

applications. In LDA the functional depends only on n_s at the coordinate where the functional is evaluated.

Band gaps of armchair GNR

An application example of DFT with LDA is shown in Fig. 1.13(b). The armchair GNR band gaps for varying width were calculated using the formula given in [65]. Just like with the tight binding approach (Fig. 1.13(b)), the three width dependent band gap families can be identified and even the semimetallic $3p+2$ family exhibits band gaps. The used formula is based on a hard-wall boundary condition, which leads to an inverse relation, $E_g \propto \frac{1}{N+N_0}$ with N_0 being a small constant, which characterizes the width dependence of the band gap. The hard-wall boundary condition is ,however, not accurate. In fact, the electron density will leak out of the GNR boundaries making the effective width of GNRs larger than the physical width N. Interestingly, the effective widening is of a different magnitude depending the three families [65].

Chapter 2

Experimental Details

2.1 Experimental setup

All sample preparation and all the experiments were performed in two ultra high vacuum (UHV) setups which have a base pressure of 2×10^{-11} mbar. Both setups consist of two main chambers and a small fast entry lock through which samples can be transferred into and out of the systems. In the analysis chambers the low temperature STM and the non-contact AFM measurements are performed. The preparation chambers have several instruments attached to it, which allow various sample preparations. The ones used for this work are:

- Argon sputter gun: Used for cleaning the samples and leaking argon into the system.
- Manipulator: Used for degassing and annealing the samples and for transfer between the preparation and analysis chambers.
- UHV evaporator: Used for thermal evaporation of molecules and salts.
- Quartz crystal microbalance: Used to measure deposition rates.
- Pressure gauges: Used to monitor the pressure.
- External pyrometer: Used to measure surface temperatures.
- Leak system: Used to introduce specific gases.

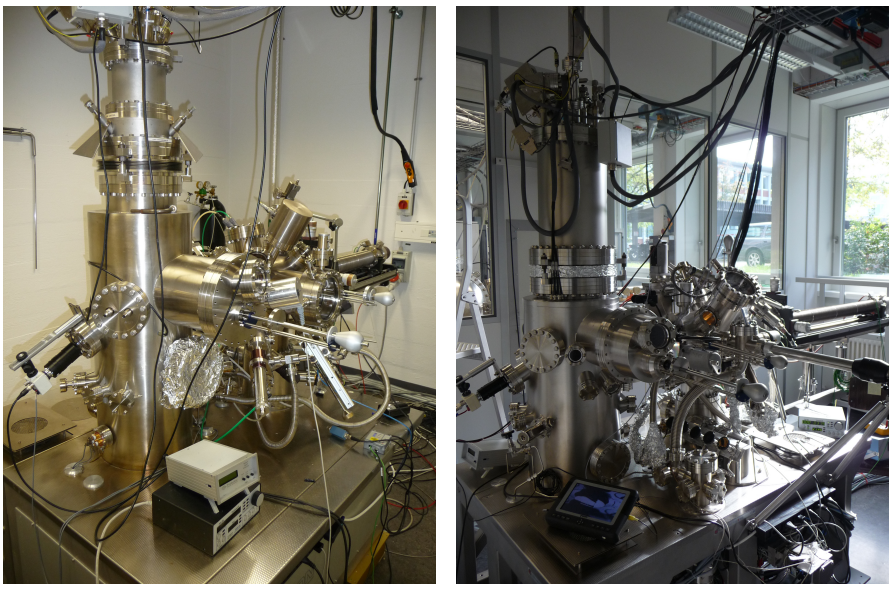

(a) LT-STM system **(b)** Qplus system

Figure 2.1 Pictures of the UHV systems used in the experiments. (a) Low temperature STM system. (b) Qplus system for nc-AFM measurements. Attached to the preparation chambers are ion sputter gun, manipulator, molecule evaporator and the leak system.

2.1.1 Low temperature STM system

The STM which was used for all but the non-contact AFM experiments is a commercially available low temperature STM from Omicron Nanotechnology GmbH. Temperatures as low as 4.2 K can be achieved under ideal conditions. However, other research that is performed on the instrument required, that an infra-red light blocking window had to be replaced by a standard window. As a result the temperature during the experiments was 5 K. The low temperature STM is located fully inside two cryostats, which can be filled with liquid cooling gases. Vibration isolation is achieved by an integrated spring suspension in addition to active damping feet underneath the system bench. A picture of the low temperature STM system is shown in Fig 2.1(a). A MATRIX control system from Omicron Nanotechnology GmbH was used to control the STM measurements. For STS experiments an additional lock-in amplifier from Stanford Research Systems, Inc. was used.

2.1.2 Qplus system

The used AFM is an upgraded version of the above described low temperature STM which allows non-contact AFM. The measurement setup of the system is commercially available from Omicron Nanotechnology GmbH. The system around the AFM stages is in principle the same as on the low temperature STM system including the active damping feet underneath the system bench. A notable difference are the lager cryostats which can maintain stable low temperatures for a longer time and can reach a minimum temperature of 4.2 K. A picture of the Qplus system is shown in Fig 2.1(b). The same MATRIX control system, that was used on the low temperature STM system, was used to control all measurements. For nc-AFM and STS experiments an additional lock-in amplifier with a phase-locked loop from Zurich Instruments AG was used.

2.1.3 Data analysis

The analysis of the raw data and the Fourier transform of STS maps was done with the matrixfilereader plug-in for IgorPro which is freely available on IgorExchange [71]. It was also used for the creation of the STM and nc-AFM images as well as the STS and FT-STS maps. The final graphs were created with the free scientific graphing software QtiPlot.

2.2 Sample preparation

2.2.1 Au(111) surface

The noble metal gold (Au) is rather inert, and thus a low catalytic activity is expected. The crystal structure of Au is face-centered cubic (fcc) with a lattice constant of $a = 0.408$ nm [72]. The Au(111) surface has a hexagonal structure, however, it does not extend over a large range. Instead, the Au(111) surface reconstructs at room temperature into a $(22\times\sqrt{3})$ overlayer structure known as herringbone reconstruction (see Fig. 2.2). Thereby, 23 atoms of the top layer are placed on top of 22 atoms of the second layer which results in a pattern of fcc and hexagonal close-packed (hcp) stacked areas [73]. A clean Au(111) surface exhibits a Shockley-like surface state at -0.52 eV, which is of importance in $\frac{dI_t}{dV_B}$ spectroscopy [74].

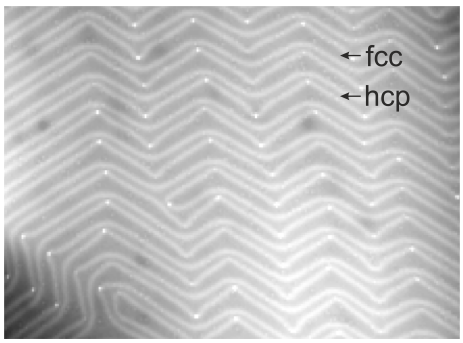

Figure 2.2 Au (111) herringbone reconstruction. Arrows indicate the fcc stacked the narrower hcp stacked areas. {110×80 nm}

2.2.2 Surface preparation

Before the deposition of the molecules, the samples were cleaned in UHV conditions. The cleaning of a Au(111) surface was done in two steps. In a first step, the surface is sputtered for 20 minutes with accelerated, ionized argon atoms at angles of ±40° to the surface normal. This removes the top layers of the surface. During sputtering the partial pressure of argon was 5×10^{-5} mbar and the kinetic energy of the argon atoms was 1.0 keV. After sputtering the samples were annealed for 20 minutes at temperatures around 480°C. After cooling the samples to room temperature the substrates were ready for the molecule evaporation.

2.2.3 Molecules

Three different species of precursor monomers were studied for the fabrication of the armchair GNRs: 10,10'-dibromo-9,9'-bianthryl (DBBA), 3',6'-dibromo-1,1':2',1"-terphenyl (DBTP) and 2',5'-diiodo-1,1':4',1"-terphenyl (DITP). Figure 2.3 shows the three molecules which have all been synthesized in the group of Klaus Müllen (Max Planck Institute for Polymer Research, Department of Synthetic Chemistry). DBBA has become commercially available during the duration of the presented work and have since been supplied by BASF SE.

A three-fold, commercially available Kentax, and a six-fold sublimation evaporator were used, enabling simultaneous and/or subsequent evaporation of different molecules. Before introducing new molecules into a system, their sublimation temperature was tested in a homemade sublimation rate detector, which consists of a single sublimation evaporator and a quartz crystal microbalance. The sublimation temperatures used in the presented work were 150°C (DBBA), 80°C (DBTP) and 120°C (DITP) which corresponds to a deposition rate of about half a monolayer per

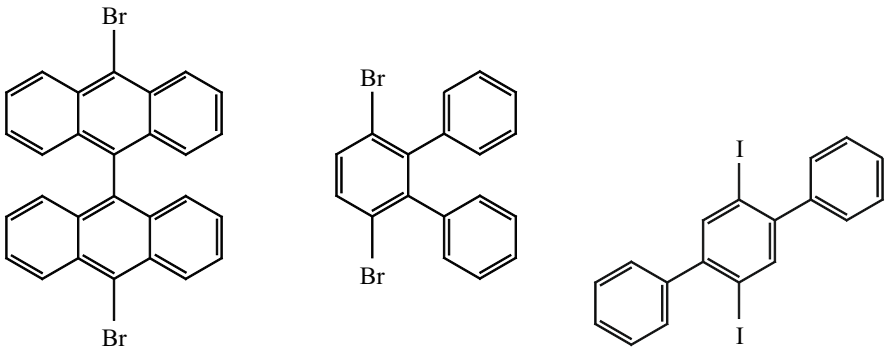

(a) DBBA **(b)** DBTP **(c)** DITP

Figure 2.3 Precursor monomers: (a) 10,10'-dibromo-9,9'-bianthryl, (b) 3',6'-dibromo-1,1':2',1"-terphenyl and (c) 2',5'-diiodo-1,1':4',1"-terphenyl.

minute for the respective molecules. Each crucible in the sublimation evaporators has a separate thermocouple for temperature measurement.

Chapter 3

Bottom-up Synthesis

In Chapter 1 the basic principals of the bottom-up fabrication method have been described. In this chapter the growth processes of graphene nanoribbons using two different precursor monomers are discussed.

All preparations have been done on Au(111) surfaces. Usually a Au single crystal had been used, in cases which the single crystal had not been available, a mica substrate with an epitaxially grown Au thin film was used. No differences have been observed between the two substrates in terms of the growth process, sample quality or the settings needed for the growth.

3.1 $N = 7$ armchair graphene nanoribbons

The growth of $N = 7$ armchair graphene nanoribbons (7-AGNRs) has first been reported in 2010 [43] and theoretically described two years later [75]. Like in this dissertation, in most publications the 7-AGNRs have been grown on a Au(111) surface using 10,10'-dibromo-9,9'-bianthryl (DBBA) as precursor monomer. However, it is also possible to use Ag(111) and Cu(111) substrates. In both cases the temperatures for polymerization and cyclodehydrogenation have to be reduced, which relates to the different surface reactivities discussed in Section 1.5 [76].

The fabrication of 7-AGNRs consists of four steps. In the first step DBBA is thermally sublimated onto the Au(111) surface. There, the bromine substitutes are removed, resulting in activated molecular building blocks, which are stabilized by the Au surface. These radical monomers diffuse across the surface and undergo radical addition forming linear polyanthracene (PA) polymer chains, which self-assemble parallelly into islands. The final step cyclodehydrogenation results in flat graphene nanoribbons.

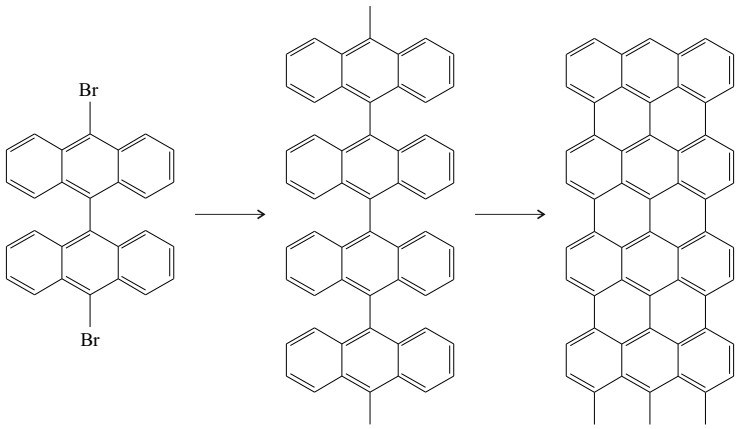

Figure 3.1 Reaction scheme from DBBA via PA polymer to 7-AGNR.

In practice, the first three fabrication steps are done simultaneously as shown in Fig. 3.1. DBBA is evaporated onto an already hot surface for 30 to 120 s depending on the desired coverage. This way, dehalogenation and radical addition start the moment, the precursor molecules arrive at the surface. In this work the sample temperature during the polymerization process was between 140°C and 250°C. The influence of the different temperatures on the 7-AGNR quality will be investigated later on in Section 3.1.2. The annealing was continued at the same temperature for ten minutes after the molecule deposition had been stopped. The following cyclodehydrogenation step is induced by further annealing to 350°C or higher. As a result, isolated 7-AGNRs are spread out over the Au(111) surface as shown in Fig. 3.2.

A very detailed description of the cyclodehydrogenation reaction with support of DFT calculations has been published by Blankenburg et al. [75]. The reaction is driven by the van der Waals attraction between metal and PA polymer, and by covalent interactions with the substrate, which stabilizes the radical positions. This mechanism is shown in Fig. 3.3. In the first step (a), the PA polymer flattens with respect to its ideal geometry, due to van der Waals interactions with the substrate. As a result, the hydrogen atom of the upwards pointing anthryl end is pushed away from the substrate, while the hydrogen atom of the downwards pointing anthryl end is pushed towards the substrate. In the second step (b), the now downwards pointing hydrogen atom is catalytically detached and diffuses across the surface away from the polymer. The metal surface then stabilizes the resultant radical carbon atom. In the third step (c), the hydrogen atom that is pointing upward relocates to a neighboring carbon atom, creating a local sp^3-hybridization. This further increases planeness of the PA polymer and enables the formation of a bond between the two radical carbon atoms. The following steps (d) and (e) are repetitions of the previous two although

Figure 3.2 Overview of 7-AGNR on Au(111). {700×700 nm}

the new geometry alters the energies involved. In the final step (f), one hydrogen atom from each sp^3-hybridized carbon atom is detached and diffuses across the surface. Due to the established flattening and the resulting reduction of the activation energy at neighboring anthryl ends, a chain reaction is started, with the result, that one side of the PA polymer has fully cyclodehydrogenated while the other side is still in its polymer form. This structure, depicted in Fig. 3.3(g), can be seen as a 5-AGNR with benzene rings attached to one side, which is why it has been given the name 5+-AGNR. A subsequent chain reaction on the other side yields the fully flat 7-AGNRs (Fig. 3.3(h)).

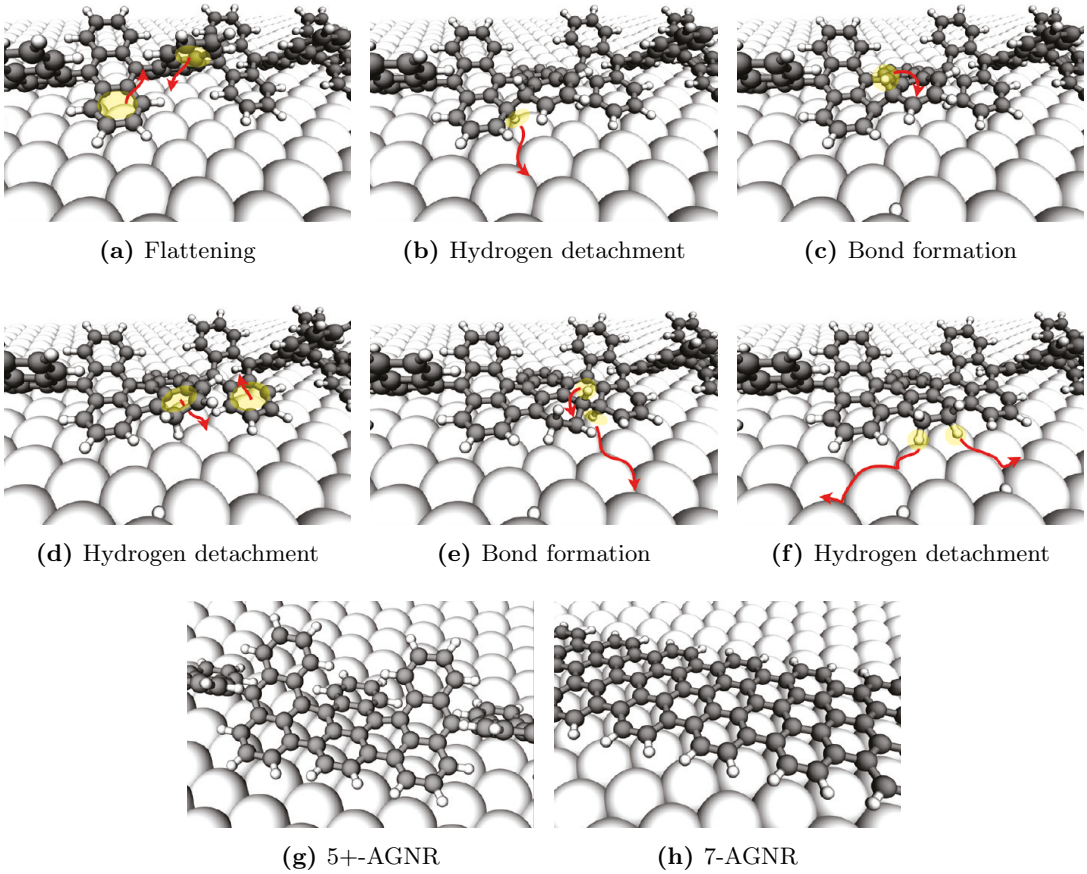

(a) Flattening **(b)** Hydrogen detachment **(c)** Bond formation

(d) Hydrogen detachment **(e)** Bond formation **(f)** Hydrogen detachment

(g) 5+-AGNR **(h)** 7-AGNR

Figure 3.3 Mechanism of the PA polymer cyclodehydrogenation as revealed by DFT calculations. Atomic models representing the geometries of the intermediate states along the reaction path. Large white spheres represent Ag atoms of a Ag(111) substrate. The three up-down repetition units of the polymer included in the simulation cell are visible. Arrows indicate atomic rearrangements that will occur in the highlighted regions upon the transition from one geometry to the next. (Images adapted from [75])

3.1.1 Termini

As a result of the structure of the DBBA, the two termini of a 7-AGNR are composed of short zigzag edges. Nevertheless, the chemical structure of a terminus at the central carbon atom, where the bromine atom of the DBBA used to be bonded, is not trivial. No specific termination monomers were used, which leaves the termination to the an uncontrolled effect which is energetically most favorable. The understanding of the chemical structure of the termini is important, as a change in a single atom can change the electronic properties of the structure and it gives information on process

(a) STM: characteristically shaped terminus

(b) STM: featureless terminus

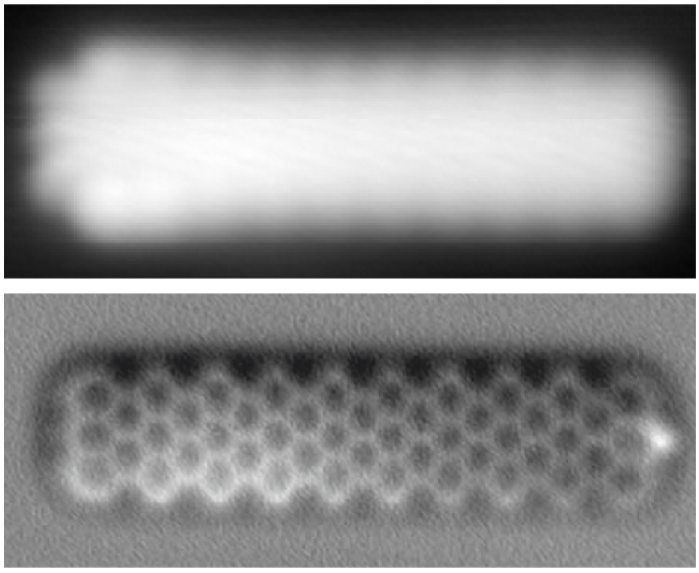

(c) nc-AFM: featureless zigzag edge terminus

(d) nc-AFM: bright spot terminus

Figure 3.4 STM and nc-AFM images of different termini. (a) and (b) STM image of a $10a$ long 7-AGNR with different termini. (c) and (d) nc-AFM image of the same 7-AGNR. {5.0×2.0 nm}

that terminates the polymerization and ultimately the GNRs.

Using high-resolution STM and nc-AFM images, two different termini can be identified. One terminus has a detailed characteristic shape and an enlarged apparent width compared to the bulk in STM experiments at low V_B on Au(111) (Fig. 3.4(a)) which has been observed by several groups [43, 77, 78]. Imaging the same terminus with nc-AFM a featureless zigzag edge is seen (Fig. 3.4(c)). This strongly suggests, that the central carbon atom has a single hydrogen atom attached to itself, just like the other two outside end carbon atoms.

The second terminus appears featureless within the high-resolution limit which could be achieved by STM (Fig. 3.4(b)). This terminus, however, shows a bright spot next to the central carbon end atom in the nc-AFM image (Fig. 3.4(d)). This can only explained by either a bromine atom or two hydrogen atoms. Since the samples have been prepared in UHV conditions, bromine and hydrogen are the only plausible candidates for passivating the radical. Bromine has either failed to detach from the initial precursor monomer or has reattached after dissociation. Atomic hydrogen is generated on the surface during the cyclodehydrogenation step, in which eight

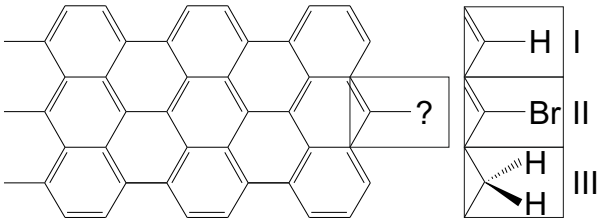

(O) Three terminations at the implied position

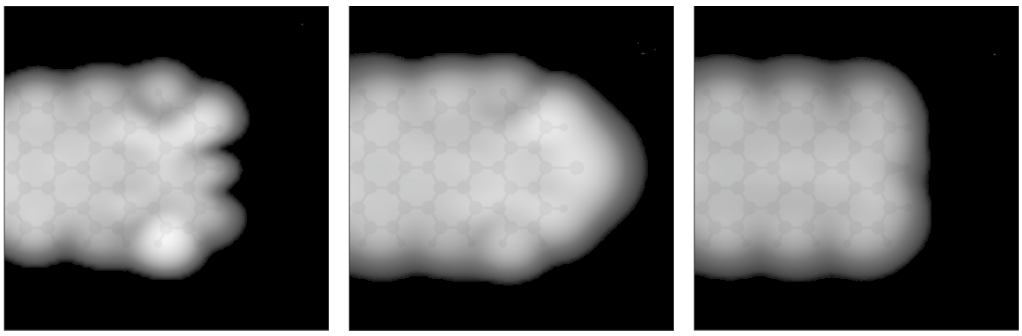

(I) Single hydrogen **(II)** Single bromine **(III)** Two hydrogen

Figure 3.5 Plausible candidates for 7-AGNR termini. (O) Model of the three plausible terminations and (I)-(III) their respective DFT-based STM simulations at an energy -0.3 eV. {2.0×2.0 nm}

hydrogen atoms are released per precursor monomer.

In order to conclusively determine the chemical structure of the terminus, the STM images are compared to STM simulations of finite 7-AGNRs absorbed on a metal substrate which were calculated by DFT. Figure 3.5 depicts the three different chemical terminations of the 7-AGNR, which are plausible candidates according to the analysis of the STM and nc-AFM images. In case I, a single hydrogen passivates the central carbon end atom, which is expected to be the case for the first observed terminus (Fig. 3.4(a) and (c)). Cases II and III consider a single bromine atom and two hydrogen atoms, respectively, which are the candidates for the second observed terminus (Fig. 3.4(b) and (d)).

In the H_1 case where a single hydrogen atom passivats the central carbon atom (I), the result is a monohydrogenated zigzag edge. This kind of edge has been studied intensively as it is a common edge in nanographene structures. A single-orbital nearest-neighbor tight-binding model predicts the presence of electronic midgap states that are localized near the edge [79]. In a zigzag edge as short as in the terminus of the 7-AGNR, the model predicts the existence of exactly one localized Tamm state [77]. This Tamm state shows up in the STM simulation shown in Fig. 3.5(I) and it agrees

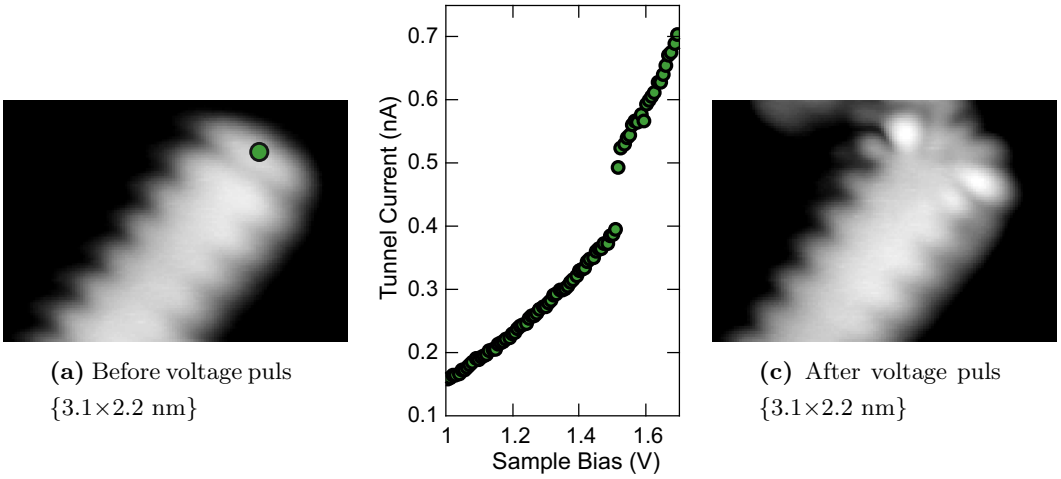

(a) Before voltage puls {3.1×2.2 nm}

(b) Voltage puls

(c) After voltage puls {3.1×2.2 nm}

Figure 3.6 Electron-induced dehydrogenation. (a) STM image of featureless a 7-AGNR H_2 terminus. (b) $I_t(V_B)$ curve of voltage ramp driven at the terminus marked in (a). (c) STM image of the same terminus after the voltage ramp.

with the experiment (Fig. 3.4(a)) very well, reproducing the detailed characteristic shape as well as the enlargement of the apparent width.

The STM simulation with a bromine termination shows a large electron density around the bromine atom (Fig. 3.5(II)). This has no similarity with the experimental STM images shown in Fig. 3.4, ruling out this case as the observed terminus.

Finally, the H_2 case considers the bonding of two hydrogen atoms at the central carbon atom (Fig. 3.5(III)). The STM simulation shows the same featureless termini that has been imaged with STM (Fig. 3.4(b)). This and the agreement in for the H_1 case strongly suggests, that the 7-AGNRs fabricated from DBBA are either terminated with on or two hydrogen atoms at the central carbon atom.

If the two observed termini indeed correspond to the H_1 and H_2 cases, it should be possible to transform a H_2 terminus into a H_1 terminus. This induced dehydrogenation can be done by positioning the STM tip above a featureless ribbon termini, as indicated in Fig. 3.6(a) and increasing V_B while keeping the height constant (Fig. 3.6(b)). A jump in the recorded $\frac{I_t}{V_B}$ at 1.5 eV indicates an incidence. After this procedure, one consistently finds the termini to display the characteristic features of the Tamm state (Fig.3.5(c)).

DFT calculations have shown that a H_2 terminus has a 0.8 eV lower energy than a H_1 terminus [80]. Yet, the H_1 termini usually outnumber the energetically more

favorable H_2 termini. The reason lies in the growth conditions, which will be discussed in the following.

3.1.2 Growth conditions

In Section 1.5, the influence of the metal surface during the three steps of the polymerization was discussed. Additionally, the influence of the substrate on the cyclodehydrogenation of the PA polymer was explained in Section 3.1. The Au(111) surface reduces the energy barriers for the 7-AGNR fabrication to values that allow the synthesis. Still, certain other conditions need to be fulfilled in order to grow 7-AGNRs. As the growth is a temperature induced, two-step chemical reaction, the temperatures in each step need to be sufficiently high in order to overcome the energy barriers. However, the thermal energy in the system may also assist or hinder the 7-AGNR growth in other ways than the sole reactions. An reduction in temperature reduces the mobility of molecules on a surface on the other hand, an increase in temperature may sublimate molecules from the surface or induce other chemical reaction than the intended ones.

Pressure is another factor in on-surface reactions. A pressure of 10^{-6} mbar will form 1 monolayer on the surface in 3 seconds if every atom that hits the surface sticks to it [81]. If an atom or molecule in the ambient gas can react with one or more of the reactants on the surface, the actual product will be dissimilar from the projected one.

Temperature dependence

As the fabrication of 7-AGNRs is experimentally a two-step process, the temperature dependence on the length and structural quality can depend on both temperatures used in the two steps. The temperature has various effects on the kinetics of polymerization reactions and this problem has been addressed in several publications [82–86].

In order to observe the influence of the polymerization temperature (T_p), a series of samples were prepared with the same parameters except T_p which ranged from 140°C to 250°C in steps of about 7°C in the center half of the range. The two annealing steps lasted 10 minutes each and the cyclodehydrogenation was done at 370°C. Figures 3.7(a) and (b) show images of samples prepared at 155°C and 196°C, respectively. The quality and the length distributions of the two samples are strikingly different.

As a first analysis, the average lengths of the 7-AGNR of all the prepared samples was determined. Figure 3.7(c) exemplary shows the sample prepared at 155°C with

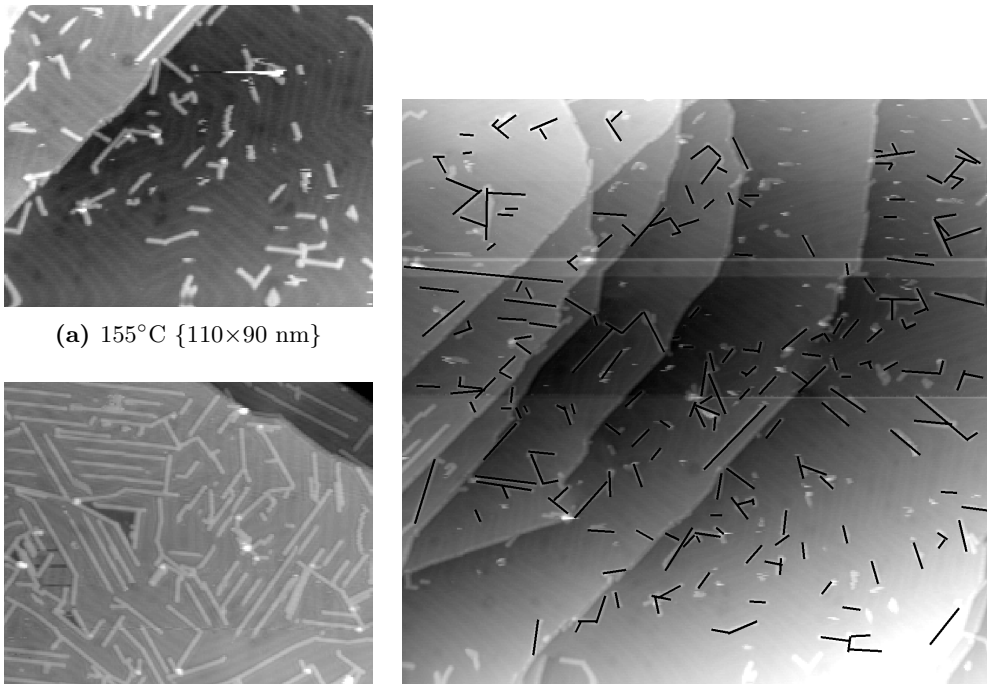

(a) 155°C {110×90 nm}

(b) 196°C {110×90 nm}

(c) 155°C with measured lengths {200×200 nm}

Figure 3.7 7-AGNR samples with different polymerization temperatures as indicated in the subcaptions. (c) Lines with corresponding lengths on top of 7-AGNRs considered for the determination of the average length.

lines on top of 7-AGNRs considered for the determination of the average length. Two cross-linked GNRs were considered as two separate GNRs, as they were separate after the polymerization process. The average lengths of the various preparations are shown in Fig. 3.8. The average lengths of the 7-AGNRs gains until it reaches its maximum value at $T_p = 175°\mathrm{C}$. After that the it reduces in a lower pace. This T_p-dependence is similar to the one in carbon nanotubes grown with a floating chemical vapor deposition process [87]. It seems that there are two competing factors which affect the PA polymer growth. In chemistry, the average length of polymers is usually referred to as degree of polymerization and it eventually determines the average length of the 7-AGNRs. The conclusions drawn on the dependence of the PA polymer on T_p is in agreement with studies on other polymers, where an increase in the lower temperature range corresponds to an Arrhenius-like behavior and a following decrease or a plateau in the higher temperature range [82–86,88,89]. The Arrhenius equation, which the increasing values in Fig. 3.8 were fitted to, describes the relationship between reaction rate R and T_p:

$$R = Ce^{-\frac{E_a}{k_B T_p}}, \tag{3.1}$$

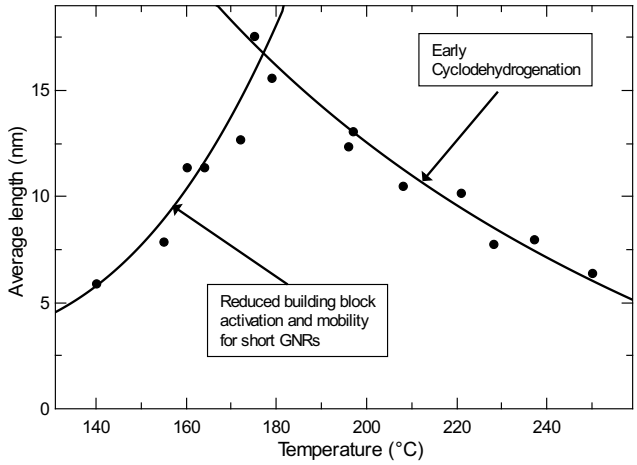

Figure 3.8 Influence of polymerization temperature on 7-AGNR growth. The increasing values have been fitted with the Arrhenius equation (3.1). As a guide to the eye, the decreasing values have been fitted with the Arrhenius equation as well.

with k_B the Boltzmann constant, E_a the activation energy and parameter C, the attempt frequency.

In the PA polymerization there are most likely two effects contributing to the reduced polymerization rate at lower T_p. Relatively low temperatures reduce the mobility and hinder polymers that have surpassed a critical length from diffusing around on the surface. This effectively lowers the chances of assembling long PA polymers and consequently limiting the final length of the 7-AGNRs. When increasing the temperature, it improves the mobility of longer polymers. The diffusion of longer polymer chains across the surface makes residual radical sites more accessible and hence raises the probability to find reaction partners for radical addition. The second contribution is the activation rate of the monomer precursors and the relatively low energy barrier for the carbon-carbon bond formation [42, 75]. The dynamics of the DBBA dehalogenation has been studied with core-level photoemission spectroscopy [76]. In this study, initial dehalogenation is observed at $T_p \approx 130°\text{C}$ on the Au(111) surface, however, the peak associated to the $3d$ levels of bromine atoms, which are linked to the anthryl units, is dominant. This ratio changes with increasing T_p until the bromine on Au(111) peak reaches its maximum at $T_p \approx 180°\text{C}$, while the the other peak has nearly vanished. This means, that the T_p where nearly full dehalogenation is reached coincides with the maximum average length of the final 7-AGNRs. At $T_p = 200°\text{C}$ no traces of bromine atoms linked to the anthryl units were found and at $T_p = 250°\text{C}$ all bromine atoms on Au(111) have been desorped.

Various explanations have been proposed regarding the behavior in the high temperature range, but it is still not fully understood and probably depends on the particular system investigated. In the case of the PA polymer, such a high-temperature effect comes into play at temperatures above 175°C. Sporadic cyclodehydrogenation of single DBBA monomers has been observed after polymerization at 200°C [80]. The hydrogen atoms which are released in the early cyclodehydrogenation are then able to passivate the radical ends of the polymers, thus preventing further radical addition. The decrease in the average length of the 7-AGNRs indicates that this reaction starts to occur at 175°C and becomes more dominant with increasing temperature. Another effect, that might influence the degree of polymerization is the structural stability at higher temperatures. Long polymers may break into two or more smaller ones when the temperature is ramped up to the cyclodehydrogenation temperature [90].

Polymerization reactions are divided into two groups known as step (or condensation) reactions and chain (or addition) reactions. Step reactions require polyfunctional monomers, while chain reactions require an initiation. The formation of PA polymers from DBBA is a chain reaction initiated by the detachment of the two bromine atoms. This means that the initiator and the added monomer units in the so called propagation step are the same and that added growth units can be non-terminated polymer chains, too.

To derive a first size distribution of polymers after a non-selective on-surface polymerization of polymer chains by addition of molecular monomers, thus a chain reaction, at a fixed temperature as the number of monomers increases. During the whole polymerization process, it is assumed that each monomer precursor has equal opportunity to react. With these characteristics, the mole fraction g_l of the final polymers with chain length l can be described by the Flory-Schulz distribution [87, 91],

$$g_l = (1 - \beta)\beta^{l-1}, \tag{3.2}$$

where β is the growth probability factor defined by

$$\beta = \frac{R_p}{R_p + R_t}, \tag{3.3}$$

with the propagation and termination rates R_p and R_t, respectively. In terms of absolute numbers of polymers with length l, the Equation 3.2 becomes [91, 92]

$$N_l = S(1 - \beta)^2\beta^{l-1}, \tag{3.4}$$

which is a simple exponential decay. In this equation, S is a scaling parameter depending on the number of initial monomers. In the original Flory theory, Equation 3.2

was derived for step reactions. However, for the described chain reaction, the same distribution function is obtained.

In the DBBA to PA polymer reaction, not only monomers are added to the a growing chain, but also other polymer chains made up of several monomer units. The longer a polymer is, the lower its attempt frequency, which usually equates to the molecular ground state vibrational frequency. As a result, the longer a polymer is, the lower its opportunities to act as a growth unit. In the case of an inversely proportional dependency between reaction opportunity and growth unit length, Equation 3.4 becomes

$$N_l = S(1-\beta)^2\beta^{l-1}l, \tag{3.5}$$

which shows a linear increase at short lengths and a subsequent exponential decay [91, 93, 94].

The length histograms in Fig. 3.9 show the distributions of the lengths for every prepared sample in the series of measurement. These show that the most likely lengths are around 10 nm and twice as long for preparations with T_p between 164°C and 197°C than with the extremal temperatures. The average length in this temperature range is then distinguished by the number of 7-AGNRs longer than 15 nm. As the distributions show very few short GNRs, which indicates that short polymers can act as growth units with reduced probabilities. However, there is a possibility that single monomers desorb from the surface. Using Equation 3.4, the Flory-Schulz distribution fits in Fig. 3.9 give rise to a T_p-dependence of β which is very similar to the T_p-dependence of the average 7-AGNR length. Equation 3.3 can be rewritten as

$$\frac{1-\beta}{\beta} = \frac{R_t}{R_p}. \tag{3.6}$$

Plotting $\frac{1-\beta}{\beta}(T_p)$ (see Fig. 3.10(a)) reveals a more dominating R_p over R_t until about 180°C. After that, the ratio develops in favor of R_t. In order to fit these data points, an Arrhenius-like behavior of R_p is assumed,

$$R_p = C_p e^{-\frac{E_{a,p}}{k_B T_p}}. \tag{3.7}$$

The initiation rate of the dehalogenation is included in R_p, which comprise all influences of the polymer growth except the termination. It therefore includes all propagation rates of every growth unit, which in principle would have to be considered separately for every size. However, due to the limited amount of data points, it is not possible to include more fit parameter.

A similar Arrhenius-like behavior can be assumed for R_t. However, one contribution to R_t is the termination by defective monomer units, which is independent of T_p.

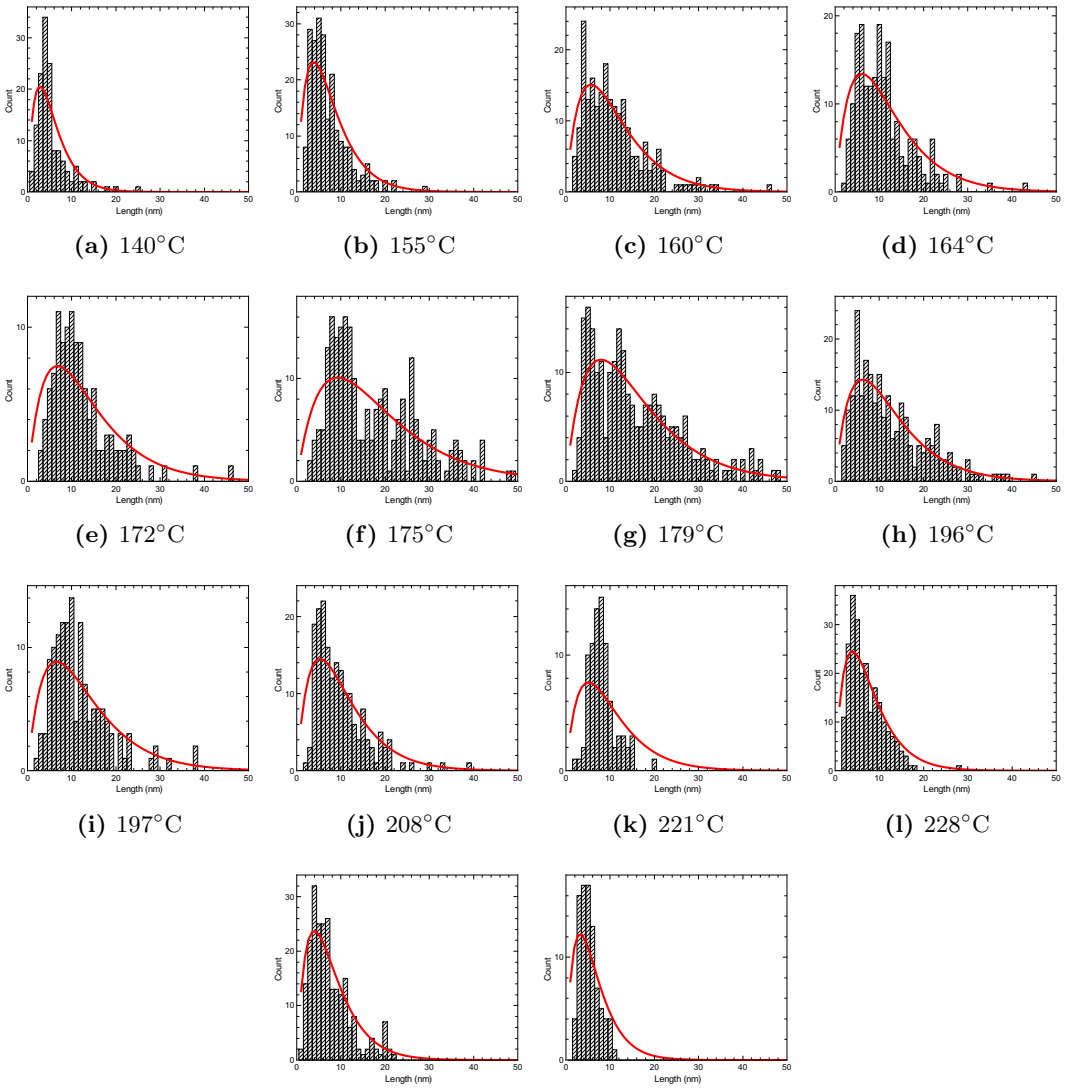

(a) 140°C **(b)** 155°C **(c)** 160°C **(d)** 164°C

(e) 172°C **(f)** 175°C **(g)** 179°C **(h)** 196°C

(i) 197°C **(j)** 208°C **(k)** 221°C **(l)** 228°C

(m) 237°C **(n)** 250°C

Figure 3.9 Polymerization temperature histograms as indicated in the subcaptions and their Flory-Schulz distributions fitted with Equation 3.5.

Therefore a constant parameter R_{t0} has to be added to the otherwise Arrhenius-like behavior of R_t,

$$R_t = R_{t0} + C_t e^{-\frac{E_{a,t}}{k_B T_p}}. \tag{3.8}$$

Fitting $\frac{R_t}{R_p}(T_p)$ to $\frac{1-\beta}{\beta}(T_p)$ with the values for β extracted from the fits to the histograms in Fig. 3.9 results in the curve shown in Fig. 3.10(a). As R_{t0}, C_t and C_p can be multiplied by the same number without changing the fitted curve, C_p was set to $10^{13}\ \frac{1}{\mathrm{s}}$, which corresponds to the vibrational frequency of small molecules and is typically taken as attempt frequency. The fit reveals the activation energies for R_p

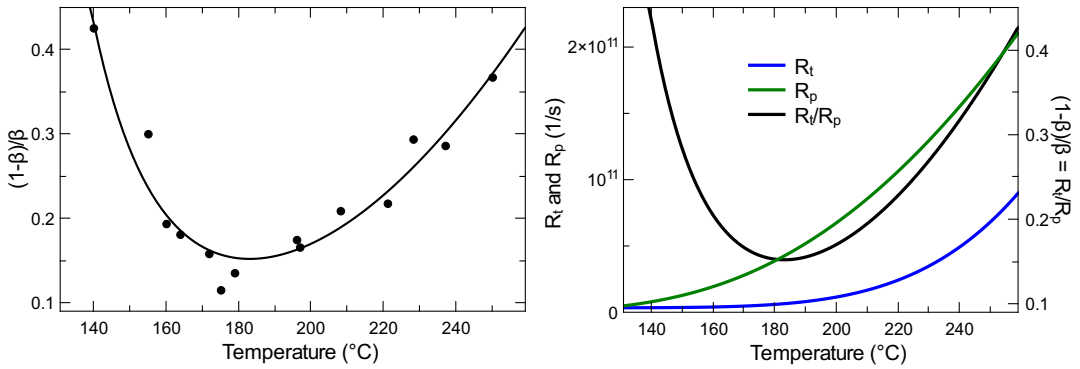

(a) Arrhenius-fit and experimental data

(b) Arrhenius-fit and its components

Figure 3.10 Arrhenius-fit to $\frac{R_t}{R_p}$. (a) $\frac{1-\beta}{\beta}$ as a function of T_p and Arrhenius-fit with Equations 3.6, 3.7 and 3.8. (b) R_t, R_p (left axis) and $\frac{R_t}{R_p}$ (right axis) as a function of T_p using the values of β extracted from the fits in Fig. 3.9 and from the Arrhenius-fit in (a).

($E_{a,p}$ = 86 meV) and for R_t ($E_{a,t}$ = 179 meV). The diffusion barrier for phenyls on Au(111) is 220 meV, which indicates, that the stabilizing organometallic complex is significantly weaker for the biradical monomer. At about 160°C the temperature dependent termination reaction comes into play and starts to reverse the increasing average length at around 180°C. As discussed earlier, sporadic cyclodehydrogenation and subsequent hydrogen passivation of the radical ends has been observed after polymerization at 200°C [80] and is most likely the reason for the temperature dependent part of R_t in addition to the temperature independent termination by defective monomer units. An energy barrier of 1.35 eV for the cyclodehydrogenation was revealed by DFT calculations [75] which is significantly higher than $E_{a,p}$ = 179 meV obtained from fitting $\frac{R_t}{R_p}(T_p)$. In the DFT calculations, a perfect Au(111) surface without herringbone reconstruction was assumed. The large difference to the experimental values strongly indicated, that the cyclodehydrogenation is aided by surface step edges and the herringbone reconstruction, especially the kinks the in the reconstruction generally show an increased reactivity. This is also supported by the observation that the early cyclodehydrogenation occurs mostly in uncoupled monomers which have the lowest diffusion barrier and are therefore more likely to encounter the reaction aiding positions on the surface.

In contrast, the cyclodehydrogenation temperature does not have an influence on the length of the 7-AGNRs. Going to temperatures higher than 350°C removes small defect molecules from the surface but increases the number of cross links between 7-AGNRs. In the temperature range up to 400°C the observed differences are minor.

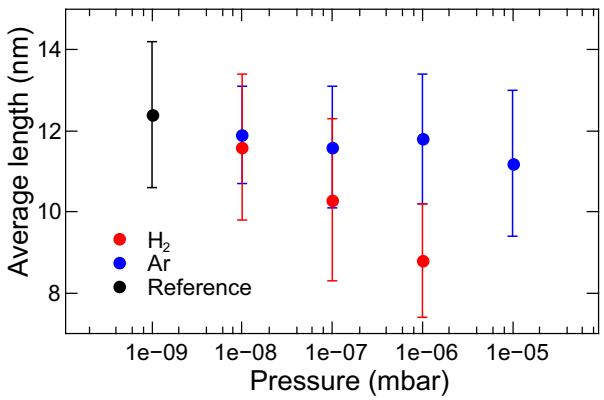

Figure 3.11 Influence of hydrogen and argon on 7-AGNR growth. The reference sample was prepared at base pressure and at $T_p = 190°C$.

Going above this temperature, initial cross-coupling reactions between GNRs occur which will be discussed in Section 3.3.

A less obvious structural reaction than the fusion of GNRs happens at the termini. Staying close to 350°C results in a majority of H_2 termini in favor of H_1 termini. This distribution can be balanced or inverted by prolonging the cyclodehydrogenation step or by increasing the temperature. This agrees with calculations, that a H_2 terminus is slightly more stable than a H_1 terminus [80]. However, when a H_2 terminus has lost one hydrogen due to the thermal energy in the system, it will not find another hydrogen instead. Because of the irreversibility of the process, a longer or higher annealing will result in a more H_1 dominated distribution.

Hydrogen partial pressure

The termini are passivated with hydrogen which originates as a by-product of the cyclodehydrogenation. As the fabrication of of 7-AGNRs is done under UHV conditions and the polymerization process is no longer than 15 minutes, ambient hydrogen was excluded as a source of hydrogen, that passivates the radicals and stops the polymerization. Increasing the hydrogen partial pressure leads to an increased number of hydrogen molecules that hit the surface and increase the probability of reacting with the radical monomers, ultimately stopping the polymer growth.

Figure 3.11 shows the influence of an increased hydrogen partial pressure up to 10^{-6} mbar during polymerization on the average length of the final 7-AGNRs and a comparison to a reference sample that was prepared in UHV conditions. The fabrication temperatures for all samples in this series were 190°C and 370°C for 10 minutes each. The average length is clearly reduced by the hydrogen partial pressure and drops

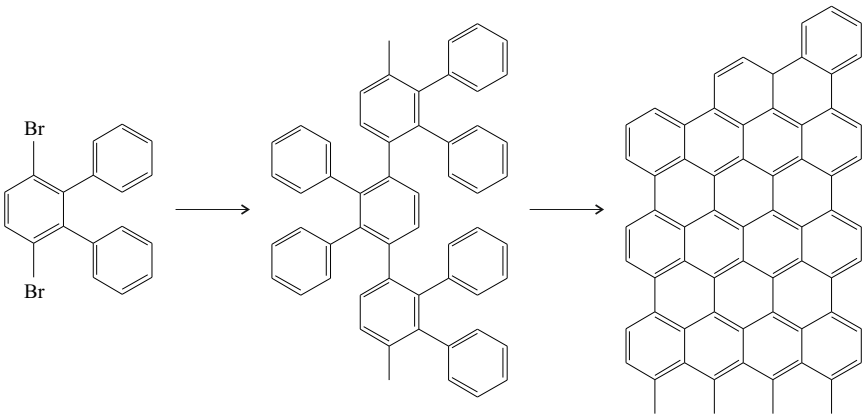

Figure 3.12 Reaction scheme from DBTP via the polymer to 9-AGNR.

about 30% at 10^{-6} mbar compared to the reference. This strongly indicates that a H_2 that hits the surface in the vicinity of a radical reacts with it, hence stopping polymer growth at this position. Hydrogen desorbs at $-162°C$ off a Au(111) surface [95], which means no hydrogen will stay on the surface, but the residence time on the surface at the temperatures of polymerization is sufficient to couple to the radical position of a growing polymer. Consequently, increasing the hydrogen partial pressure leads to an increased number of hydrogen molecules that hit the surface and passivate a radical.

In order to exclude that the reduced average length is not a purely pressure related effect, the same preparation series has been done with argon, which is unlikely to take part in any chemical reaction. The results are shown in the same graph than the ones for the hydrogen series (Fig. 3.11). A small reduction in the average length can be observed, too, but the reduction is significantly lower and well within the error. This means, the pressure related effect on the average length in the hydrogen series can be neglected.

3.2 $N = 9$ armchair graphene nanoribbons

The precursor monomer 3',6'-dibromo-1,1':2',1"-terphenyl (DBTP) was used to fabricate $N = 9$ armchair graphene nanoribbons (9-AGNRs). The design of the molecule follows the same ideas as in the design of DBBA: Two coupling positions by halogen addition to form a polymer chain and an arrangement of the benzene rings that prevents the radical monomers from coupling the wrong way. The DBTP monomers loose their bromine which are located on opposite carbon atoms of a benzene ring. By radical addition, these benzene rings form a central oligophenyl that acts as the spine of the polymer. Every benzene ring in the chain is extended with two phenyl groups

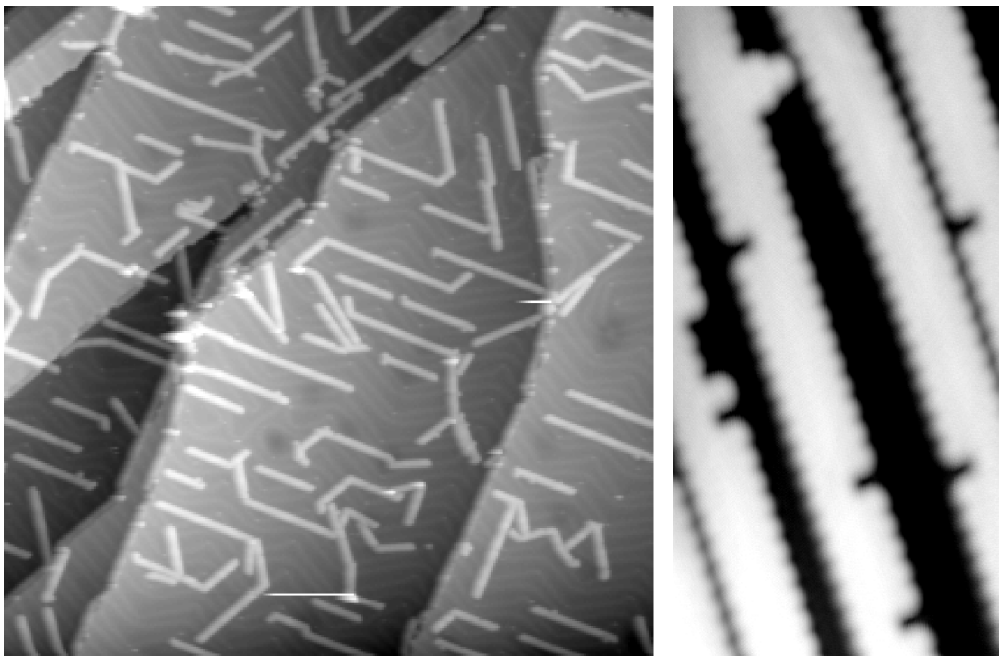

(a) Overview {140×140 nm} **(b)** Defects {5×10 nm}

Figure 3.13 Overview of 9-AGNRs on Au(111) using (a) highly purified monomers and (b) simply purified monomers, which show a high number of defects.

on one side forming an ortho-terphenyl. This forces the radical monomers to form the central chain in the way that the two phenyl groups of each monomer are on opposing sides compared to the next monomer. After cyclodehydrogenation the polymer then becomes a 9-AGNR. This reaction, with chemical models of DBTP, the polymer and the final 9-AGNR, is illustrated in Fig. 3.12. It also illustrates the 120° armchair end of the 9-AGNR.

The practical surface-assisted fabrication of 9-AGNRs done in two steps, similar to the fabrication of 7-AGNRs. The only experimental differences between the two fabrications are DBTP's lower sublimation temperature of 85°C and a higher annealing temperature of 350°C in order to induce cyclodehydrogenation. On a prepared sample, the 9-AGNRs are isolated and spread out over the Au(111) surface as shown in Fig. 3.13(a). However, when analyzing the fabrication by subsequently increasing the annealing temperature, one finds two intermediate states between the initial monomer and the final ribbon. The quality of the monomer precursors plays a significant role for the final 9-AGNRs. Monomers that have only undergone simple purification feature numerous defects as exemplified in Fig. 3.13(b)

In a first step, DBTP is thermally sublimated onto the Au(111) surface at an

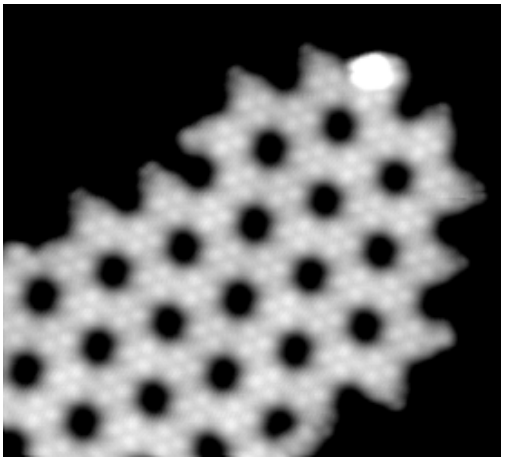

(a) $T < 250°C$: Precursor monomer islands {19×17 nm}

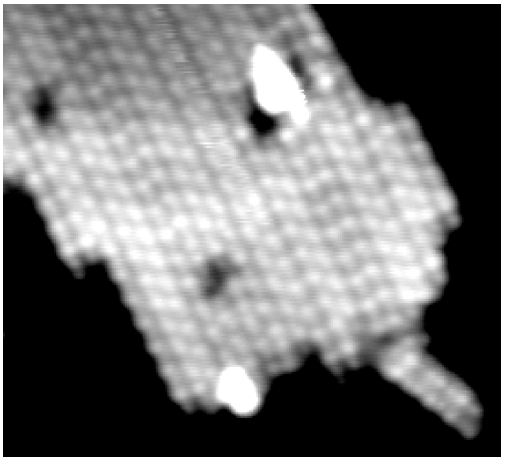

(b) $250°C < T < 300°C$: Polyanthracene polymer islands {19×17 nm}

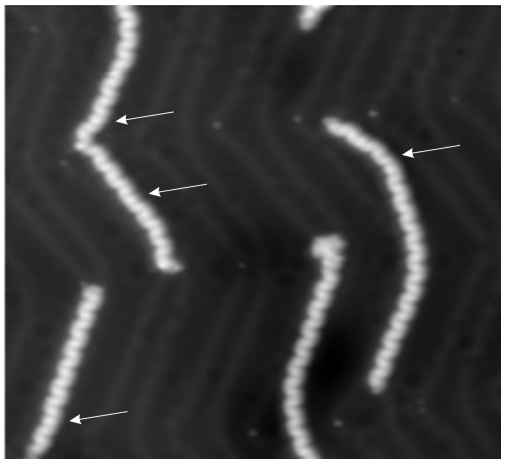

(c) $300°C < T < 350°C$: Partially cyclodehydrogenated polymer {52×47 nm}

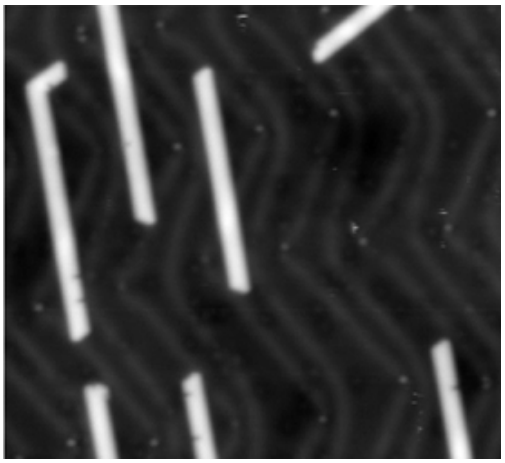

(d) $T > 350°C$: Flat $N = 9$ AGNRs {52×47 nm}

Figure 3.14 Steps in DBTP to 9-AGNR reaction. (a) Highly ordered islands of DBTP monomers. (b) Islands of polymers. (c) Separated partially cyclodehydrogenated polymer chains. The white arrows point to grain boundaries of the $4a$ features. (d) Fully cyclodehydrogenated 9-AGNRs.

evaporation temperature of 85°C. If the sample temperature does not exceed 250°C, they form highly ordered porous islands, as shown in Fig. 3.14(a). The islands show a six-fold symmetry and trimers are surrounding the holes. No preferential orientations of the islands on the Au surface or alignment due to the herringbone reconstruction are observed. The apparent height of the trimers is 0.30 ± 0.02 nm and the distance between neighboring holes is 2.65 ± 0.05 nm. The apparent height suggests the phenyl group pairs standing on the surface at an angle of maximum 45°. Figure 3.15(a) displays the arrangement of the monomers with a partly overlaid molecular model and DFT-based STM simulation which includes the relaxation of the structure on the surface. Three monomers are assembled with one phenyl group each facing the center of the assembly. This way the outermost hydrogen of a phenyl group is pointing towards the flat center of a neighboring phenyl group, similar to the arrangement in crystalline benzene [96]. The DFT simulation revealed that one phenyl group is further rotated and hence standing more upright than the second one. As the intensity in the STM simulation is slightly shifted to the more upright standing phenyl group, it is most likely the one facing the center of the trimer assembly. Additionally, the more rotated phenyl groups would be closer to the stabilizing benzene crystal structure.

It is not clear whether both bromine atoms are still attached to the monomer at temperatures up to 250°C. In comparison, the 7-AGNR precursor DBBA fully dehalogenates at 175°C as it was discussed in the previous section. The monomers, which form highly ordered porous islands self-assemble, but do not form covalent bonds and therefore fully dehalogenated monomers are unlikely. The third possibility is the dissociation of one of the two bromine atoms. The radical position would be stabilized by the creation of an organometallic complex, while tilting the central benzene ring, similar to the bromobenzene example presented in Section 1.5. This lifts up the second bromine atom from the surface. This increases the energy barrier for dehalogenation, as the catalyzing interaction with the metal surface is reduced. The porous monomer islands are formed within an annealing temperature range of $30°\text{C} \leq T \leq 250°\text{C}$. No dehalogenation has its critical temperature in this range, which implies, that either one bromine atom dissociates at a very low temperature or both bromine atom dissociate together at relatively high temperatures. A comparison to the dehalogenation of DBBA is difficult because the structure of the DBTP clearly changes the radical stabilization by the metal surface.

Surpassing 250°, the precursor monomers loose their bromine atoms and the following radical addition results in polymer chains. They assemble into islands similar to the PA polymers that are formed from DBBA [43]. Figure 3.14(b) shows an example of such an island. The apparent height of the islands is reduced to 0.24 ± 0.02 nm

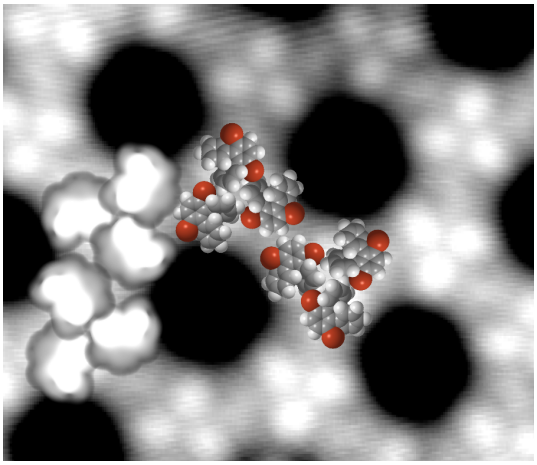

(a) $N = 9$ precursor monomer {5.0×4.3 nm}

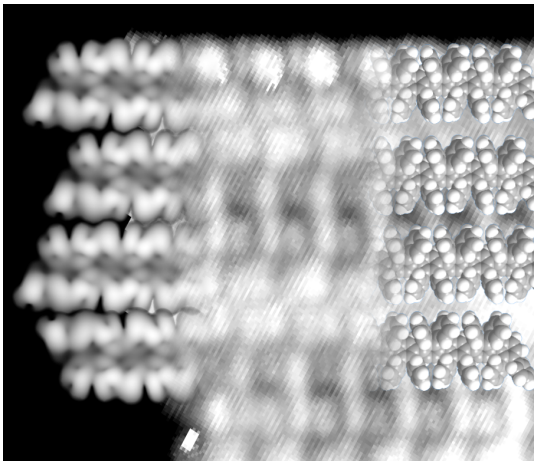

(b) $N = 9$ polymer {7.3×6.3 nm}

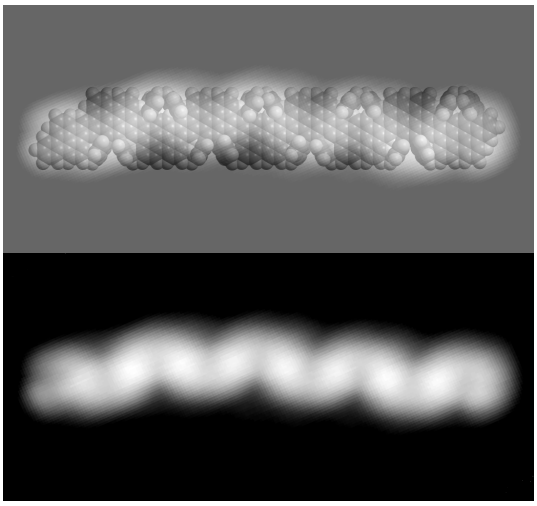

(c) $N = 9$ partial polymer {9.2×8.6 nm}

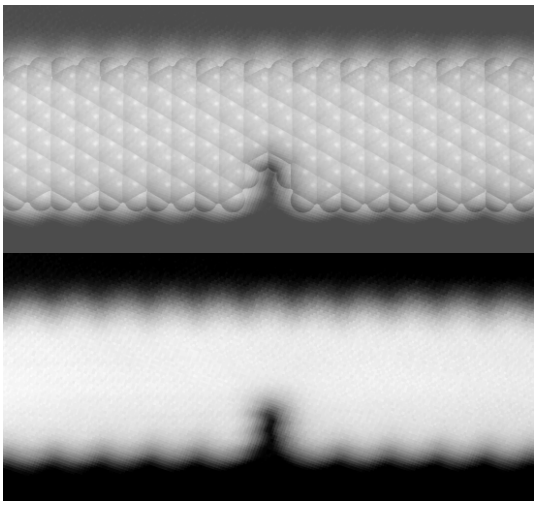

(d) $N = 9$ armchair GNR {4.7×4.4 nm}

Figure 3.15 Structures of the four steps in the 9-AGNR synthesis. (a) High resolution STM image of DBTP monomer island with partly overlaid DFT-based STM images (left) and molecular models (right). (b) High resolution STM image of a polymer island with partly overlaid DFT-based STM images (left) and molecular models (right). (c) Molecular model of the proposed chemical structure of partially cyclodehydrogenated polymers overlaid with a corresponding, transparent STM image (top) and the non-transparent STM image (bottom). (d) Molecular model of a 9-AGNR section with a cavity defect overlaid with a corresponding, transparent STM image (top) and the non-transparent STM image (bottom).

which means the phenyl groups are now standing at a lower angle to the surface. The assembled polymers are straight and they have a distance of 0.86 ± 0.02 nm between features, which is in line with the predicted dimensions of the polymers according to the distances in benzene ring chains. Figure 3.15(b) displays the structure of the polymers with partly overlaid DFT-based STM simulations and surface relaxed molecular models. The center of a polymer chain shows a trench where the central oligophenyl chain lies on the Au(111) surface. The higher sides are the still unreacted phenyl groups. Despite the symmetry of the phenyl group pairs from the initial monomer, one is standing more upright than the second one, which is found in the experimental and DFT-based STM images.

Further annealing to over 300°C results in partially cyclodehydrogenated polymers that appear as isolated, flexible chains that prefer the hcp areas of the Au herringbone reconstruction (see Fig. 3.14(c)). The chains exhibit a corrugated zigzag pattern along the central carbon chain. The period of the corrugation is 1.81 ± 0.05 nm and the apparent height is 0.27 ± 0.02 nm, thus larger compared to the one of the pure polymer. The period of corrugation corresponds to $4a$ a two times larger unit cell compared to the polymer. Despite the very symmetrical appearance in STM images, the chemical structure cannot be symmetric with a feature size that involves four initial monomers. Even with various scanning setpoints and tip shapes, it has not been possible to increase the resolution of the partially cyclodehydrogenated polymer in STM. Taking all known information about the chains into account, a possible chemical structure is proposed in Fig. 3.15(c), where a model is transparently overlaid by an STM image of a short partially cyclodehydrogenated polymer chain. The cyclodehydrogenated parts from a wave-like flat ribbon. In each chevron of the wave-like ribbon are two, upwards standing, unreacted phenyl groups. However, they are either pointing towards each other or away from each other depending on the side of the chain. The observed zigzag pattern follows the unreacted phenyl groups and is in antiphase with the wave-like flat ribbon. The $4a$ features have grain boundaries as indicated with the white arrows in Fig. 3.14(c). This indicates that the partial cyclodehydrogenation of the polymer started at various positions but the distance between the initial reaction sites did not always match a multiple of $4a$.

The geometrical design of the polymer yields flat, straight and atomically precise 9-AGNRs with an apparent height of 0.18 ± 0.02 nm after cyclodehydrogenation at temperatures above 350°C (Fig. 3.14(d)). In this step all inner hydrogen atoms that were left detach, enabling bond formation.

Some 9-AGNRs feature cavity defects as shown in Fig. 3.15(d) with a model and an overlaid, transparent STM image. These cavities are a result of the separation

of phenyl groups. Upon extensive purification by six times recrystallization of the DBTP powder, a significant reduction of the number of defects was observed. Defects resulting from flawed monomers are already apparent as darker spots in STM images of polymer chain islands as it can be observed in Fig. 3.14(b). The number of defects in the final 9-AGNRs, however, outnumber the defects in the polymer chains prior to cyclodehydrogenation. As the purity might be critical to the quality of the 9-AGNRs, it is most likely not the only factor. One experimental factor is the thermal energy in the system that drives the cyclodehydrogenation. The phenyl groups are connected by carbon-carbon single bonds to the central benzene ring. The average binding energy of such a bond is 3.61 eV, which is lower than the binding energy of carbon-hydrogen bonds which are broken up during cyclodehydrogenation (4.29 eV). Based on these numbers, the phenyl groups would be expected to detach before the hydrogen atoms. The values, however, do not account for the assistance or hindrance of the Au(111) surface and the geometry of the molecule. For the cyclodehydrogenation the surface acts as a catalyst, which leads to the observation, that cyclodehydrogenation does not occur in second layer polymers within the usual temperature window [43, 75].

Incomplete cyclodehydrogenation

When performing the cyclodehydrogenation close to the threshold temperature for the usual time of about ten minutes, non reacted parts can be found in the 9-AGNRs. These non reacted parts are neighboring phenyl groups showing up as a pair of bumps on the same side of a GNR as depicted in Fig 3.16(a) and (c). This is similar to the partial cyclodehydrogenation observed in 7-AGNRs [75]. There two cyclodehydrogenated antracene groups, lower the activation energy for the neighboring antracene groups, causing a knock-on effect, as it was shown in Fig. 3.3. Therefore, the partially cyclodehydrogenated 7-AGNRs have extended sections of neighboring, non-reacted antracenes. In contrast, the phenyl group pairs of the incompletely cyclodehydrogenated 9-AGNRs are distributed randomly. Taking into account the position of two opposing phenyl pairs in Fig 3.16(a), it implies that these features were at a position of a grain boundary of the partially cyclodehydrogenated polymer's $4a$ zigzag feature. Cyclodehydrogenating the phenyl pairs via annealing, may result in the observed cavity defects as shown in Fig. 3.15(d).

In the previous section, it was shown that it is possible to induce dehydrogenation at the termini of a H_2 terminated 7-AGNR with an STM tip. A similar electron-stimulated cyclodehydrogenation can be imagined for the phenyl group pairs of a incompletely dehydrogenated 9-AGNR. Such an electron-stimulated cyclodehydrogena-

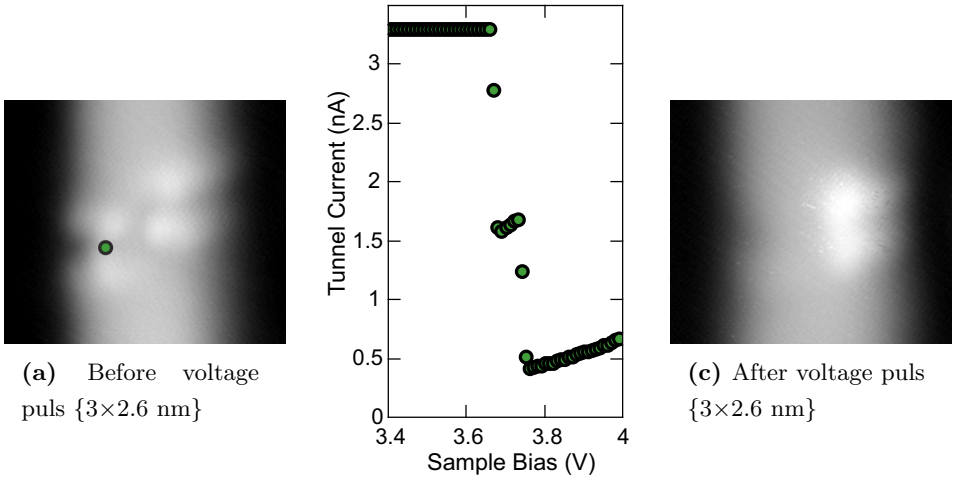

(a) Before voltage puls {3×2.6 nm}

(b) Voltage puls

(c) After voltage puls {3×2.6 nm}

Figure 3.16 Electron-induced cyclodehydrogenation. (a) STM image of a incompletely cyclodehydrogenated 9-AGNR segment. (b) $I_t(V_B)$ curve of voltage ramp driven at the position marked in (a). (c) STM image of the same 9-AGNR segment after the voltage ramp.

tion has also been performed successfully for the 7-AGNRs [75]. The STM tip is positioned above the phenyl group pair as indicated in in Fig. 3.16(a), a voltage ramp is then performed while keeping the height constant (Fig. 3.16(b)). After two consecutive jumps at about 3.7 eV in the $I_t(V_B)$ spectrum, the phenyl group pair has disappeared (Fig. 3.16(c)). The electron energy required for this electron-stimulated reaction is higher than in the 7-AGNR case (2.6 eV [75]) which is in agreement with the higher temperature needed for cyclodehydrogenation.

Termini

As a result of the structure of the DBTP, the two termini of a 9-AGNR are composed of 120° armchair edges. Both STM and nc-AFM images in Fig. 3.17 show no difference between the the long armchair edge and the 120° terminus armchair edge. Based on these images, it can be assumed that the position where the bromine atom was attached in the initial precursor monomers is passivated with a single hydrogen atom. The source of the hydrogen is sporadic cyclodehydrogenation of single DBTP monomers which occurs below the temperature of polymerization (Fig. 3.17(c)). Similar to the passivation of 7-AGNRs, the detached hydrogen atoms can diffuse around the surface until they find a radical position or desorb from the surface.

The addition of a second hydrogen atom at the same site, resulting in a H_2 termi-

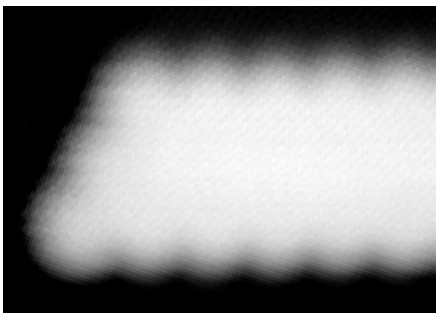

(a) STM {2.6 × 1.8 nm}

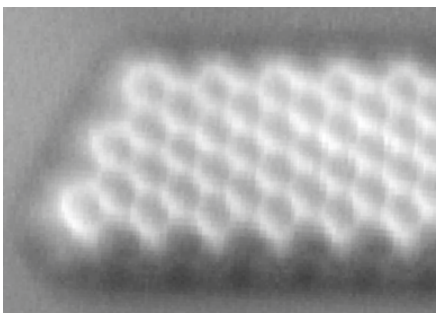

(b) nc-AFM {2.6 × 1.8 nm}

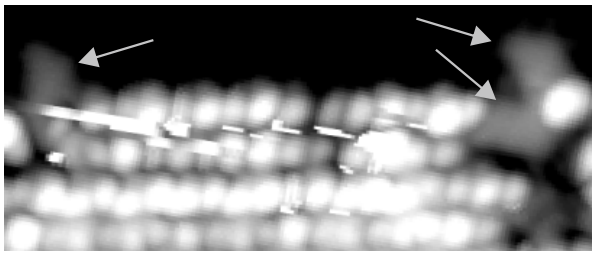

(c) Sporadic cyclodehydrogenation {9.1 × 3.9 nm}

Figure 3.17 9-AGNR termini imaged with STM (a) and nc-AFM (b). (c) STM image of a polymer island on a sample annealed to 275°C. Arrows point to small structures with an apparent height of 0.17 nm, indicating that they already have undergone cyclodehydrogenation.

nation, similar to the H_2 termination in 7-AGNRs, is hindered by the energy barrier of 0.99 eV to form an sp^3 carbon at an armchair edge [75]. Additionally, the Gibbs free energy would only be smaller and thus the stability higher for partial pressures of H_2 higher than 1 bar at typical temperatures of cyclodehydrogenation [97, 98]. These obstacles are evidently too high under the given conditions and no other than H_1 termini have been found.

Raman spectroscopy

Raman spectroscopy is a vibrational spectroscopic technique for analyzing molecular motion and is used for fingerprinting molecular species by which molecules can be identified. It measures inelastic scattering of monochromatic light, usually from a laser, in a spectral range between near infrared and near ultraviolet. The photons interact with molecular vibrations, phonons and other excitations in the system, which shifts the energy of the photons. The scattered photons, if in an applicable energy range, reveal the resonant frequencies of vibrational modes in the system [99].

The Raman spectrum of a densely packed layer of 9-AGNRs a Au(111) single-

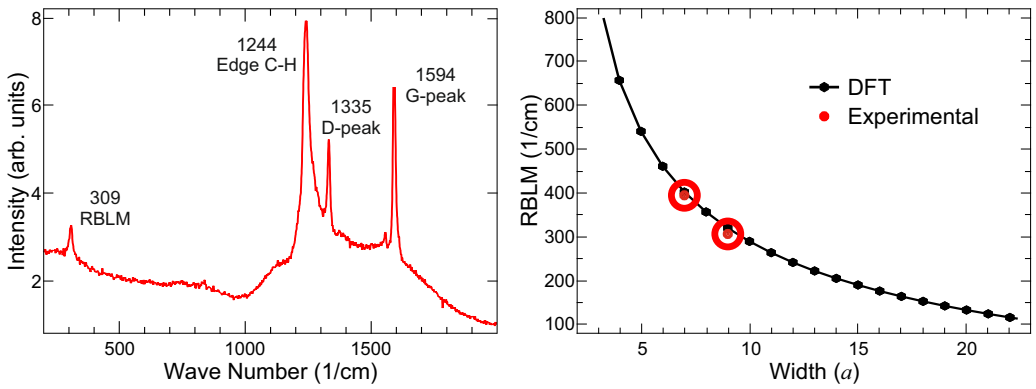

(a) Raman spectrum **(b)** RBLM peak positions

Figure 3.18 Raman spectroscopy on 9-AGNRs. (a) Raman spectrum of straight densely packed 9-AGNRs on Au(111) using 785 nm laser light. The peak at 309 $\frac{1}{\text{cm}}$ is characteristic for a radial vibration of the 0.99 nm wide 9-AGNR. (b) The experimentally obtained RBLM peak positions of the 7- and 9-AGNRs in comparison to a DFT simulations.

crystal substrate in Fig. 3.18(a) reveals several peaks, including the D- and G-peak. [100]. The peak with the lowest wave number, 309 $\frac{1}{\text{cm}}$, corresponds to the width-specific radial-breathing-like mode (RBLM). Figure 3.18(b) shows a calculated evolution of the RBLM peak position of armchair GNRs with increasing width [101]. In this graph, the experimental value is marked together with the experimental value obtained for the 7-AGNRs, 396 $\frac{1}{\text{cm}}$ [43]. The measured peak positions are in excellent agreement with the DFT calculations and attests the uniform width of the 9-AGNRs.

3.3 Fusion of armchair graphene nanoribbons

Annealing to 450°C or higher leads to the fusion of armchair GNRs which is a conjugation side-by-side via dehydrogenation. 7-AGNRs will result in $N = 14$, $N = 21$ and sometimes even wider armchair GNRs, analogously, 9-AGNRs will result in $N = 18$, $N = 27$ armchair GNRs. Because this is a reaction which is not programmed into the initial precursor monomers, there is no control over the length and alignment of the reactants, except they need to be side-by-side.

As it has been discussed in Section 1.5, carbon-hydrogen bonds have a binding energy of 4.29 eV, which is higher than the carbon-carbon bond energies [41]. When annealing the sample, the edge carbon-hydrogen bonds are therefore likely to be broken at lower temperatures than the inner GNR carbon-carbon bonds. After dehydrogenation of the edges, inter-GNR carbon-carbon bonds are formed resulting in cross links

or GNRs of double width. The mechanism behind this reaction is still unclear. For pentacene molecules (another graphene based nanostructure) it has been proposed that a hydrogen is transferred from one pentacene to an abutted pentacene, resulting in a radical on one and a local two-hydrogen passivation on the other pentacene. Subsequently, a molecular hydrogen splits, creating a second radical position. Via radical addition the two pentacenes can then form a carbon-carbon bond between them and lower the activation energy for the same reaction on the neighboring hydrogen positions [102]. It is likely that the same mechanism happens in the fusion reaction of two or more armchair GNRs. A mechanism in which the hydrogen detaches without the assistance of a abutted GNR is unlikely because the fused GNRs show clean hydrogen passivation. Additionally, a temperature of about 500°C is needed for dehydrogenation of flat graphene-based structures on a Cu(111) surface, which has a significantly higher catalytic activity than a Au(111) surface [103].

It has been proposed, that on a Ag(111) surface the synthesis of wide armchair GNRs from DBBA is a single two-dimensional growth step starting from the radical monomers [104]. This is clearly not the case on Au(111), on which the growth is in the direction of the radical monomer's armchair edges creating 7-AGNRs. In a second step wide GNRs are formed by fusing together the GNRs at their armchair edge. Taking all observations into account, a fusion mechanism of armchair GNRs on Au(111) is proposed in Fig 3.19. It follows the proposed mechanism for the fusion of pentacenes [102].

The thermal reactivity of polyaromatic hydrocarbons has been studied, for which the carbonization via hydrogen transfer is monitored by differential thermal analysis [105]. High mechanical pressures produce graphitic species and dihydrogenated and tetrahydrogenated byproducts from polyacenes via hydrogen transfer [106]. Additionally, in the fusion reaction of pentacenes, calculations have shown that each successive bond delivers a greater enthalpy, assuming a symmetrical order of bond formation. In this regard, it is reasonable to consider the individual steps of a zipper reaction in Fig. 3.19(a)-(f) that fuse two armchair GNRs into one of with the summated width of the initial GNRs. The actual mechanism may involve a number of different intermediates with differing fusion points, although initial reaction at the end of one GNR represents a plausible starting point. As a first step, a hydrogen is transferred from one GNR edge to the first carbon position of the other GNR armchair edge or the other way around. This results in a radical on one and a local two-hydrogen passivation on the other GNR edge (Fig. 3.19(b)). The yielded hydrogen pair then splits as molecular hydrogen, creating a second radical position (c). Via radical addition a carbon-carbon bond is formed between the radical positions (d). This likely

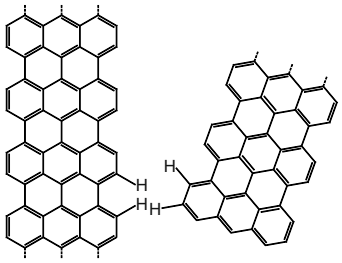

(a) Abutting GNRs

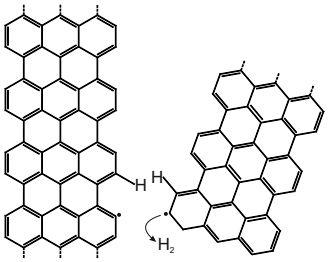

(b) Hydrogen transfer

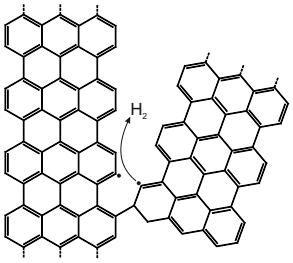

(c) Detachment of molecular hydrogen

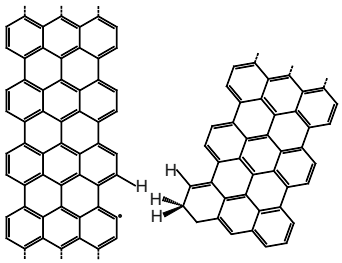

(d) Radical addition and hydrogen transfer

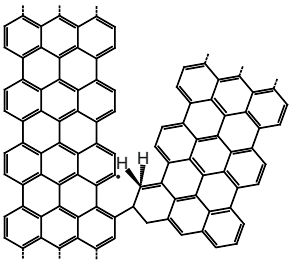

(e) Detachment of molecular hydrogen

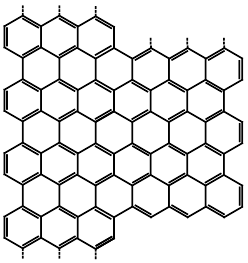

(f) Fully fused GNR

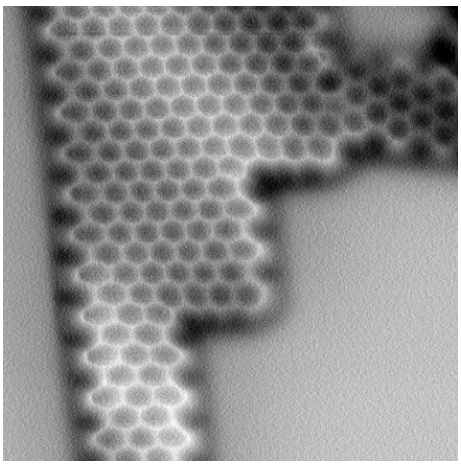

(g) $N = 7, 14, 21$ $\{4.5 \times 4.5$ nm$\}$

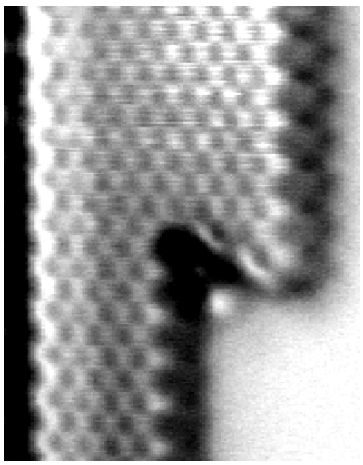

(h) $N = 9, 18$ $\{3.5 \times 4.5$ nm$\}$

Figure 3.19 Fusion of armchair GNRs. (a)-(f) Proposed reaction mechanism for the fusion of armchair GNRs via hydrogen transfer and radical addition. (g) nc-AFM image of a fused GNR with 7-, 14- and 21-AGNR sections and a cross-linked 7-AGNR showing a pentagon and a heptagon at the connection point. (h) nc-AFM image of a fused GNR with 9- and 18-AGNR sections.

lowers the activation energy for the same reaction on the neighboring hydrogen positions (e). The timing of the second hydrogen transfer may be different and vary along the zipper reaction. Ultimately, the zipper reaction leads to a fully fused GNR (f)-(h).

Cross-coupling is expected to follow the same reaction mechanism. In case of zigzag termini cross-coupling occurs at lower temperature than in the armchair-armchair edge fusion case. This observation is coherent, as a two-hydrogen passivation on a zigzag edge lowers the energy, while it increases the energy on an armchair edge, see the discussions about the termini in sections 3.1 and 3.2. An example of cross-coupling can be seen in Fig. 3.19(g). Here, where a zigzag termini cross-links to an armchair edge, creating pentagons and heptagons [107, 108].

Chapter 4

Electronic Structure

For the utilization of the prepared GNRs, their electronic properties need to be known. There are several theoretical studies about various properties of the GNRs. The ones about the electronic properties have been reviewed in Chapter 1. However, experimental confirmation is still due for the vast majority of GNR structures. The main obstacle is of course the fabrication of GNRs, which are limited to a small number of GNRs so far.

In this chapter Fourier-transform scanning tunneling spectroscopy (FT-STS) will be introduced in detail and applied to 7-AGNRs and 9-AGNRs whose fabrications were discussed in Chapter 3. The STS technique measures single GNRs of known length and makes use of scattering processes at the termini. Therefore, the band gap as a function of length and the influence of the termini will be presented before.

4.1 $N = 7$ armchair graphene nanoribbons

Shortly after the first report about the fabrication of 7-AGNRs, the electronic structure has been studied. At first, simple STS measurements revealed an electronic band gap E_g of 2.3 eV [109] and 2.5 eV [110], respectively. Here the difference is a result of different perceptions where to pinpoint the position of the electronic state in an STS spectrum. In the former one, the energetic positions of the half height of the onsets were used to determine the band gap, while in the latter one the peak positions was used. For the effective mass of the valence band m^*_{VB} values of sizeable difference have been reported ranging from $m^*_{VB} = 0.21\ m_e$ [109] to $m^*_{VB} = 1.07\ m_e$ [78] and $m^*_{VB} = 1.37\ m_e$ [111], where m_e is the free electron rest mass. The first two values were measured with angle-resolved photoelectron spectroscopy, which can directly access the averaged occupied band structure of the 7-AGNRs within the photon beam.

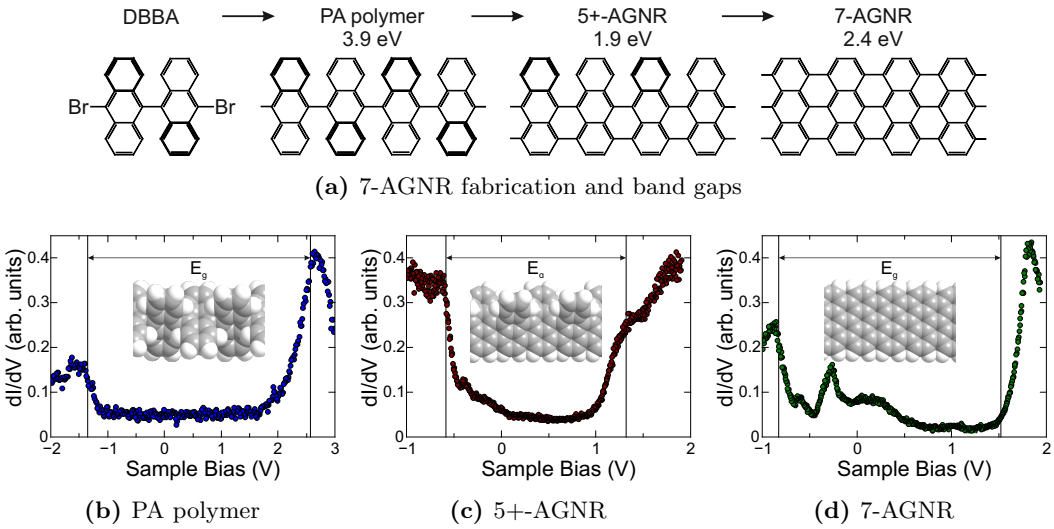

(a) 7-AGNR fabrication and band gaps

(b) PA polymer **(c)** 5+-AGNR **(d)** 7-AGNR

Figure 4.1 Stable, elongated structures during the 7-AGNR synthesis. (a) Fabrication steps on the 7-AGNR synthesis from DBBA. The band gaps are given for all stable structures on Au(111). (b)-(d) Single $\frac{dI_t}{dV_B}(V_B)$ spectra recorded on a PA polymer, the flat side of a 5+-AGNR and a 7-AGNR, respectively. The vertical lines mark the onsets of the VBs and CBs.

The reason for the conflicting results can only be speculated from the outside. Only the fact that in both reports the samples were grown ex-situ can be pointed out as a possible source of error. The latter of the three results was obtained by angle-resolved two-photon photoemission spectroscopy which also revealed an effective mass of the conduction band of $m^*_{CB} = 1.35\, m_e$. However, the 7-AGNRs under study were orientated randomly which puts the results into question, as the alignment is of high importance in this technique.

4.1.1 Electronic versus optical band gap during synthesis

In Section 3.1 the synthesis of 7-AGNRs from DBBA has been discussed in detail. Three stable one-dimensional structures occur during the process: the PA polymer, the partially cyclodehydrogenated polymer (5+-AGNR) and the final 7-AGNR. Figure 4.1(a) depicts models of the three structures with the electronic band gap on Au(111) extracted from the STS spectra shown in Fig. 4.1(b)-(d) .

Fitting band onsets from a single $\frac{dI_t}{dV_B}(V_B)$ spectrum is not straightforward. In the case of the here presented one-dimensional structures, the LDOS has van-Hove singularities which diverge proportional to $\frac{1}{\sqrt{E}}$ for a band onset at $E = 0$. Broadening arises due to several aspects. Experimentally, major broadening arises from

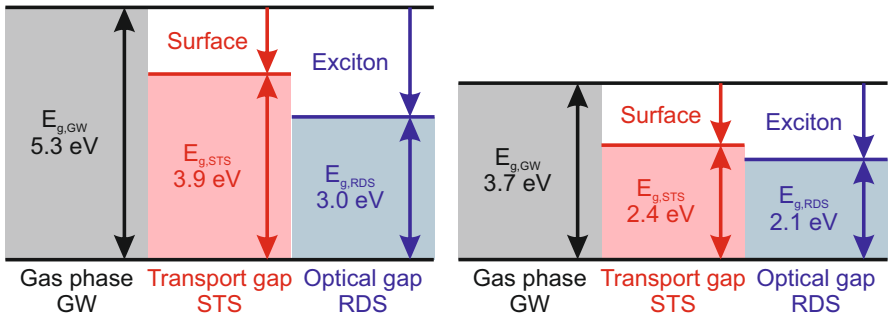

(a) PA polymer **(b)** 7-AGNR

Figure 4.2 Schematics of the relations between transport and optical gaps determined by STS and RDS in comparison with GW-calculations in vacuum for the PA polymer (a) and for the 7-AGNR (b). GW and RDS values from [113]

the finite modulation amplitude of the lock-in amplifier used to directly measure the derivative $\frac{dI_t}{dV_B}$. The lock-in amplifier settings resulted in a peak-peak modulation of ≈ 56 meV. The experimental spectra show a larger broadening which excludes the experimental parameters as the main source of broadening. Coupling between the adsorbed structures and the metal substrate introduces a life-time broadening, which can be modeled by a convolution with a Lorentzian function of appropriate width. This broadening can be of the order of 100 meV for GNRs [112]. The onset of the underlying van-Hove singularity with a Lorentzian function broadening lies at around 80% of the peak height.

As the 80% peak height position promises the most accurate extraction of the band onsets, it was used in the determination of the band gaps in Fig. 4.1. Other recipes for the fitting have been used in the literature. It is common to either use the peak position [110] or the position at the half maxima [109] without justification.

Many-body perturbation theory with a GW approximation for a free standing PA polymer and a 7-AGNR predict band gaps of 5.3 eV and 3.7 eV, respectively [113]. These values are larger than the less accurate values calculated with DFT and LDA approximation, which do not account for electron-electron and electron-hole interactions. The experimentally measured values were obtained on a Au(111) surface, which causes substrate polarizations and effectively lowers the measured band gaps (see Section 1.3). In weakly coupled systems like PA polymers and 7-AGNRs on Au(111), an image charge correction has been proven to predict transport and optical band gaps well [114, 115]. This image charge correction reduced the band gaps of the PA polymer and the 7-AGNR to 3.9-4.3 eV and 2.3-2.7 eV, respectively.

Optical band gaps of the PA polymer and the 7-AGNR have been measured with reflectance difference spectroscopy [113]. The optical band gap is the electronic band gap minus the exciton binding energy. The PA polymer reveals an optical band gap of 3.0 eV, while the 7-AGNR reveals 2.1 eV. A schematic of the relations between transport and optical gaps is shown in Fig. 4.2.

4.1.2 Length dependence of electronic levels

GNRs are essentially one-dimensional structures, due to the narrow confinement perpendicular to their long axis, which causes the electronic properties to change dramatically with even the slightest change in width (see Section 1.6). So far 7-AGNRs have always been treated as infinitely long one-dimensional structures. However, with average lengths of only 15 nm (see Section 3.1) the validity of this assumption needs to be verified, especially in the light of previous angle-resolved photoemission spectroscopy experiments which averaged over a large number of GNRs.

A DBBA monomer, which gets passivated with hydrogen before participating in polymerization, will become a $2a$ (0.86 nm) long 7-AGNR. But this GNR can just as well be seen as a 0.74 nm long GNR with zigzag edges, for which the electronic structure is expected to be dominated by the localized states related to the zigzag edges. In this case it is obvious that one has to treat it as a molecule. Elongating the 7-AGNR will eventually result in a 7-AGNR in which the confinement in the long direction becomes insignificant to its then bulk properties. On the other hand, elongation of the 7-AGNRs will reduce the sensitivity to quantum confinement along the ribbons axis and to localized states at the termini until the properties of infinite 7-AGNRs are reached asymptotically.

In order to find out the critical length at which the band gap of infinitely long 7-AGNRs is achieved, the onsets of the two electronic states that are easily visible in STS spectra and closest to E_F have been systematically measured on 7-AGNRs of various lengths. In order to exclude effects from the zigzag edges, the spectra were recorded middle of the ribbons as indicated in Fig. 4.3(a). These two states correspond to the HOMO and LUMO+1 (second lowest unoccupied molecular orbital). The LUMO level, which would be of more interest, is not accessible in the recorded spectra and the reason for this will be discussed in the following Section 4.1.4. The energies were read at 80% peak height position, as discussed in the previous section. Adding or removing a single atom in a molecule can completely change the properties of the entire molecule. With the additional hydrogen atom in the H_2 termination of a 7-AGNR, the hybridization of the central carbon atom changes to sp^3. As a result,

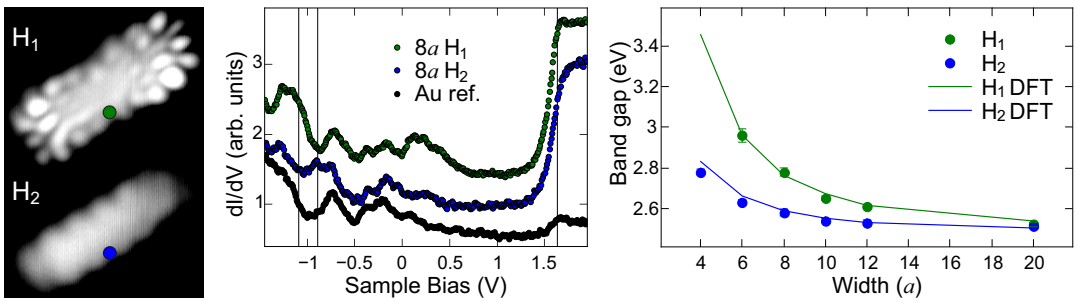

(a) {3.2×4.7 nm} **(b)** Spectra **(c)** Energy spacings

Figure 4.3 HOMO-LUMO+1 spacings in short 7-AGNRs. (a) STM image of $6a$ long 7-AGNRs with H_1 and H_2 termini. The dots mark the positions where the spectra were taken. (b) Comparison of differential conductance spectra on 7-AGNRs with different termini. (c) Experimentally measured HOMO-LUMO+1 spacings as function of length and termination. The DFT band gaps (solid lines) are increased by 0.9 eV to aid comparison with experimental results.

it cannot contribute to the delocalized π-electron system. For this reason, the band onsets have been investigated with respect to H_1 and H_2 termination of the central carbon atom at the 7-AGNR termini.

One remark to this approach needs to be made. In the part of Section 3.1 about the structure of the termini, the Tamm states that arise from the H_1 termini were presented. These states lie inside the bulk band gap of the 7-AGNRs. When regarding short ribbons as being molecules, these states are the actual HOMO and LUMO. But, in order to avoid confusion by using different names for the same states in H_1 and H_2 terminated 7-AGNRs, the Tamm states will be considered nonexistent until the end of this section.

Figure 4.3(c) shows the energy spacing between the HOMO and LUMO+1 for 7-AGNRs with H_1 and H_2 termini. 7-AGNRs of length $20a$ exhibit the same energy spacing as the ones that are much longer. In ribbons shorter than this $20a$, the spacing increases as a result of the additional confinement. The effect of the termini on the spacing in short 7-AGNRs is striking. The two curves seem to have an offset in length of about $4a$. This suggests, that the H_1 zigzag edge blocks the electronic bulk states from existing within $2a$ of a terminus, therefore effectively increasing confinement. This interpretation is supported by the fact, that the measured states could not be found in $4a$ long 7-AGNRs with H_1 termini.

When looking at short GNRs, with orthogonal edges, two are armchair while

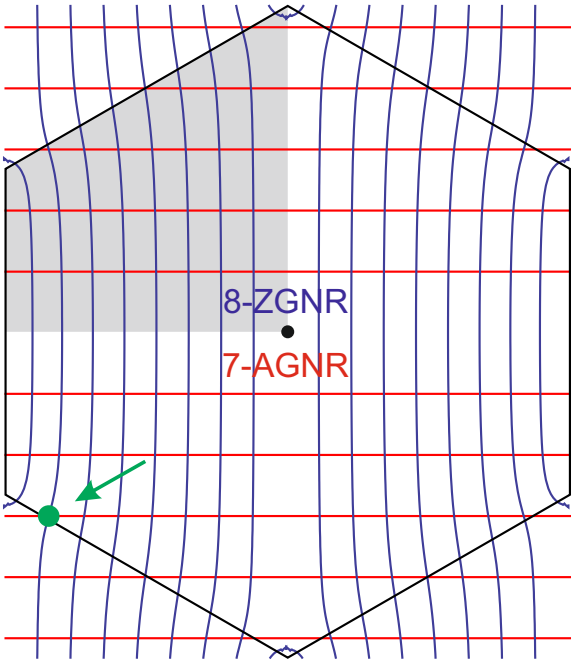

Figure 4.4 Band structure cuts of 7-AGNRs (red) and 8-ZGNRs (blue). The green dot indicates one of the four intersection that are closest to a K-point. The grey area indicates an area of unique intersections.

the other two are zigzag. In the case where confinement occurs in both in-plane dimensions, these GNRs carry the properties of both GNR types. In Section 1.6, tight binding solutions for the band structures of both GNR types have been presented. For armchair GNRs, the band structure from Equation 1.8 are evenly spaced, straight slices in k_x-direction from graphene's two-dimensional band structure. Zigzag GNRs are described by Equations 1.9 and 1.10, slicing the band structure of graphene on curved lines in k_y-direction. Hence, in short GNRs both slicings have to be considered, which quantizes the band structure to the intersections of the cuts. Figure 4.4 displays the cuts of a $N = 7$ armchair GNR and a $N = 8$ zigzag GNR ($\Rightarrow 4a$ long 7-AGNR) within the first Brillouin zone of graphene and indicating the intersection closest to a K-point. A $4a$ long 7-AGNR consists of 56 carbon atoms and thus has 56 p_z electrons. In its Brillouin zone are $7 \cdot 8/2 = 28$ unique intersections which correspond to the allowed, doubly occupied electronic states[1]. The intersections will always be further away from the K-points, than the closest point of all armchair GNR slices.

[1] Actually, only 27 unique crossing points are displayed in in the grey area in Fig. 4.4. The missing intersection is due to the imaginary part of one zigzag GNR cut. An imaginary line originating from the K-point, along k_y and away from graphene's Brillouin zone border would intersect the missed out red line, indicating the localized edge state

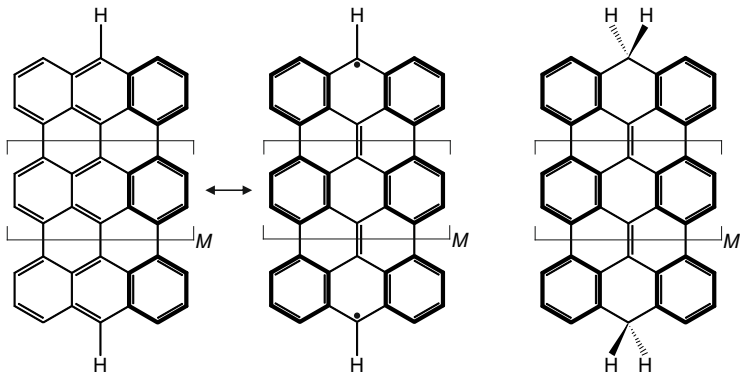

(a) H_1: Kekulé and Clar **(b)** H_2: Clar

Figure 4.5 Clar formulas of H_1 and H_2 terminated 7-AGNRs. (a) High energy Kekulé structure and low energy Clar structure of 7-AGNRs with H_1 termini. (b) Clar formula of 7-AGNR with H_2 termini.

This is due to the fact that the slices of the zigzag GNRs do not have a straight line cut through $k_x = 0$ (when the center of the Brillouin zone is $(k_x, k_y) = (0, 0)$), as illustrated in Fig. 4.4. Because of the double cone band structure, the K-points are where the band gap minimum lies, consequently the band gap increases when the armchair GNR band structure is quantized. Also, this reasoning is mostly true in the case where all four edges are of the same type with $60°/120°$ angles between them. The slices in the two-dimensional band structure of graphene are then in the same angle of $60°/120°$ between each other. This way, however, it is possible that an intersection is exactly at the closest point to the K-point of all armchair GNR slices and the band gab stays unchanged. Most obviously this is the case when both cuts go though the K-point itself in the semimetallic armchair GNRs.

The difference in the energy spacing of H_1 and H_2 terminated 7-AGNRs can be rationalized by considering Clars theory [116]. This theory of the aromatic sextet has proven to be an intuitive yet adequate model for the edge-induced distribution of π-electrons [117]. A H_1 terminated 7-AGNR has two resonance structures. In the structure model according to Kekulé, the carbon sextets on one armchair edge are assigned three double bonds, while the other two sextets of each anthryl unit have two double bonds and the sextets connecting the anthryl units have zero double bonds assigned. In addition to the Kekulé structure, the Clar structure maximizes the number of carbon sextets with three double bonds and it is more stable than alternative bond configurations [118]. Both structures are illustrated in Fig. 4.5(a). As illustrated, the Clar structure has a biradical form, which means, the even-electron chemical compound has two free radical centers which act independently of each other.

The biradical form of the H_1 terminated 7-AGNRs has lower energy spacing compared to that of the Kekulé form due to the aromatic stabilization with an extra Clar sextet for each repeating unit [119]. The contribution of the Kekulé form thus increases the energy spacing compared to that of the H_2 terminated 7-AGNRs, which have dominant contribution from the optimal Clar formula (Fig. 4.5(b)). Additionally, the weight of the biradical form has been calculated for H_1 terminated 7-AGNRs with various lengths [120]. It is increasing with increasing length and hence decreasing the weight of the energetically less favorable Kekulé form. This is in agreement with the experimental results, which reveal the convergence of the energy spacings of the H_1 and H_2 terminated 7-AGNRs upon longitudinal extension.

Calculated values of the band gap with DFT are shown in the same panel as the the experimental values. Because DFT underestimates band gaps, the curves have been offset by 0.9 eV for easier comparison. A direct comparison of the experimental results to the respective calculations show very good agreement. Notably, the calculated energy spacings show the same $4a$ length offset as the the experimental values.

One important conclusion from these results is when the bulk properties of 7-AGNRs is wanted to be probed, they should be at least $20a$ long, as for this value, the HOMO-LUMO+1 separation approaches the one of long 7-AGNRs to within 0.02 eV, independent of their termination. Shorter 7-AGNRs on the other hand have and increased band gap, which sensitively depends on the structure of the terminus.

4.1.3 Band dispersion with Fourier-transform STS

When an electron collides with a potential barrier of infinite energy height, it is scattered elastically (energy is conserved). The incident and reflected particle waves interfere with each other because of their coherence. This results in a standing wave in the existence probability with half the original wavelength of the particles wavefunction (Fig. 4.6(a)). If there is a potential barrier with finite width and finite energy height higher than the particles energy, the probability of the particle being transmitted through the barrier does not reach zero (Fig. 4.6(b)). This tunneling effect is described in detail in Section 1.2. When a particle is confined one-dimensionally in an infinite potential well of width L, the motion of the particle is restricted. Only the wavefunctions with wavelength $\pi = \frac{2L}{n}$ and energy level $E = \frac{\hbar^2 k^2}{2m_e}$ are allowed, where integer n is the wavefunction index, $k = \frac{2\pi}{\lambda}$ is the wave number, m_e is the effective mass, and $\hbar$ is Planck constant divided by 2π (Fig. 4.6(c)). If the barrier height is finite, these wavefunctions penetrate the barriers surrounding the well (Fig. 4.6(d)).

For most electronic and optical characterization methods, it is impossible to inves-

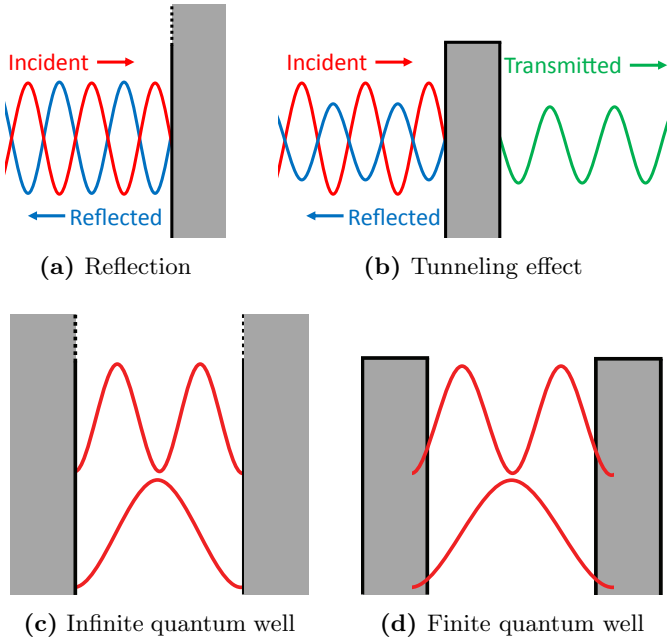

(a) Reflection **(b)** Tunneling effect

(c) Infinite quantum well **(d)** Finite quantum well

Figure 4.6 Fundamental quantum mechanical phenomena

tigate wavefunctions with nanometer-scale resolution. Only statistical averages over large areas can be obtained. STS, on the other hand, allows to observe the spatial distribution of the LDOS, value corresponding to the squared electron wavefunction at each energy level of selected individual GNRs. However, it is impossible to observe the wavefunction itself. But still, the measured standing wave patterns makes it possible to deduce information about the wave functions. Recording standing wave patterns for different energies allows to access the dispersion of occupied and unoccupied electronic bands of the system. Systems that have been studied this way include defects in graphene [121], defects in carbon nanotubes [122], ends of carbon nanotubes [123] and also defects in high-T_c superconductors [124].

This technique is now used to measure the electronic band dispersion of both 7-AGNRs and 9-AGNRs. In these cases, the standing waves arise from the scattering at the geometrically well defined short edges, similar to work by Wang et al. on polyphenylenes [125, 126]. The physical quantity measured in the experiments is the derivative $\frac{dI_t}{dV_B}$ of the tunneling current I_t with respect to the sample bias V_B. In the Tersoff-Hamann approximation [127], $\frac{dI_t}{dV_B}(V_B, x)$ at sample bias V_B and position x is proportional to the LDOS at energy $E = E_F + |e|V$. After acquiring $\frac{dI_t}{dV_B}(V_B, x)$ line scans along the GNR edges, the band dispersions can be extracted from the Fourier-transform of the spatially resolved STS spectra (FT-STS) along the ribbons axes.

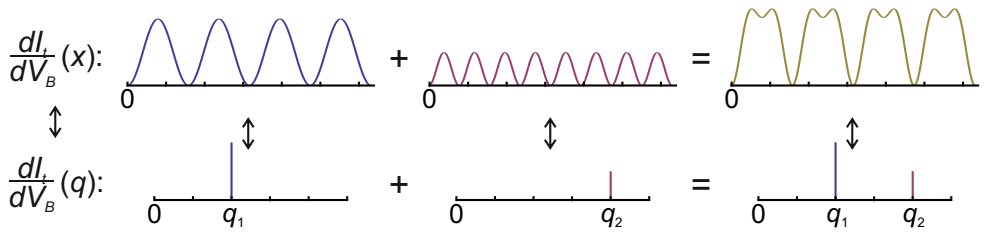

Figure 4.7 The Fourier-transform illustrated. A signal which is a superposition of two sinusoidal waves, reveals the two wave numbers q_1 and q_2 of the initial waves after a Fourier-transform.

This line-by-line discrete Fourier-transform is defined by

$$\frac{dI_t}{dV_B}(V_B, q = \frac{2\pi n}{N\delta x}) = \sum_{j=0}^{N-1} \frac{dI_t}{dV_B}(V_B, j\delta x) \exp\left(i2\pi n \frac{j}{N}\right). \tag{4.1}$$

An illustration of the conversion concept is shown in Fig. 4.7, where the Fourier-transform of two superimposed sinusoidal waves result in two values at discrete q-points. The electronic wave vector k is obtained as $\frac{q}{2} = k$ because the measured LDOS is proportional to the square of the wavefunction, effectively doubling the frequency of the standing wave. This gives direct access to the k-vectors of the electronic states probed at energy E.

Because the experiments were performed on finite AGNRs, only ribbons of lengths that exhibit the band gap of infinite AGNRs were used ($\geq 20a$). In this range, armchair GNRs are expected to not exhibit alterations in the band structure due to the extra confinement in the long direction as described in the previous section.

As described in Chapter 1, the low-energy electronic structure of graphene is characterized by delocalized π-electronic states, half of which lie below and half of which lie above E_F (Fig. 1.9(c)). The electrons in these states scatter elastically at the well-defined boundaries of GNRs, giving rise to selection rules and standing wave patterns [128]. In a single-orbital nearest-neighbor tight-binding model of AGNRs, the scattering at opposing armchair edges restricts the wave vector k_y to discrete values $k_y = \pm\frac{2\pi}{a\sqrt{3}}\frac{r}{8}$, $r \in \{1 \dots N\}$, as indicated by the blue lines in Fig. 4.8(a) [59]. Figure 4.8(b) illustrates an elastic scattering process at the short edge of a 7-AGNR: a left-moving initial Bloch state of crystal wave-vector k_i is mapped into a right-moving final state with wave vector k_f, where $|k_i| = |k_f| =: k$ due to symmetry. The superposition of these two states gives rise to a standing wave in the LDOS with non-vanishing Fourier components at the scattering vectors $\pm q$, where $q = |k_f - k_i| = 2k$. It should be noted here that scattering also occurs at the long edges of the 7-AGNR, as illustrated in Fig. 4.8(a). The resulting k_y components of the scattering wave vector

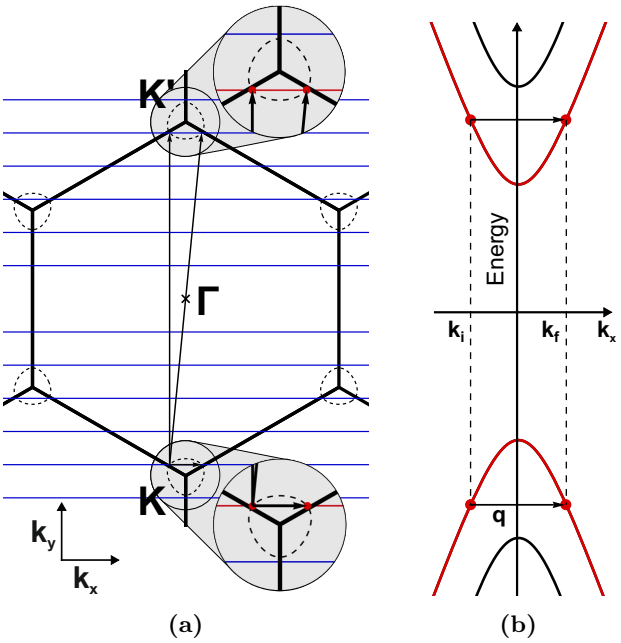

Figure 4.8 Scattering processes in AGNRs. (a) Reciprocal lattice of graphene with discretized k_y spectrum of the 7-AGNR. Constant-energy contour (red) and possible scattering processes in 2d momentum space. (b) Scattering processes from (a) projected onto k_x.

are, however, too large in order to be resolved in real-space using a standard STS experimental setup.

In this work, standing wave patterns along the armchair GNRs were determined by taking $\frac{dI_t}{dV_B}$ spectra at equidistant points on a topography line-scan along the long edge. The Fourier-transform of the STS maps were performed line-by-line for every sample bias according to Equation 4.1. Supporting DFT calculations of finite AGNRs in vacuum were performed using the PBE generalized gradient approximation to the exchange-correlation functional [129]. The CP2K code [130] was used, which expands the wave functions on an atom-centered Gaussian-type basis set. STS simulations were performed on a plane parallel to the planar GNR and in the Tersoff-Hamann approximation [127].

Band dispersion of $N = 7$ armchair graphene nanoribbons

With FT-STS it possible to obtain the band structure of a single, well-defined 7-AGNR. The experiments presented here were done in-situ. Because the $\frac{dI_t}{dV_B}$-intensity is highest at the edge of a 7-AGNR, the measured spectra were taken in a single line-

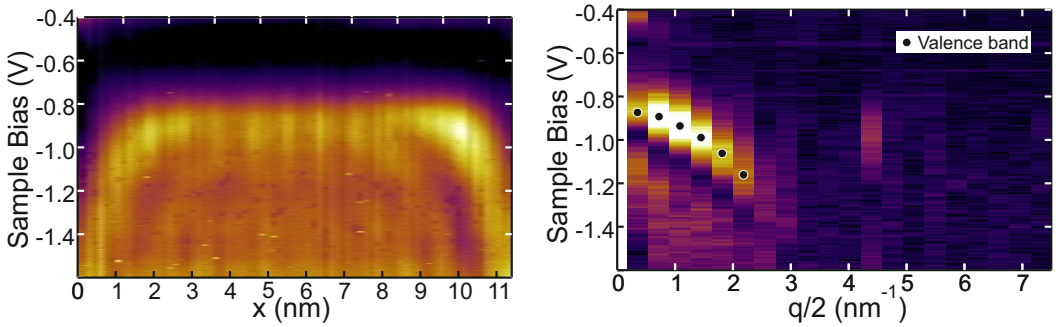

(a) STS occupied states **(b)** FT-STS occupied states

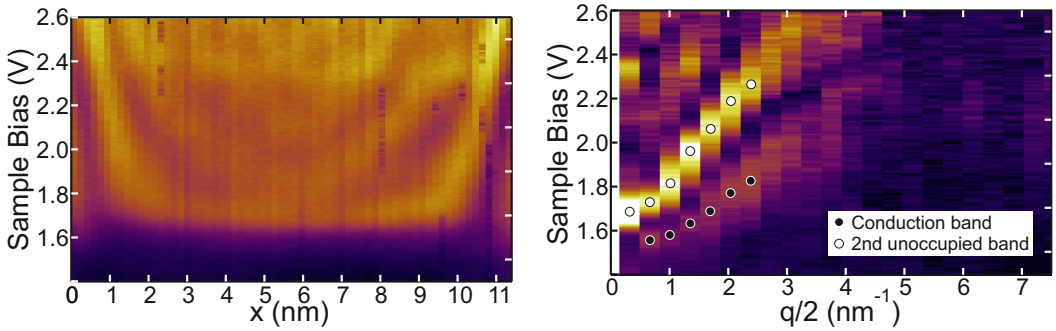

(c) STS unoccupied states **(d)** FT-STS unoccupied states

Figure 4.9 Standing waves and FT-STS on 7-AGNRs. (a) Equidistant $\frac{dI_t}{dV_B}(E,x)$ spectra of the occupied states recorded along the edge of a 7-AGNR of length $24a$. (b) Line-by-line Fourier-transform of (a) in the range $0 \leq \frac{q}{2} \leq \frac{\pi}{a}$. (c) Analogous $\frac{dI_t}{dV_B}(E,x)$ spectra of the unoccupied states, recorded along the edge of a 7-AGNR of length $24a$. (d) Line-by-line Fourier-transform of (c).

scan along one edge. The cause of this edge intensity will be discussed in Section 4.1.4 in this chapter. It was not possible to record the occupied states and the unoccupied states on the same ribbon, because a tip that provided good results for the negative LDOS maps often became attractive to small molecules and atoms on the surface when measuring the positive LDOS maps. Due to the resolution of STM, it is possible to compare results obtained from different 7-AGNRs with the exact same chemical structure.

Figure 4.9 shows the STS maps and their Fourier-transform measured on two $24a$ long defect-free ribbons. The valence band (VB), the conduction band (CB) and the second unoccupied band (CB+1) are revealed in the FT-STS images. A parabolic fit in the range $0 \leq \frac{q}{2} \leq 2$ nm^{-1} to the VB in Fig. 4.9(b) yields an effective mass of $m^*_{VB} = 0.42 \pm 0.08\ m_e$ and a band onset at $E_{VB}(k = 0) = -0.86 \pm 0.02$ eV

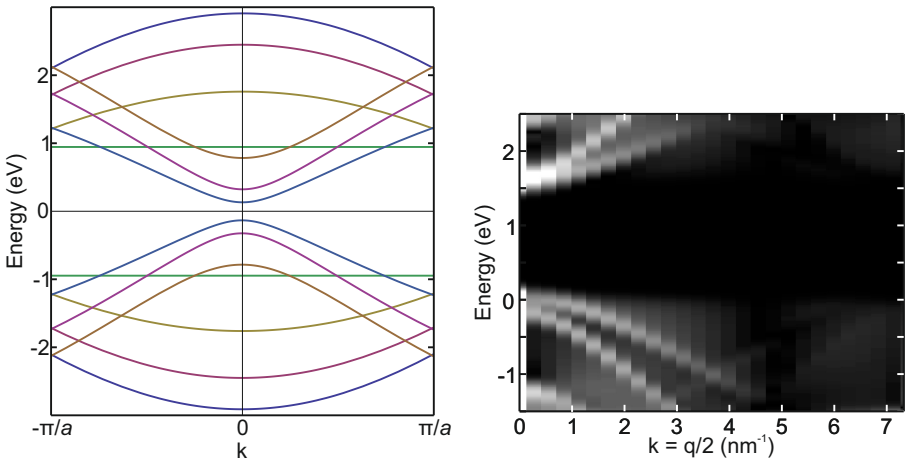

(a) Tight binding **(b)** DFT

Figure 4.10 Calculated band structure of 7-AGNRs. (a) Tight binding band structure of 7-AGNRs from Equation 1.8 with $\gamma_0 = 1$ in the range $-\frac{\pi}{a} \leq k \leq \frac{\pi}{a}$. (b) FT-STS simulation on a $24a$ long 7-AGNR in the range $0 \leq k \leq \frac{\pi}{a}$ evaluated 0.1 nm above the GNR, $E_{VB}(k = 0)$ is set to zero. The white lines are the DFT calculated bands of infinite 7-AGNRs

with respect to E_F. It has to be noted that the Fourier-transform is sensitive to the exact width of the real-space window. The associated uncertainty in the band mass and band onset has been incorporated into the errors. The lack of intensity for $k > 4$ nm^{-1} in the experimental FT-STS indicates a resolution limit due to finite tip-sample separation and finite tip size, it does not imply the absence of scattering with wave vectors $k > 4$ nm^{-1}.

Corresponding results for the two lowest unoccupied band have been extracted from Fig. 4.9(b). The CB sets in at $E_{CB}(k = 0) = 1.52 \pm 0.02$ eV and the CB+1 sets in at $E_{CB+1}(k = 0) = 1.67 \pm 0.01$ eV with band masses of $m^*_{CB} = 0.40 \pm 0.18\ m_e$ and $m^*_{CB+1} = 0.21 \pm 0.02\ m_e$, respectively. The parabolic fits were done in the range $0 \leq \frac{q}{2} \leq 2$ nm^{-1} for the CB and in the range of $0 \leq \frac{q}{2} \leq 1.5$ nm^{-1} for the CB+1. Interestingly, the CB appears much fainter compared to the CB+1 and its signal further looses intensity towards $q = 0$. These observations can be related to the decay of the associated wave functions as a function of tip-sample distance (see Section 4.1.4).

Comparison with theoretical predictions

Equation 1.8, which resulted from a tight binding calculation, extracts the electronic band structure of armchair GNRs as evenly spaced slices from free standing graphene's

band structure. The one for 7-AGNRs is shown in Fig. 4.10(a) with a hopping parameter $\gamma_0 = 1$. Due to the symmetry of the π-band in graphene, the bands of 7-AGNRs exhibit the same occupied-unoccupied band symmetry. The three bands closest to E_F have their minimum at $k = 0$ with the second band showing a stronger curvature, indicating a smaller m^*, like it has experimentally been observed. The position of the band extrema at $k = 0$ fits well to the experimental results. However, only the VB, CB and CB+1 are observed, but the VB-1 is not accounted for in the FT-STS maps. In the tight binding calculations, no influence of the substrate was taken into account and γ_0 has not been optimized. This only makes it possible to compare the results qualitatively without information on absolute values.

It is possible to simulate FT-STS using DFT by calculating the charge densities of a GNR for several energies and applying a Fourier-transform parallel to the GNR axis. Figure 4.10(b)shows the result of such a simulation on a 7-AGNR of length $24a$. In the examined energy range, three electronic bands can be identified on either side of E_F and is qualitatively similar to the tight binding band structure. Yet, DFT is able to predict band curvatures rather precisely: $m^*_{VB} = 0.33\ m_e$, $m^*_{CB} = 0.41\ m_e$ and $m^*_{CB+1} = 0.14\ m_e$. Considering the error margin, the values for the VB and CB match with the ones extracted from FT-STS. The difference for the CB+1 is a bit larger than the experimental error margin, but in all, the experimental and DFT results are in good agreement. Especially in the light of previous measurement of m^* [78, 109, 111] FT-STS proves to be a robust way of determining the energy dispersion of frontier electronic bands.

Length dependence

In the beginning of this chapter the transition from molecular to bulk 7-AGNRs was investigated with the result that armchair GNRs should be at least $20a$ long when their bulk properties are intended to be probed. Additionally, the band structure is expected to be independent of the termination, in contrast to shorter GNRs where they have significant influence (Fig. 4.3). In order to verify this assumption, the experiments shown in Fig. 4.9 have been repeated. A selection of FT-STS maps are shown in Fig. 4.11 including their parabolic fits in the range of $0 \leq \frac{q}{2} \leq 2\ \mathrm{nm}^{-1}$ for the VBs and CBs, and in the range of $0 \leq \frac{q}{2} \leq 1.5\ \mathrm{nm}^{-1}$ for the CB+1s. As it can be seen from the consistency of the obtained $E(k = 0)$ and m^* in the subcaptions, no systematic effects of the length of the GNRs, their termini or the tip shape can be observed. The values for $E(k = 0)$ and m^* averaged over all obtained values, including the respective error margins and DFT results, are stated in Tab. 4.1. On the basis of

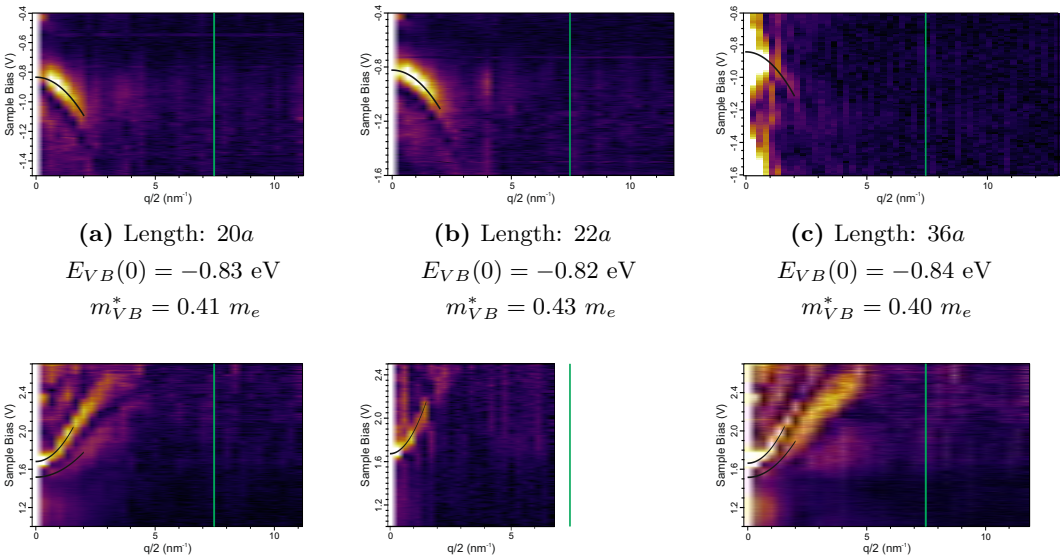

(a) Length: $20a$
$E_{VB}(0) = -0.83$ eV
$m^*_{VB} = 0.41\ m_e$

(b) Length: $22a$
$E_{VB}(0) = -0.82$ eV
$m^*_{VB} = 0.43\ m_e$

(c) Length: $36a$
$E_{VB}(0) = -0.84$ eV
$m^*_{VB} = 0.40\ m_e$

(d) Length: $22a$
$E_{CB}(0) = 1.52$ eV
$m^*_{CB} = 0.41\ m_e$
$E_{CB+1}(0) = 1.66$ eV
$m^*_{CB+1} = 0.21\ m_e$

(e) Length: $22a$
$E_{CB+1}(0) = 1.67$ eV
$m^*_{CB+1} = 0.21\ m_e$

(f) Length: $26a$
$E_{CB}(0) = 1.51$ eV
$m^*_{CB} = 0.40\ m_e$
$E_{CB+1}(0) = 1.67$ eV
$m^*_{CB+1} = 0.21\ m_e$

Figure 4.11 FT-STS on 7-AGNRs of varied length. The full range of $\frac{dI_t}{dV_B}(V_B, q/2)$, corresponding to $0 \leq q \leq \frac{\pi}{\delta x}$ is displayed. The green lines indicate the border of the first Brillouin zone at $q/2 = \frac{\pi}{a} \approx 7.3\ \mathrm{nm}^{-1}$.

these values, the band gap of 7-AGNRs on a Au substrate is $E_g = 2.37 \pm 0.06$ eV.

	VB	CB	CB+1
$E(k = 0)$ [eV]	-0.84 ± 0.05	1.53 ± 0.04	1.67 ± 0.03
m^* $[m_e]$	0.42 ± 0.08 (0.33)	0.40 ± 0.18 (0.41)	0.20 ± 0.03 (0.14)

Table 4.1 Band onsets and effective masses for the different bands averaged over all measurements shown in Fig. 4.9 and 4.11. DFT results in brackets.

Comparing the results from Tab. 4.1 with the values for the effective masses reported previously is tricky. The three results mentioned in the beginning of this section are spread across a huge range: $m^*_{VB} = 0.21\ m_e$ [109], $1.07\ m_e$ [78] and $1.37\ m_e$ [111]. The result obtained with FT-STS, $m^*_{VB} = 0.42\ m_e$, is in the lower part of this range. Yet, the measurements presented here were done in-situ, on selected defect-free GNRs, not averaged over several, and have been reproduced several times. For non of the other values these points are valid which gives $m^*_{VB} = 0.42\ m_e$ a high relevance.

As for the band gap, $E_g = 2.37 \pm 0.06$ eV agrees with the previous results (2.3 eV [109] and 2.5 eV [110]) which were extracted from single $\frac{dI_t}{dV_B}(V_B)$ spectra. In contrast, the onset of the electronic bands in FT-STS were obtained by parabolic fits. The CB is strongly reduced close to $q = 0$ (Fig. 4.9(b)). In FT-STS the $q = 0$ component correlates with the average of all initial $\frac{dI_t}{dV_B}(x)$. Therefore, the CB onset should (if at all) only appear as a very small signal compared to the high intensity CB+1. Taking a look at the spectra in [109] and [110] shows that in both cases a large intensity was believed to be the CB. However, this intensity can clearly be assigned to the CB+1 with FT-STS. A detailed discussion why the CB of 7-AGNRs is missed in standard STS will be given below in Section 4.1.4.

Spectra selection

Fourier-transform is sensitive to the exact width of the real-space window. Removing or adding spectra to the STS images changes the appearance of the resultant FT-STS images. The STS and FT-STS images in Fig 4.12(b) are the same shown in Fig 4.9(c) and (d). The other images show the equivalent images with one spectrum more (a) or less (c) on each side. The influence of the extracted m^* is considerable which makes the selection of the real-space window crucial. The main factor is an as little as possible variation in m^* of real-space images with $M + 2$ and $M - 2$, where M is the number of spectra in a range that reveals clear bands. When increasing M, effects from the surface at the GNR edges are introduced, which splits the CB into two bands. On the other hand, when M is decreased that the intensity maxima at the termini are left out, the CB+1 splits into two.

This spectra selection effect increases the uncertainty in the experimental m^* and is in fact the biggest contribution to the error bars in Tab. 4.1. On the other hand, $E(k = 0)$ is hardly effected by the selection of the real-space window within the range that provided clear bands. The error in the onset is thus comparatively small.

4.1.4 Influence of the tip-sample distance on STS spectra

The low intensities of some of the bands raise the question, whether the tip-sample distance has an influence on the visibility of electronic states in STS. According to Equation 1.1, I_t depends exponentially on the tunneling gap, in the case of STM and STS the separation between tip and sample. Consequently, the feedback loop needs to move the tip closer to the sample when the set point I_t is increased at constant V_B. If electronic states are hidden due to an unfavorable tip-sample distance, it might also depend on the in-plane position on top of a GNR. When taking two-dimensional

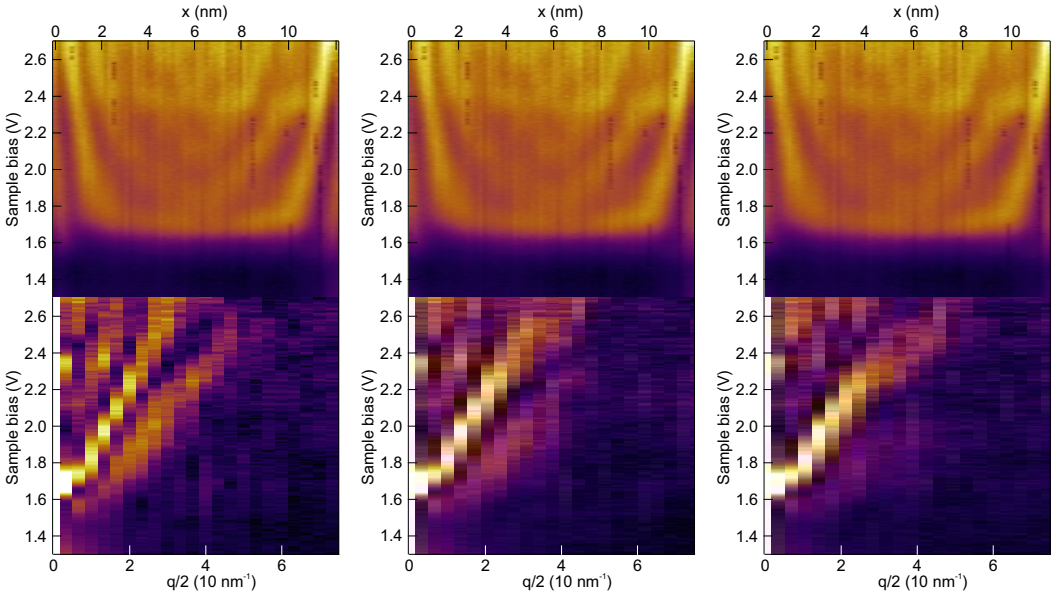

(a) $m^*_{CB} = 0.32\ m_e$
$m^*_{CB+1} = 0.21\ m_e$

(b) $m^*_{CB} = 0.40\ m_e$
$m^*_{CB+1} = 0.21\ m_e$

(c) $m^*_{CB} = 0.48\ m_e$
$m^*_{CB+1} = 0.23\ m_e$

Figure 4.12 Spectra selection for FT-STS. (b) The same images shown in Fig 4.9(c) and (d). Selecting one spectrum more (a) or less (c) on each side results in different FT-STS images. The extracted values for m^* are given in the subcaptions.

$\frac{dI_t}{dV_B}(x, y)$ maps at fixed V_B, a concentration of intensity at the edges of the GNR is always observed [77, 109]. This observation is shown in Fig 4.13(a) where the edge intensity can be found in constant-I_t and constant-z mode. Based on the calculated electronic wavefunctions [131], there is no obvious reason for this edge effect.

As stated in Section 4.1.3, the onset of the CB has been missed in previous STS experiments on 7-AGNRs [109, 110] and it was only acquired through parabolic fits in FT-STS maps (Fig. 4.9). Previously set points of ($V_B = 2.5$ V, $I_t = 0.2$ nA) [109] and ($V_B = 1.2$ V, $I_t = 0.015$ nA) [110] where used. These experiments were repeated using higher I_t to reduce the tip sample difference. Figure 4.13(b) shows two $\frac{dI_t}{dV_B}(V_B)$ spectra taken on the armchair edge with set points ($V_B = 1.8$ V, $I_t = 1.0$ nA) and ($V_B = 1.8$ V, $I_t = 3.0$ nA), the resulting height difference between them is 0.13 nm. The black spectra with lower I_t looks similar to the previous spectra, where nothing would indicate the onset of the CB. In the grey spectra, however, a small intensity peak appears at the energy position of the CB onset. Figure 4.13(c) proves that this intensity peak is not due to an electronic state from the Au substrate. In addition, it shows that the measured intensity is strongly reduced in the ribbon's center.

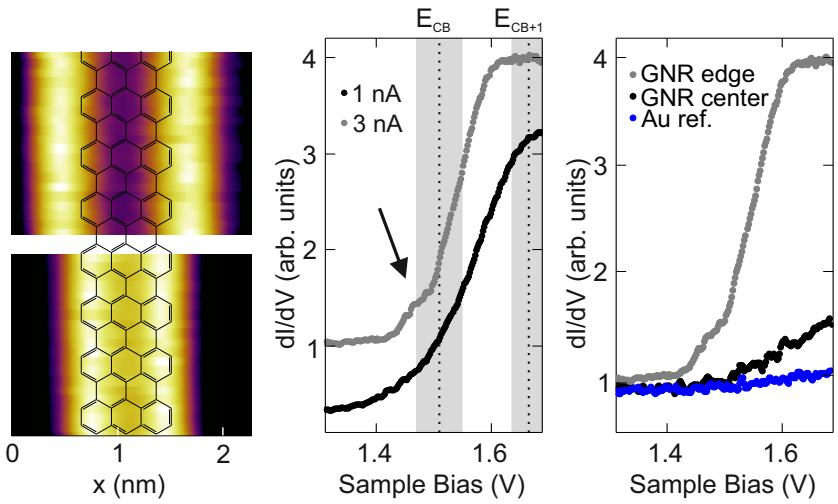

Figure 4.13 Hidden electronic states in STS spectra. (a) Constant-I_t (top) and constant-z (bottom) $\frac{dI_t}{dV_B}(x, y)$ maps of the same 7AGNR (set point $V_B = 2.5$ V, $I_t = 0.3$ nA). (b) $\frac{dI_t}{dV_B}(V_B)$ spectra at the long edge of the 7-AGNR with set point $I_t = 1.0$ nA (black) and 3.0 nA (gray) at $V_B = 1.8$ V. The tip-sample distance is reduced by 0.13 nm. The dotted lines with grey error margins indicate E_{CB} and E_{CB+1} (Tab 4.1). (c) Same grey $\frac{dI_t}{dV_B}(V_B)$ spectrum as in (b) compared to a reference spectrum on the Au substrate and a spectrum on top of the center of the GNR.

The observations in Fig. 4.13 relating to the tip-sample separation cannot simply be interpreted fully by further experiments. Here, DFT provides a solid explanation. Figure 4.14 shows the Kohn-Sham orbitals ϕ_j of a finite 7-AGNR at the respective band onsets, evaluated at short tip-sample distance of 0.1 nm (a) and a more realistic experimental distance of 0.4 nm (b). Kohn-Sham orbitals resemble the molecular orbitals and accordingly its square resembles the charge carrier density that is probed in STS [132, 133]. At a tip-sample distance of 0.1 nm, the states corresponding to the CB and the VB-1 strongly oscillate perpendicular and parallel to the ribbon axis, while the states corresponding to the VB and the CB+1 oscillate only perpendicular to the ribbon axis. Moving further away from the GNR, the orbitals smear out (Fig. 4.14(b)). In areas with a strongly oscillating state, superposition cancels out ϕ_j in these areas, which results in a faster decay of the state in z-direction. This is exactly what happens to the CB and VB-1 states. In the case of the VB and the CB+1, the states survive on the long edge of the GNR. This has a considerable effect on $\frac{dI_t}{dV_B}(V_B, x)$ spectra and explains the edge intensity in $\frac{dI_t}{dV_B}(x, y)$ maps (Fig. 4.13(a) and (c)), the missing onset

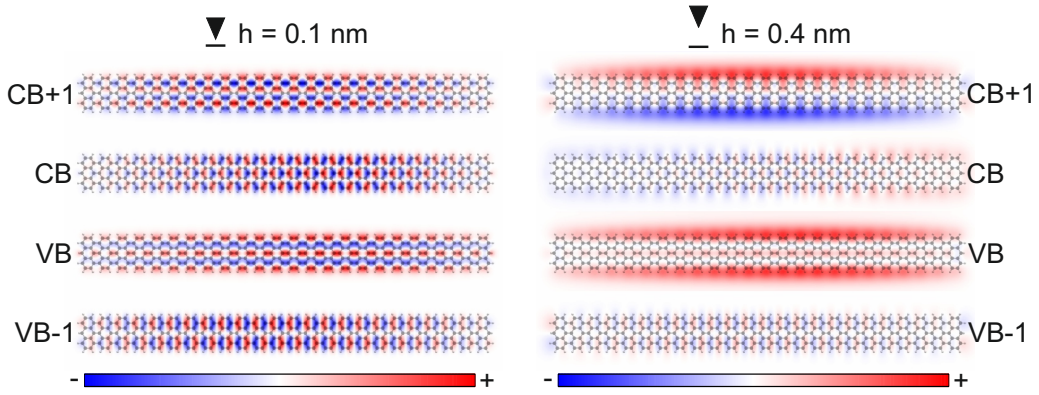

(a) Kohn-Sham orbitals 0.1 nm **(b)** Kohn-Sham orbitals 0.4 nm

Figure 4.14 Effect of tip-sample distance. Kohn-Sham orbitals at the band onsets for a 7-AGNR of length $24a$ evaluated at different heights above the GNR.

of the CB in the FT-STS maps (Fig. 4.9 and 4.11) (and the completely missing VB for that matter), and the appearance of the CB onset at small tip-sample distances Fig. 4.13(b).

In Fig. 4.10(b) a DFT simulation of the FT-STS measurements on 7-AGNRs was shown. This simulation can be used to illustrate the effect of the tip-sample distance on FT-STS measurements by evaluating the LDOS for different z. Figures 4.15(a) and (b) show LDOSs along a line parallel to the long axis of a $24a$ 7-AGNR evaluated at $z = 0.1$ nm and $z = 0.4$ nm, respectively. A line-by-line Fourier-transform of the LDOS evaluated at $z = 0.1$ nm using Equation 4.1 is shown in Fig. 4.15(c) and reveals the band structure and all electronic bands and their onsets can be clearly determined. In Fig. 4.15(d), which shows the line-by-line Fourier-transform of the LDOS evaluated at $z = 0.4$ nm, the VB-1 and VB-2 are missing completely while the intensity related to the CB is strongly reduced at low k-values. Comparing the DFT images with the images in Fig. 4.9, the experimentally resolved bands of the 7-AGNRs can convincingly be labeled the VB, CB and CB+1.

4.2 $N = 9$ armchair graphene nanoribbons

The fabrication of high quality 9-AGNRs was only achieved recently. Therefore, no experimental results of the electronic properties have yet been reported, except the ones presented here.

As a first investigation into the electronic properties of 9-AGNRs, the band gap

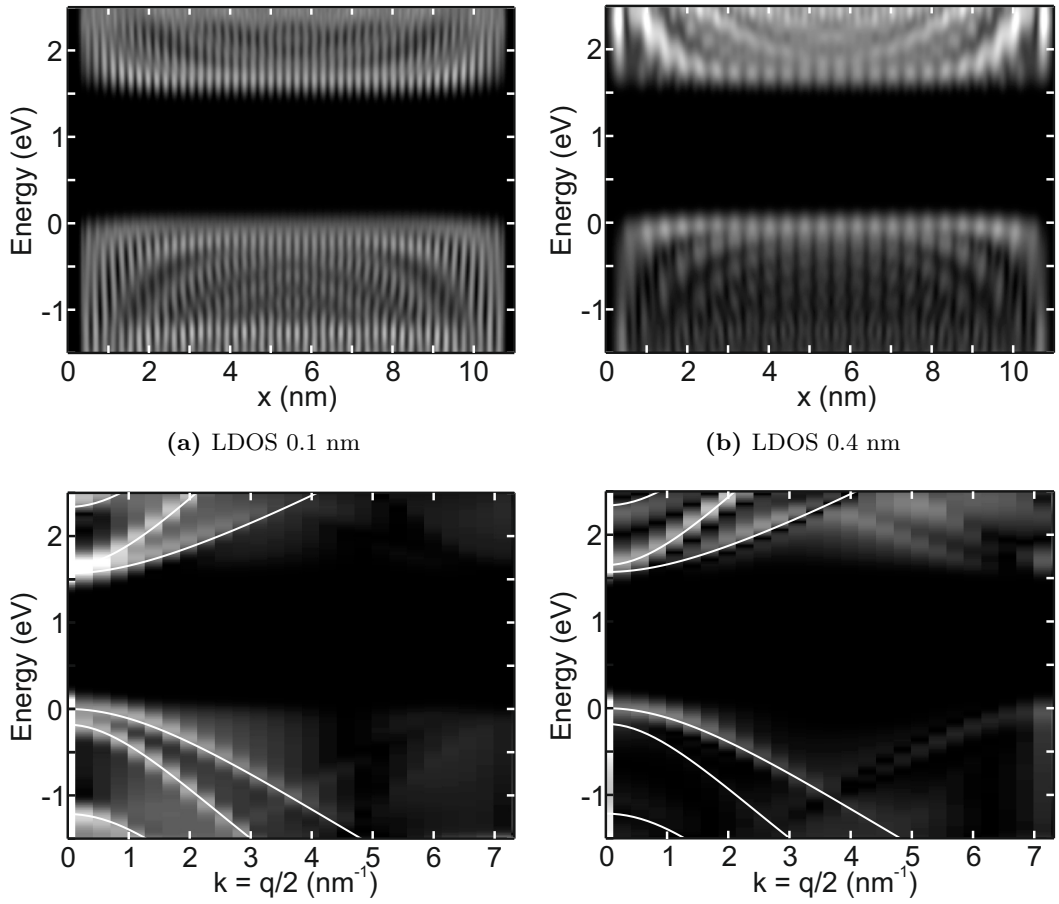

(a) LDOS 0.1 nm

(b) LDOS 0.4 nm

(c) FT-LDOS 0.1 nm

(d) FT-LDOS 0.4 nm

Figure 4.15 LDOS and FT-LDOS on 7-AGNRs. (a) LDOS along a 7-AGNR of length $24a$, integrated across the ribbon evaluated at $z = 0.1$ nm. (a) Same as a but evaluated at $z = 0.4$ nm. (c) Line-by-line Fourier-transform of (a) in the range $0 \leq k \leq \frac{\pi}{a}$. (d) Line-by-line Fourier-transform of (b). $E_V B(k = 0)$ is set to zero in all subfigures.

was measured with standard STS. Figure 4.16 shows two $\frac{dI_t}{dV_B}(V_B)$ spectra recorded on a 9-AGNR and on the Au(111) surface for reference. The onsets were determined at the position of 80% peak height for the reasons discussed in Section 4.1.1. The two onsets at $V_B = -0.3$ V and $V_B = 1.1$ V yield a band gap of 1.4 eV. In order to observe the VB onset, large $I_t = 10$ nA was needed, indicates a fast decay of the wave function away from the GNR.

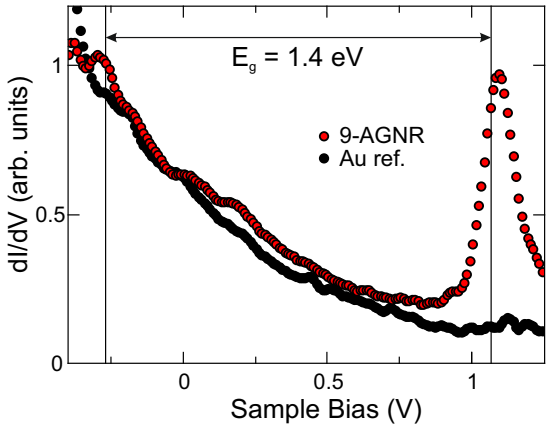

Figure 4.16 9-AGNR band gap from STS. Two $\frac{dI_t}{dV_B}(V_B)$ spectra recorded on a 9-AGNR (red) and on the Au(111) surface for reference (black). The vertical lines mark the onsets of the VB and CB. Large $I_t = 10$ nA was needed to resolve the VB onset.

4.2.1 Band dispersion with Fourier-transform STS

The experimental steps in FT-STS on 9-AGNRs are largely the same as for the 7-AGNRs. The spectra were taken in a single line-scan along one edge, as both armchair GNR types exhibit the same edge intensity effect (see the section about the tip-sample distance on page 74). In addition to the well defined termini, scattering in 9-AGNRs can occur at the likewise well defined defects.

Figure 4.17 shows characteristic STS maps and their line-by-line Fourier-transform maps. The STS maps on the occupied states were recorded on a $30a$ section between a terminus and a defect. The occupied states could only be resolved at a setpoint $I_t = 10$ nA, which is more than a factor of 10 higher than in all other STS maps. In the FT-STS image of the occupied states, the VB and the third and fourth occupied bands (VB-2 and VB-3, respectively) are revealed. A parabolic fit in the range of $0 \leq \frac{q}{2} \leq 1$ nm^{-1} to the VB in Fig 4.17(b) yields an effective mass of $m^*_{VB} = 0.12 \pm 0.03\ m_e$ with a band onset at $k = 0$ of $E = -0.28 \pm 0.01$ eV. The value for the other bands are summarized in Tab. 4.2.

Corresponding results can be extracted from the STS map in Fig 4.17(d) recorded on a $23a$ segment between two defects. The resulting FT-STS image in Fig. 4.17(d) reveals the CB, CB+1 and the 3rd and 4th unoccupied band (CB+2 and CB+3, respectively). A parabolic fit in the range of $0 \leq \frac{q}{2} \leq 1$ nm^{-1} to the CB yields an effective mass of $m^*_{VB} = 0.11 \pm 0.03\ m_e$ with a band onset at $k = 0$ of $E = 1.10 \pm 0.02$ eV. The value for the other bands are listed in Tab. 4.2. The difference of

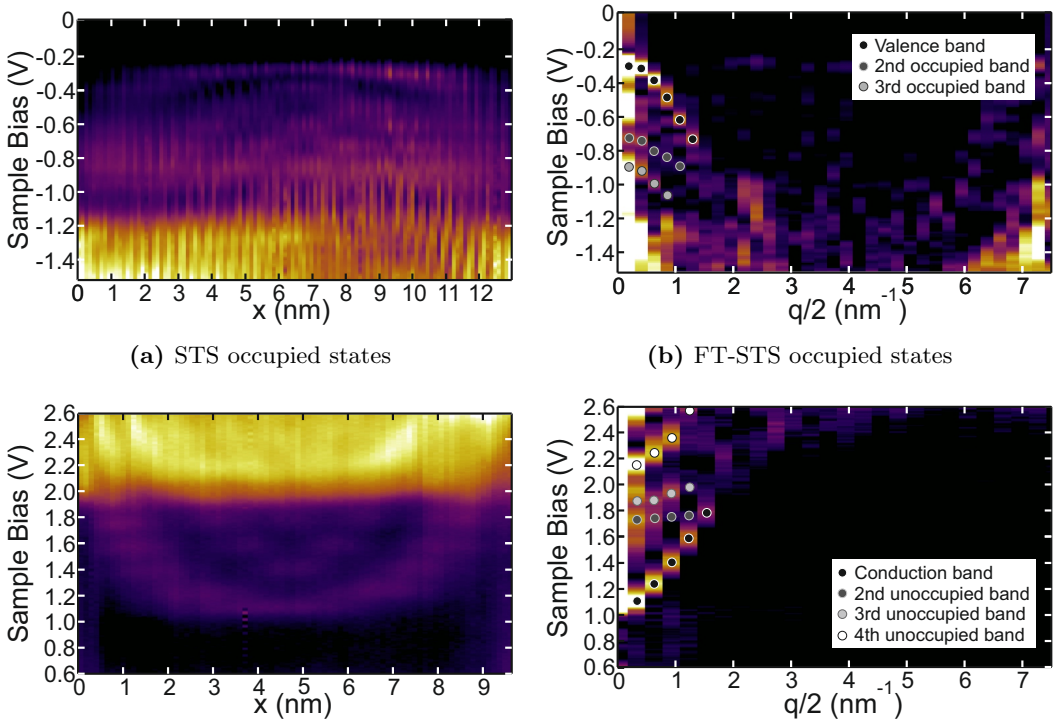

(a) STS occupied states

(b) FT-STS occupied states

(c) STS unoccupied states

(d) FT-STS unoccupied states

Figure 4.17 Standing waves and FT-STS on 9-AGNRs. (a) Equidistant $\frac{dI_t}{dV_B}(E,x)$ spectra of the occupied states recorded on a 30a long section between a terminus and a defect. (b) Line-by-line Fourier-transform of (a) in the range $0 \leq \frac{q}{2} \leq \frac{\pi}{a}$. (c) Analogous $\frac{dI_t}{dV_B}(E,x)$ spectra of the unoccupied states, recorded on a 23a segment between two defects. (d) Line-by-line Fourier-transform of (c).

the VB and CB onsets yields an electronic band gap of 1.38 ± 0.02 eV.

Comparison with theoretical predictions

Just like for 7-AGNRs, Equation 1.8 extracts the electronic band structure of armchair GNRs as evenly spaced slices from free standing graphene's band structure. The one for 9-AGNRs is shown in Fig. 4.18(a) with a hopping parameter $\gamma_0 = 1$. Due to the symmetry of the π-band in graphene, the bands of 7-AGNRs exhibit the same occupied-unoccupied band symmetry. The four bands closest to E_F have their minimum at $k = 0$. The VB shows a stronger curvature for small k, indicating a smaller m^* as experimentally observed. on the other hand the VB-1 shows a weaker curvature than the other three bands. Due to symmetry, this is true for the unoccupied bands as well. The position of the band extrema at $k = 0$ fits well to the experimental results

	VB	VB-1	VB-2	VB-3
$E(k=0)$ [eV]	-0.28 ± 0.01	-	-071 ± 0.04	-0.89 ± 0.06
m^* $[m_e]$	0.12 ± 0.03 (0.11)	- (0.72)	0.18 ± 0.10 (0.19)	0.16 ± 0.08 (0.22)
	CB	CB+1	CB+2	CB+3
$E(k=0)$ [eV]	1.10 ± 0.02	1.72 ± 0.04	1.86 ± 0.8	2.13 ± 0.03
m^* $[m_e]$	0.11 ± 0.03 (0.11)	1.69 ± 0.62 (1.48)	0.55 ± 0.24 (0.17)	0.12 ± 0.08 (0.18)

Table 4.2 Band onsets and effective masses for the different bands in Fig. 4.17. DFT results in brackets.

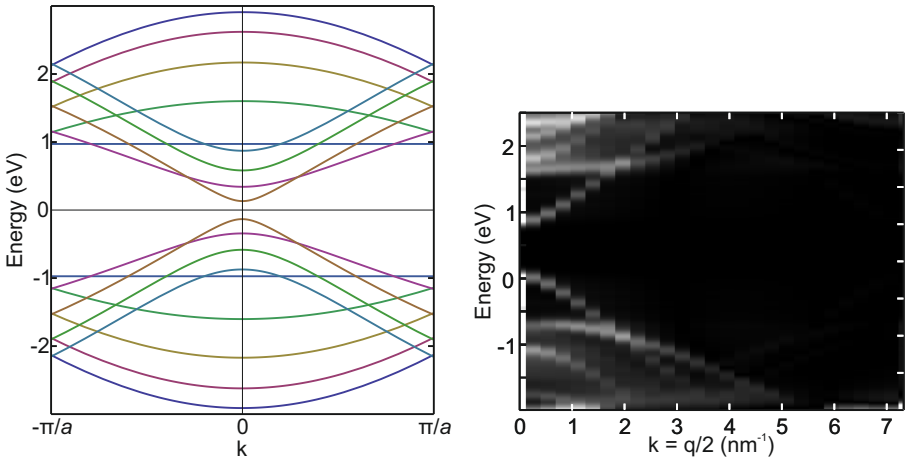

(a) Tight binding **(b)** DFT

Figure 4.18 Calculated band structure of 9-AGNRs. (a) Tight binding band structure of 7-AGNRs from Equation 1.8 with $\gamma_0 = 1$ in the range $-\frac{\pi}{a} \leq k \leq \frac{\pi}{a}$. (b) FT-STS simulation on a $24a$ long 7-AGNR in the range $0 \leq k \leq \frac{\pi}{a}$ evaluated 0.1 nm above the GNR, $E_{VB}(k=0)$ is set to zero.

as well as the curvature relation between all four unoccupied bands. In the occupied bands, however, the rather flat band, which is the VB-1, is missing and the remaining bands are the VB-2 and VB-3.

The FT-STS can again be simulated using DFT. Figure 4.18(b)shows the result of a simulation on a 7-AGNR of length $24a$. In the examined energy range, four electronic bands can be identified on either side of E_F and is qualitatively similar to the tight binding band structure. The DFT prediction on the band curvatures of the frontier bands are: $m^*_{VB} = 0.11\ m_e$ and $m^*_{CB} = 0.11\ m_e$. These are in very good

agreement to the experimental values extracted from Fig. 4.17. The data quality of the experimental data for the other bands is low, which is reflected in the large error margins. Nevertheless, the simulation and experimental data are in qualitative agreement. Further analysis into the electronic structure of 9-AGNRs is needed to back up the acquired information, preferably using a different technique like angle resolved photoemission spectroscopy.

4.3 Significance for general armchair graphene nanoribbon systems

The combination of FT-STS with DFT simulations allows for a reliable determination of the VB and CB energies and their effective masses in the vicinity of the K-points. It can circumvent the problem of quickly decaying wave functions, which hides in standard STS spectra and the reduction of the tip-sample distance by increasing I_t is not always possible.

The measured band gap of a 9-AGNR is 1.0 eV lower compared to the one of a 7-AGNR [112] and about the same as the band gap of a 13-AGNR [110]. The relation of the band gap is predicted to be inverse proportional to the width with the division into the three families, as is was illustrated in Fig. 1.13 on page 22. The 7- and 13-AGNRs belong to the high band gap $3p$+1 family while the 9-AGNR belongs to the medium band gap $3p$ family [65]. The high currents needed in order to observe the VB of 9-AGNRs and given the fact that frontier bands have been missed in standard STS experiments, the value for the band gap of 13-AGNRs has to be accepted with caution. Nevertheless, the experimental electronic band gap versus width relation is consistent with the theoretical predictions presented. The relative bending of the observed electronic bands, the dependence on the width and the quantification supports are in agreement with the illustrative picture of cutting the band structure of a GNR out of graphene's band structure.

Chapter 5

Heterojunctions

A heterojunction is generally defined as the interface that between two materials with dissimilar electronic properties. The combinations of the materials vary greatly depending on the applications. Diodes and field effect transistors, which can be used for switches or rectifiers, combine doped semiconductors. In solar cells, semiconductors are combined to form heterojunctions for charge depletion regions with the desired optical properties. Heterojunctions are characterized by the alignment of the electronic frontier bands of the individual semiconductors: In a straddling gap heterojunction (type I) one material has the VB maximum at lower and the CB minimum at higher energies than the second material with lower E_g. In a staggered gap heterojunction (type II) one material has both, the VB maximum and the CB minimum, at higher energy than the second material. A broken gap heterojunction (type III) is a type II heterojunction but the VB maximum of one material is at higher energy than the CB minimum of the other material. This means there is no overlap of E_g of the two materials.

Heterojunctions of GNRs have theoretically been studied in detail [107, 108, 134–136]. The experimental study is, however, limited by the difficulties of fabricating them. The obvious way of growing GNR heterojunctions, would be to use precursor monomers of two dissimilar GNRs and let them form a mixed polymer chain. During cyclodehydrogenation, GNR heterojunctions develop where two different type precursor monomers have undergone radical addition. This has been done using a precursor monomer that forms a seesaw type nanoribbon and the same precursor monomer where two carbon atoms are substituted by nitrogen atoms, effectively doping it [137, 138]. The interface in which the shift of the bands occur has a width of only 3 nm and an internal electric field with a maximum strength in the order of $2 \times 10^8 \ \frac{\mathrm{V}}{\mathrm{m}}$. Such a narrow region with a strong electric field in type II heterojunctions is useful for

devices with such a small feature size and in systems whose efficiency depends on high charge-carrier separation, like photovoltaic cells [139, 140].

By using a third precursor monomer as coupling component between the two GNRs of the heterojunction would increase the control over the synthesis and open doors to more elaborate heterojunctions. If the precursor monomer of the coupling component would become a narrow GNR section with smaller band gap than the GNRs it is connecting, one would obtain a semiconductor quantum dot, which is often referred to as artificial atom [141]. With artificial atoms, recombination of excitons can be confined to specific spacial positions, even in an electric field [141–143].

There are two known possibilities to fabricate GNR heterojunction by just using a single type precursor monomer. When fusing GNRs together, as it has been discussed in Chapter 3, it rarely happens that both initial GNRs have the same length and are aligned without displacement. As a result, parts of the GNR still have the original width while the rest has the final width, creating a heterojunction [104]. A second possibility was shown in [75], where the cyclodehydrogenation of a PA polymer was interrupted. As a result, parts of the 7-AGNR already had its final structure, while other parts had undergone cyclodehydrogenation on one side of the polymer only, forming a 5-AGNR with benzene rings attached to one side (5+-AGNR).

Two different heterojunctions have been fabricated using only DBBA as precursor monomer and following both procedures mentioned in the previous paragraph.

5.1 $N = 5+/7$ armchair graphene nanoribbons

Here, the electronic band structure at the interface of a $N = 7$ and $N = 5+$ armchair GNR heterojunction is investigated. The fabrication of 7-AGNRs has been discussed in detail in Section 3.1. Depending on the annealing temperature, three different and stable structures can be found on the substrate. The PA polymer, the partially cyclodehydrogenated polymer and the flat 7-AGNR have substantially dissimilar band gaps as listed in Fig. 4.1(a). Upon combining two structures, the electronic bands shift in the vicinity of the interface.

The $N = 5+/7$ armchair GNR heterojunctions used here were fabricated according to the recipe from [75]. As is was described in Section 3.1, after an initial reaction, the cyclodehydrogenation of the PA polymer continues on one side only due to the flattening in the structure, which lowers the activation barrier of the partially reacted side with respect to the benzene rings on the opposite side. This allows the realization of heterojunctions by annealing at a reduced temperature.

The STM image in Fig. 5.1(a) shows such a partially cyclodehydrogenated sec-

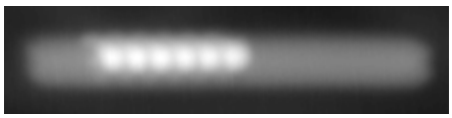

(a) Partially cyclodehydrogenated PA polymer {8.0×1.9 nm}

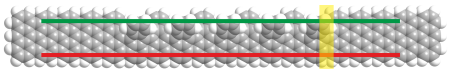

(b) Model of the double heterojunction investigated in (c) and (d)

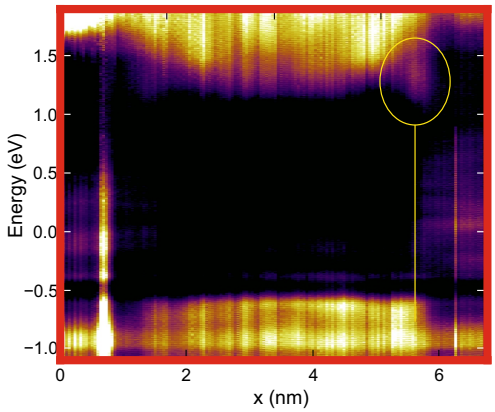

(c) Flat side

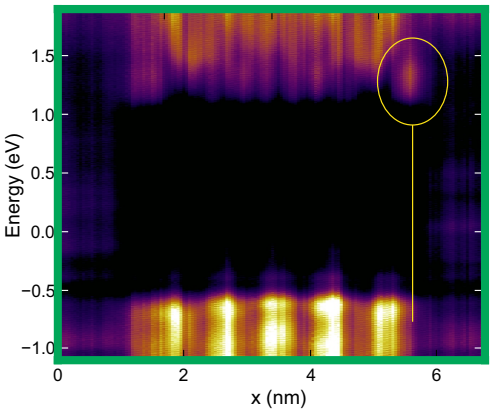

(d) Polymer side

Figure 5.1 $N = 5+/7$ heterojunctions. (a) STM image of a partially cyclodehydrogenated PA polymer. (b) Model of a $N = 5+$ section in between two $N = 7$ sections and linescan traces on both sides of the structure. The yellow rectangle marks the interface. (c) Equidistant $\frac{dI_t}{dV_B}(E, x)$ spectra recorded on the cyclodehydrogenated side of the $N = 5+$ section along the red line indicated in (b). (d) Analogous $\frac{dI_t}{dV_B}(E, x)$ spectra recorded on the polymer side of the $N = 5+$ section along the green line indicated in (b).

tion in between two $N = 7$ sections. These sections can be seen as a 5-AGNR with additional benzene rings orthofused to the naphthalene units, which may change the electronic properties significantly and hence the abbreviation 5+-AGNR. The additional benzene rings in the $N = 5+$ section are bent up and down alternatingly, similar to the structure of the initial polymer. Due to the underlying substrate, the downwards bend is marginal. The terminal benzene ring that is next to the $N = 7$ section, is always bent upwards. This means that for a downwards bend benzene ring the energy barrier to partially cyclodehydrogenate and form the 7-AGNR is significantly lower than for an upwards bend benzene ring which has a larger separation to the gold surface. Another consequence is that the length of the $N = 5+$ sections is an odd integer multiple of antracene units.

Figures 5.1(c) and (d) show equidistant $\frac{dI_t}{dV_B}(E, x)$ spectra recorded along straight lines across a double $N = 7/5+/7$ heterojunction on the flat and the polymer side

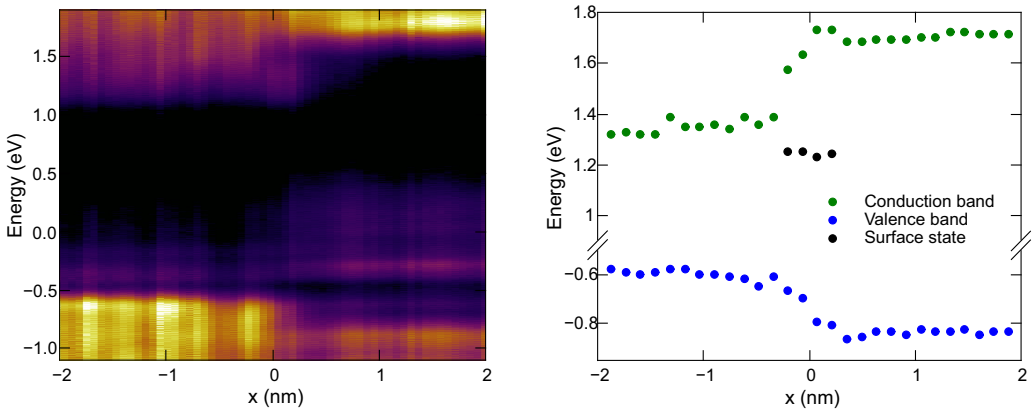

(a) Band bending STS **(b)** Band edges

Figure 5.2 Band shifting in $N = 5+/7$-AGNR heterojunctions. (a) Equidistant $\frac{dI_t}{dV_B}(E, x)$ spectra recorded on the cyclodehydrogenated side of a single $N = 5+/7$ heterojunction, similarly as indicated by the red line in Fig 5.1(b). The interface is at $x = 0$ nm. (b) Band edges of the accessible states in (a).

of the $N = 5+$ section, respectively. The scan lines are indicated in Fig 5.1(b). The measurements show similar features, most strikingly a localized interface state with onset 1.23 ± 0.05 eV, slightly lower than the onset of the CB. On both sides it has a broadening of 0.6 nm. The most prominent difference is the intensity corrugation in the occupied states on the polymer side of the $N = 5+$ section. This is related to the upwards bent benzene rings, which show an increased LDOS. This feature is not observed in the unoccupied states.

The most interesting characteristic is certainly the behavior of the electronic bands, especially the VB and CB within the heterojunction. Figure 5.2(a) displays equidistant $\frac{dI_t}{dV_B}(E, x)$ spectra across an $N = 5+/7$-AGNR heterojunction on the flat side of the structure. Reading the positions of the band edges of the accessible bands at 80% peak height (see [112] for details), gives quantitative insight into the band bending around the interface. This data is presented in Fig. 5.2(b) and clearly presents a sharp evolution of the electronic bands and the position of the interface state. Due to the risk of tip-induced cyclodehydrogenation, I_t had to be restricted, thus the CB of the $N = 7$ section is not accessible because of the large tip-sample separation. In principal, it would be possible that the CB in the $N = 5+$ section is hidden too. Preliminary ab initio calculations predicts the interface state to be at a slightly lower energy than the CB [144]. This is the case for the first observed unoccupied band in Fig. 5.2(a). The CB of the $N = 5+$ section and the CB+1 of the $N = 7$ sections show a significant

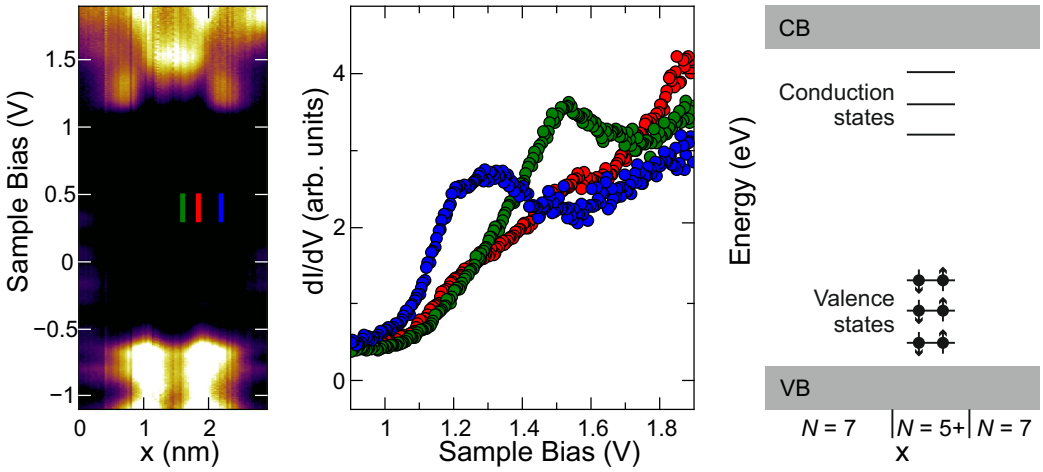

(a) 1.3 nm long $N = 5+$ section

(b) $N = 7/5+/7$ quantum dot energy levels

(c) Energy level structure of a quantum dot

Figure 5.3 $N = 7/5+/7$ quantum dot. (a) Equidistant $\frac{dI_t}{dV_B}(E, x)$ spectra across the polymer side of a 1.3 nm long $N = 7/5+/7$ double heterojunction. (b) Selected $\frac{dI_t}{dV_B}(E)$ spectra as marked in (a). (c) The energy level structure of a quantum dot shows discrete conduction and valence states.

shift of 0.39 ± 0.03 eV only about 0.2 nm away from the interface. Albeit the CB of the $N = 7$ section is hidden, it can be expected that the energy shift occurs in the same spatial range as for the CB+1. This band offset of 0.21 ± 0.02 eV and narrow interface region over which the band shift occurs identifies an average electric field of $5.3 \times 10^7 \frac{\mathrm{V}}{\mathrm{m}}$. This is about two orders of magnitude larger than the electric fields found in traditional semiconductor p-n junctions, which have a much wider depletion region [145]. Also, the average electric field is larger by a factor of approximately 5 compared with doped chevron-type GNR heterojunctions [137]. Such a narrow region with a strong electric field in a type I heterojunction can be used in devices with a small feature size like quantum dots [139, 140].

The problem of hidden electronic states is the same for the occupied states in the $N = 5+$ section. The first onset is found at $E = -0.58 \pm 0.01$ eV. Though it cannot be confirmed that there is a hidden band closer to E_F, the state found at $E = -0.58$ eV will be considered as VB maximum of the $N = 5+$ section. The energy shift in the VB is 0.25 ± 0.02 eV and thus slightly larger than in the CB. The frontier bands of the $N = 5+$ section are inside the band gap of the $N = 7$ section which means the heterojunction is classified as a straddling gap type II heterojunction.

In the introduction of this chapter, the possibility of fabricating artificial atoms

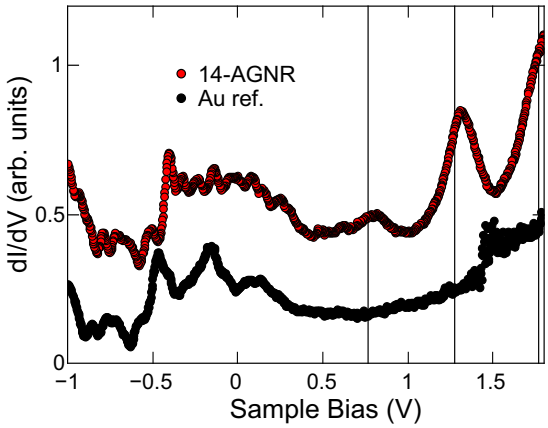

Figure 5.4 STS spectrum on a 14-AGNR. Two $\frac{dI_t}{dV_B}(V_B)$ spectra recorded on a 14-AGNR (red) and on the Au(111) surface for reference (black). The vertical lines mark the onsets of the observable GNR states.

by placing a third monomer as coupling component in between the heterojunction. A little less elaborate quantum dot system can be realized with a double $N = 7/5+/7$ heterojunction, similar to the one shown in Fig. 5.1. By reducing the size of the $N = 5+$ section, discrete, atom-like valence and conduction states develop in this lower band gap region and the interface states are additional discrete states in the system. Figure 5.3(a) shows a 1.3 nm long $N = 7/5+/7$ double heterojunction and a selection of three sprectra in Fig. 5.3(b), which illustrate the discrete states. The VB and CB of the heterojunction system are show a slight increased searation on 0.15 eV compared to the long $N = 5+$ sections. In the discrete states, which are exemplary illustrated in Fig. 5.3(c), excitons can be trapped and recombined by creating narrow line-width single photons [146, 147].

5.2 $N = 7/14$ armchair graphene nanoribbons

The second heterojunction that is investigated is made up of $N = 7$ and $N = 14$ armchair GNRs. The fabrication of 14-AGNRs via fusion of two 7-AGNRs has been discussed in Section 3.3. This is an uncontrolled reaction, where ribbons bind to a neighboring ribbon at random arrangement. The result are heterojunctions of armchair GNRs with different sections of widths $N = 7$ and $N = 14$.

As a first investigation of the electronic properties of the $N = 7/14$ armchair GNRs, the electronic structure of the 14-AGNR section was measured with standard STS. Figure 5.4 shows two $\frac{dI_t}{dV_B}(V_B)$ spectra recorded on a 14-AGNR and on the Au(111) surface for reference. Three onsets at $V_B = 0.75$ V, $V_B = 1.27$ V and $V_B = 1.78$ V

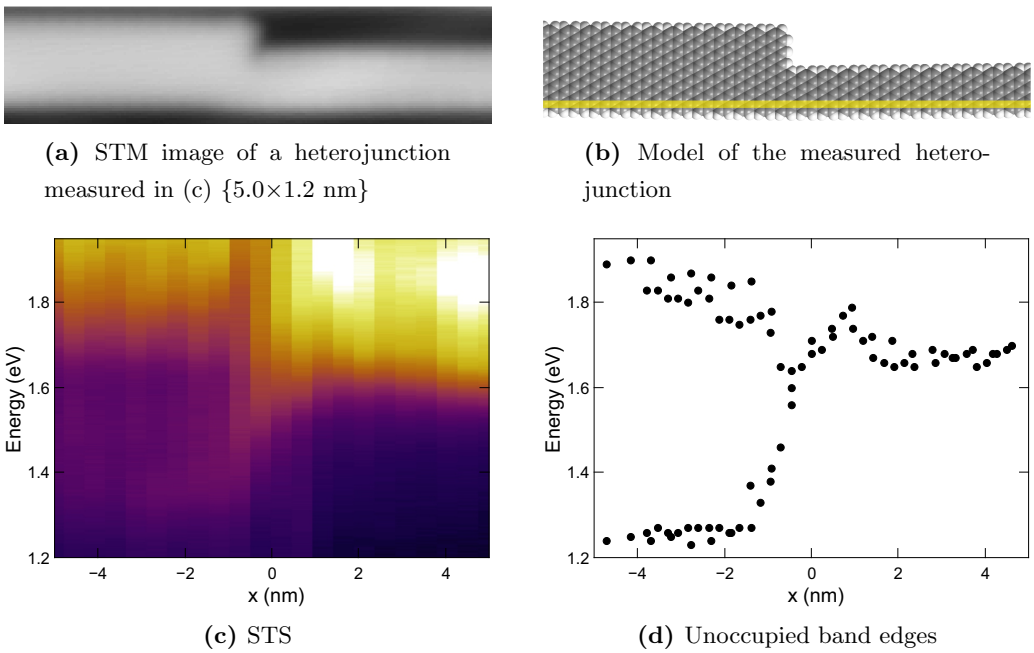

(a) STM image of a heterojunction measured in (c) {5.0×1.2 nm}

(b) Model of the measured heterojunction

(c) STS

(d) Unoccupied band edges

Figure 5.5 Band shifting in $N = 7/14$-AGNR heterojunctions. (a) STM image of an $N = 7/14$ heterojunction fabricated via fusion of two 7-AGNRs. (b) Model of the heterojunction in (a) with a yellow line marking the linescan. (c) Equidistant $\frac{dI_t}{dV_B}(E, x)$ spectra recorded along the yellow line indicated in (b). (d) Band edges of the accessible states in (c).

can be identified. The onsets were determined at the position of 80% peak height for the reasons discussed in Section 4.1.1. The first onset at $V_B = 0.75$ V is very sensitive to the shape of the tip and it is not clear whether this is an intrinsic state of the 14-AGNR. The two onsets at $V_B = 1.27$ V and $V_B = 1.78$ V are always observed. The 14-AGNRs belong to the semimetallic $3p$+2 family as evidenced by the touching VB and CB at $k = 0$. The DFT values shown in Fig. 1.13(b) suggest a band gap of about 0.5 eV. Despite factors like the underestimation of band gaps with LDA or the absence of the metallic surface in the calculations, it nevertheless is highly unlikely that the observed onset at $E = 1.27$ eV is the CB of the $N = 14$ section but rather the CB+1. If the state at onsets at $V_B = 0.75$ V was an intrinsic state of the 14-AGNR, it may be the CB, as the polarization of the underlying surface moves E_F to lower energies.

The heterojunctions were fabricated by annealing Au(111) samples with 7-AGNRs to 450°C. The 7-AGNRs grow together via the proposed reaction mechanism illustrated in Fig. 3.19. Due to the nature of this reaction, the GNR heterojunction has one continuous armchair edge on one side, while the width reduction on the other side

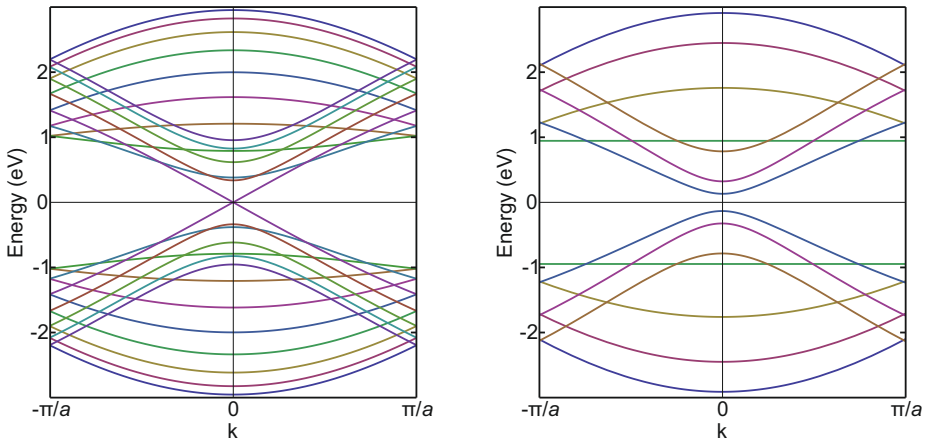

(a) Bandstructure 14-AGNR **(b)** Bandstructure 7-AGNR

Figure 5.6 Calculated band structures of $N = 14$ and $N = 7$ AGNR sections. Tight binding band structures from Equation 1.8 with $\gamma_0 = 1$ in the range $-\frac{\pi}{a} \leq k \leq \frac{\pi}{a}$.

is accomplished with a zigzag edge in a 90° angle to the armchair edges. The images in Fig. 5.5(a) and (b) show such an $N = 7/14$ heterojunction.

Figure 5.5(c) shows equidistant $\frac{dI_t}{dV_B}(E, x)$ spectra recorded along a straight line across the $N = 7/14$ heterojunction. The scan line is indicated in Fig 5.5(b). As expected, the CB+1 at $E = 1.68 \pm 0.03$ eV is found in the $N = 7$ section. In the $N = 14$ section, the first onset is found at 1.25±0.02 eV and a second one at 1.81±0.06. Figure 5.6(a) depicts the tight binding band structure of 14-AGNRs calculated with Equation 1.8.

Like previously, reading the positions of the band edges of the accessible bands at 80% peak height, gives a band diagram shown in Fig. 5.5(d). The observed shift of 0.43 ± 0.04 nm between the respective CB+1s at the heterojunctions interface occurs in a range of 1.8 ± 0.4 nm. Assuming, that the shift of the CBs happens within the same range, it can be expected that the electric field in the heterojunction is in the order of $10^6 \frac{\mathrm{V}}{\mathrm{m}}$, one order of magnitude lower than in $N = 7/5+$ heterojunctions. This indicates a similar behavior found in carbon nanotube-metal heterojunctions, where the interface range of band shifts increases with diameter [148]. In the $N = 7/14$ heterojunction, the two bands are connected at the interface, which seems not to be the case in the previously presented $N = 5+/7$ heterojunction.

Chapter 6

Conclusions

At the end of this report it is time to reflect on the achieved results and the research ahead. The central topics of this thesis were the fabrication of atomically precise graphene nanoribbons and the study of their electronic properties. The starting point of this research was the recent fabrication of atomically precise $N = 7$ armchair graphene nanoribbons, which was a proof of concept for the bottom-up synthesis of these technologically interesting nanostructures. The motivation was to experimentally verify the electronic properties that theory had been predicted. Additionally, the fabrication of GNRs of different widths was desired to widen the understanding of both, the synthesis of GNRs and their electronic properties. The presented research has improved the understanding of the synthesis and the electronic structure of GNRs. Along the way, a deeper understanding of differential conductance spectra was achieved, which will help to correctly measure and analyze nanostructures in future research.

GNR fabrication

In Section 1.6 an overview of graphene and its nanostructures was given. The growth of 7-AGNRs from previous works have been discussed in detail in Section 3.1. In order to complete the picture, the termini were studied which answered the last open question about the exact chemical structure. The study of the influence of hydrogen partial pressure and polymerization temperature gave insight into more details of the synthesis, especially in the light of growth limitations. A new armchair GNR was presented in Section 3.2. Here, the separate steps in the fabrication process of this 9-AGNR were studied, including DFT simulation supported models of each step. An unusual intermediate step was found, where the polymer is only partially

cyclodehydrogenated.

Electronic band structure

Chapter 4 was dedicated to the investigation of the electronic properties of the 7- and 9-AGNRs. At first, the influence of the confinement in the long direction of the GNRs was studied. Short ribbons have electronic properties of molecules with quantized electronic states and strongly depend on the termini. Only in armchair GNRs that have a length of at least $20a$ (8.5 nm) the bulk properties of 7-AGNRs are observed, which are, by implication, independent of the termini. In the following it was explained how to use standing wave patterns that arise from scattering processes to extract the band structure. This FT-STS technique was then applied to the 7- and 9-AGNRs.

During the investigation, is was observed, that the charge carrier density decays unequally away from the surface for different electronic states. As a result, states had been missed in standard differential conductance spectra of previous works. The straight forward solution is to decrease the tip-sample distance by increasing the tunneling current. This is, however, not possible with all structures as high tunneling currents can induce chemical reactions like the presented tip-induced cyclodehydrogenation. FT-STS can sometimes circumvent this problem by extracting the band onset from fits to the accessible band structure as it was shown for the conduction band of the 7-AGNR.

Heterojunctions

Two different heterojunctions have been fabricated using only the precursor monomer for the 7-AGNR synthesis. Critical temperatures in the final fabrication step forms $N = 5+/7$ and $N = 7/14$ armchair GNR heterojunctions. Due to a narrow interface region, both heterojunctions exhibit an internal electric field which is much stronger than in traditional semiconductor p-n junctions.

Outlook

From the outlined research results some new interesting questions evolved which can be investigated in further experiments. In the following a brief outlook on possible future projects is given.

The bottom-up fabrication of atomically precise nanostructures is still in the fledgling stages. At present, only very few GNRs can be produced with reasonable quality and only one of them is a straight zigzag edge GNR. Step by step a knowledge

base for the requirements on the monomer precursor molecules is built up. The next steps following the control of the growth of single structures is to fabricate more complex structures with well designed electronic and magnetic properties. For a working device it will be crucial to reliably transfer the structures onto insulator substrates or, even better, fabricate them on such substrates. Already the investigated fabrication of 9-AGNRs has two significant open questions. The first one is the uncertainty of the exact arrangement of the $N = 9$ precursor monomer islands. The second one is the chemical structure of the partially cyclodehydrogenated polymer. An XPS study has the potential to reveal the temperatures when the precursor monomers loose their first and second bromine atoms. At higher temperature, XPS may be able to reveal how many hydrogen atoms are detached in the partial cyclodehydrogenation. Ideally, this information identifies exactly one structural possibility.

In order to design functional nanostructures, the properties of all parts must be known. So far, spectroscopy measurements on GNRs, which average over an area, provided unreliable results of the electronic structure. The FT-STS method, that was implemented in this thesis, has proven to be a powerful tool in determining the electronic properties. Especially in future with more complex nanostructures, this will be an even more powerful tool, as it provides the possibility of measuring specific sections of a complex structure, e.g. heterojunctions or kinks, without averaging.

The research presented in this thesis is part of initial research in of the development of new materials for the large scale production of electronic devices with feature sizes around 1 nm where atomic precision is crucial.

Appendix A

Other Research

In the previous chapters, the major topics of this thesis have been discussed. During the research, several side projects have been studied. Additionally, some approaches have not been satisfactorily successful. However, successful and unsuccessful projects have produced valuable results.

A.1 Tip functionalization for STS

In Section 1.4, the advantages of functionalizing the tip with a CO molecule in nc-AFM experiments has been discussed. It has been shown in previous experiments that it is possible to increase the resolution of an STM tip by functionalizing the tip with a CO molecule [31]. The higher resolution can be explained not only by the sharpness of the CO tip, but also by the tunneling through the p-wave orbitals of the CO molecule.

For STS, using a CO functionalized tip means that the assumption of a constant n_t in Equation 1.1 is invalid and consequently, the $\frac{dI_t}{dV_B}$ is not proportional to n_s. However, n_t of a CO tip should be predictable and, hence, the tip states in the STS spectra should be identifiable. CO has a HOMO-LUMO gap of about 7 eV and, hence, the CO should not take part in the tunneling process withing this 7 eV range [149]. Effects of tip states in spectroscopy are, for example, discussed in [150].

The CO functionalization works by placing the tip above a CO molecule on a sodium chloride (NaCl) island. CO appears dark in STM images as shown in Fig. A.1(a). Increasing I_t forces the feedback to bring the tip closer to the surface. At a certain point, the CO molecule attaches to the tip changing I_t. As a result the feedback reacts by pulling the tip away from the surface in order to maintain the set I_t.

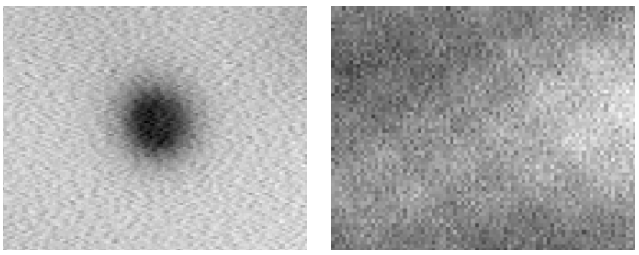

(a) Before **(b)** After

Figure A.1 CO pickup. (a) Within the usual measurement parameters, a CO molecule appears as a hole in the surface when measures with a metal tip. (b) After successful CO pickup, the same area can be measured with atomic resolution. $\{2.5 \times 2.0$ nm$\}$

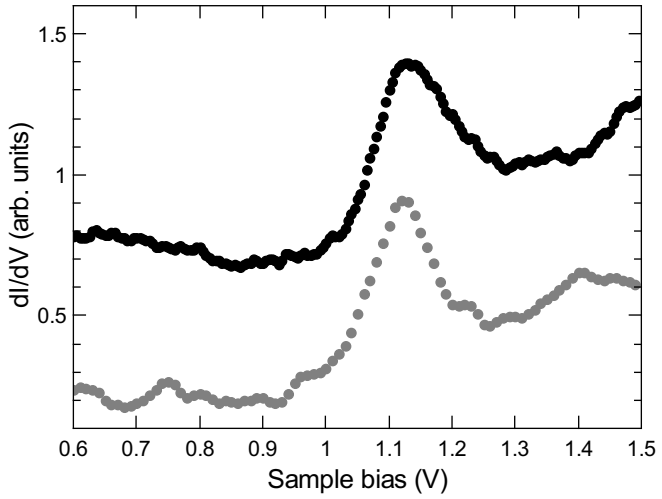

Figure A.2 STS with a CO functionalized tip. The two spectra were recorded on a 9-AGNR immediately before CO pickup with a bare metal tip (black) and immediately after with a CO functionalized tip (grey).

In order to check the usability of a CO functionalized tip, STS spectra were compared to similar STS spectra with a bare metal tip. NaCl was deposited on a Au(111) surface, where it forms 2 monolayer thick islands. After exposing the sample to CO at a pressure of 3×10^{-5} mbar for 3 minutes, CO molecules could easily be found on the salt islands. A CO molecule on NaCl sits perpendicular to the surface on top of a sodium ion with the carbon atom down [151]. The CO molecule holds a small dipole moment oriented towards the substrate i.e. the oxygen atom carries a small positive partial charge [30].

Figure A.2 shows two spectra that were recorded on the edge of a 9-AGNR. The

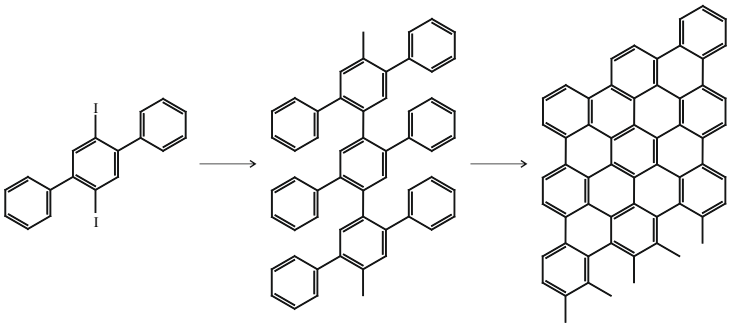

Figure A.3 Reaction scheme from DITP via a polymer to 9-AGNR.

black spectrum was recorded just before the CO pick-up. With a CO a spectrum with exactly the same settings and at the same position was taken (grey). The CB peak is slightly sharper with a full width at half maximum of 0.09 V compared to 0.11 V with the metal tip.

The tip functionalization with CO molecules for STS worked only for positive sample biases, at negative biases, the CO was detached from the tip. So in general, the improvement for single spectra is marginal. The main use of tip functionalization is the reproducible high spacial resolution and this is exactly where the advantage for STS experiments lies, too. Within the energy restrictions, the spacial expansion of a localized state can be measured more precisely or higher modes in standing wave pattern can be resolved.

A.2 Alternative molecule for $N = 9$ armchair graphene nanoribbons

When designing a precursor monomer for a specific nanostructure on paper, usually more than one option is possible. However, several factors can limit the usefulness of a monomer. For sublimation, the monomers should not be too large, as the sublimation temperature of hydrocarbons increases with size. A higher sublimation temperature increases the risk of degrading the molecules or inducing unwanted reactions. A possibility to circumvent this problem is using a solvent for the transfer onto the surface [15,152]. But not only during sublimation degradation or the loss of functional groups can occur. The chemical stability must be given during on-surface annealing, too. False coupling is another major issue, which deforms the final nanostructure.

For the synthesis of 9-AGNRs, 2',5'-diiodo-1,1':4',1"-terphenyl (DITP) would also yield the desired result. The reaction scheme is shown in Fig. A.3. The steps are the same as for the other precursor monomer reactions. After deposition on Au(111),

the monomers are dehalogenated and, via radical addition at the activated connection points, a covalently bond polymer is formed. Subsequent cyclodehydrogenation yields the final fully flat 9-AGNR.

DITP has a sublimation temperature of 130°C and thus lower than DBBA for the fabrication of 7-AGNRs. Dehalogenation and polymerization was done simultaneously by annealing at 175°C and the final cyclodehydrogenation by annealing at 350°C. The result of this procedure is shown in Fig A.4. Relatively long 9-AGNRs were formed but they show a high degree of defects. The high-resolution STM image in Fig A.4(b) shows the two main defects: cavities which have the same structure as the ones in 9-AGNRs from DBTP and additions to the armchair edge. Similarly, the cavities are a result of the detachment of phenyl groups. By the reason of the much higher number of defects, the mechanical stress must be stronger on the carbon-carbon bond that attaches the phenyl group. The origin of the addition defect on the armchair edge is not clear. Judging from its size it seems likely that the additions are the detached phenyl groups that cause the cavity defects. However, these additions have never been observed when DBTP was used as monomer precursor. Another defect is shown in Fig. A.4(a). Kinks with an angle of 120° disrupt the straight nature of the 9-AGNRs. These kinks are most likely due to a low purity of the DITP. A similar molecule with the second iodine atom at the 6' instead of the 5' position (2',6'-diiodo-1,1':4',1"-terphenyl) results in the observed kinks.

The here used monomer precursor (DITP) is basically the same molecule that was formed as an intermediate for the fabrication of $N = 15$ armchair GNRs [153]. A para-phenyl with two bromine atoms at opposing sites on the central benzene ring was synthesized by regioselective Suzuki coupling of 4-biphenylboronic acid with 1,4-dibromo-2,5-diiodobenzene. The $N = 15$ armchair GNRs which were fabricated from this monomer precursors were, however, of a similar limited quality as the 9-AGNRs using DITP.

A.3 Decoupling

So far in this work, the GNRs studied were on a Au surface. As all organic nanostructures and molecules, they interact through their π-orbitals with the free electron gas of metal surfaces. With or without chemical reaction, this leads to charge transfer between GNRs and surface [154–156]. When studying the properties of nanostructures on a metal surface it is therefore desirable to decouple the nanostructures from the substrate. This is particularly important for electronic devices because leak currents through the surface will suppress the functionality of the device. In order to avoid

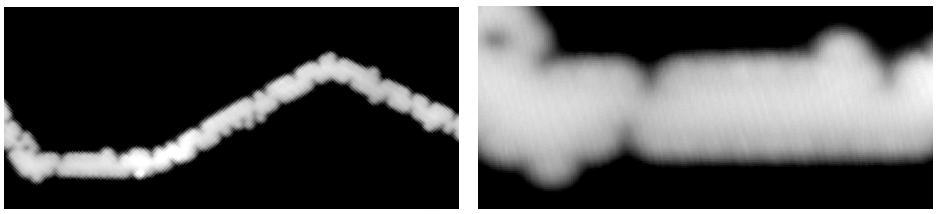

(a) Overview {26 × 12 nm} **(b)** Magnification {6.2 × 2.8 nm}

Figure A.4 9-AGNR alternative precursor monomer. The GNRs show a significant amount of cavity defects, due to the detachment of phenyl groups, and kinks, due to faulty coupling.

such interactions, an insulating layer with a several eV band gap can acts as a tunnel barrier towards the metal. It has been demonstrated that 3 monolayers of NaCl already disentangle the electronic structure of adsorbed pentacene molecules from the influence of the substrate [157]. This way, the unperturbed gas-phase like frontier orbitals of pentacene could be imaged.

There are several procedures for decoupling nanostructures. One way is to transfer them completely onto another substrate by using a transfer material like PMMA [15, 64, 137], by intercalation of insulating materials [152, 158, 159] or moving them onto insulating, few monolayer thick islands [160, 161].

A.3.1 $N = 7$ armchair graphene nanoribbons on NaCl and KCl

Potassium chloride (KCl) and NaCl are two classical salts that are used to electronically decouple molecules from a metal surface. They have huge electronic band gaps of 8.4 eV and 8.5 eV, respectively. [162]. Additionally, they can form stable 2 monolayer thick films in carpet mode without clustering on most surfaces [163, 164].

The idea for decoupling GNRs was to evaporate NaCl or KCl onto a 7-AGNR on Au(111) sample. There they would form few monolayer thick islands while reducing the space for the GNRs. Eventually the space would be too small and the GNRs would be forced to go on top of the salt islands.

The 7-AGNRs were grown via the deposition of DBBA and subsequent annealing to 175°C and 320°C. The sublimation was done at 500°C (NaCl) and 470°C (KCl) for 45 seconds each while the substrate was annealed to 200°C. After the deposition of NaCl and KCl, the salt islands pushed the 7-AGNRs together as depicted in Fig. A.5(a) and (b). When increasing the salt coverage, the GNRs did not go on top of the islands but they were grown over by the islands. This is shown in Fig. A.5(c) in which a NaCl island grew over the 7-AGNRs in carpet mode. This way the GNRs show up

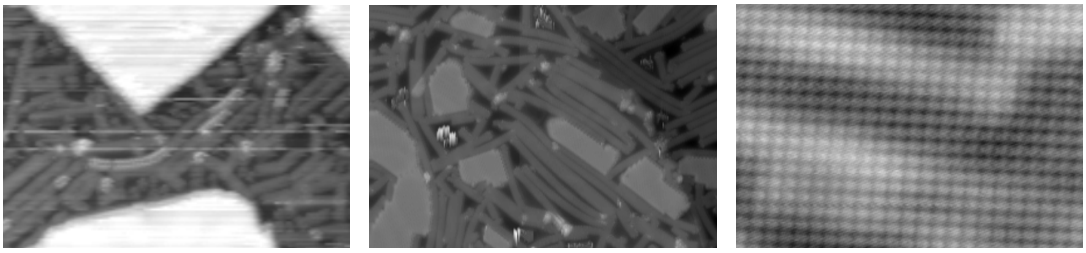

(a) NaCl {50 × 35 nm} **(b)** KCl {50 × 35 nm} **(c)** Salt covered {8.0 × 5.6 nm}

Figure A.5 NaCl and KCl on 7-AGNR samples. (a) NaCl forms large islands and squeezes the 7-AGNRs together. (b) KCl forms many small islands between the GNRs. (c) Both, NaCl and KCl cover the GNRs at higher coverage.

as corrugations in the continuous islands. A decoupling of the GNRs from the metal surface is not achieved.

A.3.2 $N = 7$ armchair graphene nanoribbons on graphene

The properties of graphene have been studied intensively since its discovery ten years ago. Despite the missing bang gap, graphene can efficiently decouple molecules from strongly interacting metallic surfaces. However, the degree of decoupling depends strongly on the underlying substrate. While graphene on iridium(111) is electronically homogeneous and almost neutral, graphene on ruthenium(0001) exhibits charge inhomogeneities and a surface potential corrugation [165–167]. Several molecules have been placed on graphene, all of which show differences on the substrate [168, 169]. In case of TCNQ on graphene a small charge transfer the electronic decoupling can range from one electron per molecule to practically zero [167, 170].

In order to place 7-AGNRs onto graphene, two samples were prepared. The first sample was a high-coverage 7-AGNR on Au(111) sample which was prepared via the deposition of DBBA and subsequent annealing to 200°C and 380°C. The second sample was a graphene on ruthenium(0001) sample which was prepared by thermal decomposition of ethylene. The ruthenium surface was annealed at 1425°C while being exposed to ethylene at a partial pressure of 10^{-7} mbar for 10 minutes. The ethylene molecules dehydrogenate at the surface. The remaining carbon atoms diffuse on the surface and form the graphene. After the fabrication, both samples were taken out of the UHV system and placed with the prepared surfaces on top of each other. After this mechanical transfer, the ruthenium sample was introduced back into the UHV system. As a last step this sample was annealed at 200°C, which removed molecules

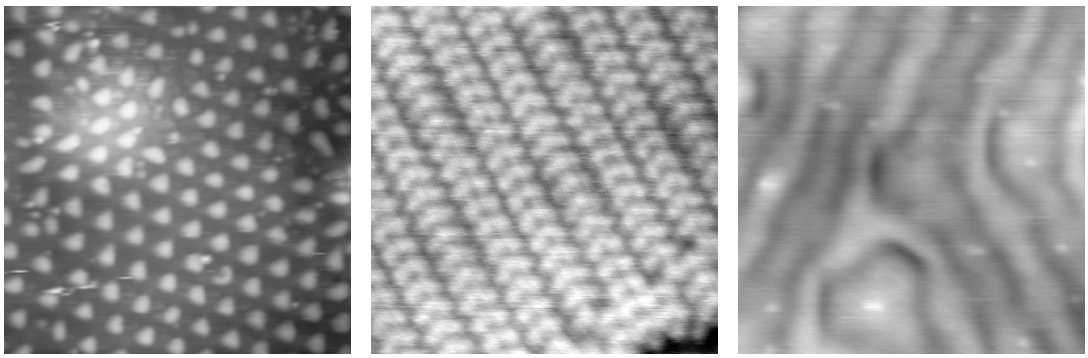

(a) Graphene {32 × 32 nm} **(b)** 7-AGNRs {6.0 × 6.0 nm} **(c)** Au island {17 × 17 nm}

Figure A.6 Three areas of a graphene-decoupled 7-AGNR sample. (a) Graphene on ruthenium(0001) exhibiting the distinct Moiré pattern. (b) Island of densely packed 7-AGNRs lying on graphene. (c) Corrugated Au island on graphene.

and atoms that had been adsorbed outside the UHV system. Both, graphene and 7-AGNRs are stable at ambient pressures and after annealing they can be studied in UHV [43, 171].

Figure A.6 shows all three areas found on the prepared sample. The area in (a) exhibits the regular Moiré pattern of graphene on ruthenium(0001). The area in (b) shows 7-AGNRs which form compact islands on graphene. Finally, the third area shown in (c) is a slightly corrugated Au island. The observed graphene shows a Moiré pattern due to the lattice mismatch between graphene (0.246 nm) and ruthenium (0.271 nm). The features of the pattern show no difference to previous graphene on ruthenium(0001) studies [172, 173].

The appearance of the 7-AGNR islands is rather peculiar. Instead of perfectly symmetric ribbons, they appear as rows of bend bananas (Fig A.6(b)). The distance from the center of one 7-AGNR to the neighboring one is 0.77 ± 0.02 nm and they have a feature size of 0.42 ± 0.02 nm. This is in perfect agreement with the 7-AGNR's width of 0.74 nm and unit cell length of 0.43 nm. The reason for the asymmetric appearance is not understood, but it is most likely related to the edges of the GNR islands. The bend features appear concave towards the island edge as shown in Fig A.6(b). The asymmetry of the inner island GNRs must then be induced by the outer ones. Figure A.7(a) shows the border of a 7-AGNR island which is confined by the Moiré pattern of graphene, indicating the relation to the spacial nonuniform surface potential of graphene on ruthenium(0001) [167]. Organic molecules have been shown to have preferential sites and direction within the Moiré pattern [167, 170]. The step height

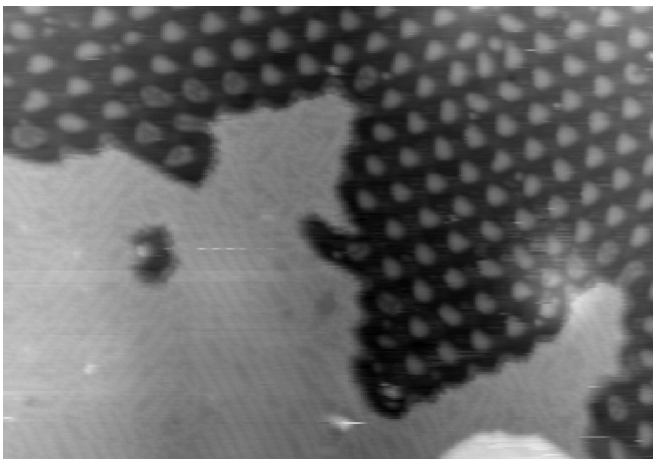

(a) 7-AGNR island border on graphene {50 × 35 nm}

(b) $V_B = -3.0$ V {4.0 × 2.0 nm}

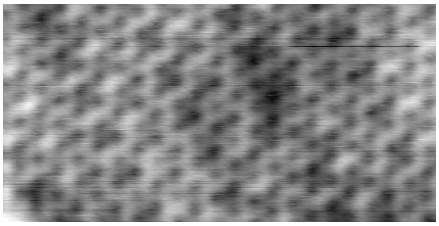

(c) $V_B = -1.0$ V {4.0 × 2.0 nm}

Figure A.7 7-AGNR islands on graphene. (a) STM image of a border of a 7-AGNR island edge on graphene on ruthenium(0001). (b) STM image at $V_B = -3.0$ V of 7-AGNRs exhibiting the asymmetric appearance. (c) STM image of the same area as in (b) at $V_B = -1.0$ V.

of the 7-AGNR islands is 0.27 ± 0.01 nm, which is significantly lower than the layer spacing of graphite (0.335 nm [174]). This has to be related to the interaction of the 7-AGNRs with the metal substrate. Another evidence is the absence of a Moiré pattern which is fully suppressed. A feature of the semiconducting nature of the GNR islands is shown in Fig. A.7(b) and (c): At $V_B = -3.0$ V the GNR can be clearly seen and they disappear when reducing V_B to -1.0 V, consequently, the underlying graphene structure can be observed.

The Au island on graphene on ruthenium(0001) shown in Fig A.6(c) exhibits a vague herringbone like reconstruction. These islands are always lying on top of graphene with a step height of 0.33 ± 0.02 nm, which is in the range of the layer spacing of graphite but much larger than the step height of a terrace of the Au(111) surface (0.235 nm [175]). It can be excluded that Au lies directly on the ruthenium(0001) surface as it would show straight and evenly spaced corrugations [176]. Similarly, it can

be excluded, that Au has intercalated and lies between the ruthenium(0001) surface and graphene, which would display a $2\sqrt{3} \times 2\sqrt{3}R30$-Au(111) surface reconstruction [177, 178].

A.4 Conclusions

Other research that has been conducted was less successful or, in the case of decoupling with graphene, the results are not fully understood and so far restrictions have prevented clarifying additional experiments. But even those experiments gave valuable information and ideas for viable approaches in the future.

The tip functionalization with CO molecules for STS worked only for positive sample biases and the increased sharpness of the peaks was marginal. However, within these limitations the advantage for STS experiments lies in the increased resolution compared to relatively blunt metal tips.

An alternative precursor monomer (DITP) for the synthesis of 9-AGNRs was presented. Due to its shortcoming in chemical stability and coupling orientation, the final GNRs exhibit a large number of defects. Therefore, they are unusable for analyzing bulk properties of 9-AGNRs.

Decoupling 7-AGNRs by depositing the salts NaCl and KCl onto the surface was not achieved, because the salt islands grew over the GNRs in carpet mode. It does, however, show a way of shielding the nanosructures from ambient gases or molecules deposited on the surface.

The transfer of 7-AGNRs onto a graphene/ruthenium(0001) sample worked well. Large areas of clean graphene was found. Other areas had layered Au islands and 7-AGNR islands. The GNRs show a significant interaction with the substrate and appear non-symmetrically in STM images.

Bibliography

[1] J. Rifkin, *The Third Industrial Revolution; How Lateral Power is Transforming Energy, the Economy, and the World*, Palgrave MacMillan, 2011.

[2] G. E. Moore, Electronics **38**, 114 (1965).

[3] C. Nuttall, Intel's chip plans bloom in Arizona desert, 2012.

[4] S. A. Wolf et al., Science **294**, 1488 (2001).

[5] D. P. DiVincenzo, Science **270**, 255 (1995).

[6] Y. Ding, Y. Wang, S. Shi, and W. Tang, The Journal of Physical Chemistry C **115**, 5334 (2011).

[7] Z.-D. Yang, W. Wu, and X. C. Zeng, Journal of Materials Chemistry C **2**, 2902 (2014).

[8] M. H. D. Guimarães, P. J. Zomer, I. J. Vera-Marun, and B. J. van Wees, Nano Letters **14**, 2952 (2014).

[9] J. Hong, E. Bekyarova, W. a. de Heer, R. C. Haddon, and S. Khizroev, ACS nano **7**, 10011 (2013).

[10] S. Park, M. Vosguerichian, and Z. Bao, Nanoscale **5**, 1727 (2013).

[11] J. R. Sanchez-Valencia et al., Nature **512**, 61 (2014).

[12] L. Grill et al., Nature Nanotechnology **2**, 687 (2007).

[13] W. Y. Kim, Y. C. Choi, and K. S. Kim, Journal of Materials Chemistry **18**, 4510 (2008).

[14] A. Liscio, E. Orgiu, J. M. Mativetsky, V. Palermo, and P. Samorì, Advanced materials **22**, 5018 (2010).

[15] L. Chen, Y. Hernandez, X. Feng, and K. Müllen, Angewandte Chemie **51**, 7640 (2012).

[16] J. M. Tour, Chemistry of Materials **26**, 163 (2014).

[17] G. Binnig, H. Rohrer, C. Gerber, and E. Weibel, Physical Review Letters **49**, 57 (1982).

[18] D. M. Eigler and E. K. Schweizer, Nature **344**, 524 (1990).

[19] J. A. Stroscio and W. J. Kaiser, *Scanning Tunneling Microscopy, Methods of Experimental Physics*, Academic Press, San Diego, 27 edition, 1993.

[20] B. Naydenov and J. J. Boland, Physical Review B **82**, 245411 (2010).

[21] A. Batra et al., Chemical Science **5**, 4419 (2014).

[22] F. Flores and J. Ortega, Basic Theory of the Molecule-Metal Interface, in *The Molecule-Metal Interface*, edited by N. Koch, N. Ueno, and A. T. Wee, chapter 2, pages 17–49, WILEY-VCH Verlag, Weinheim, 2013.

[23] A. Guerrero et al., ACS Nano **6**, 3453 (2012).

[24] C. E. Klots, The Journal of Chemical Physics **60**, 1177 (1974).

[25] A. L. Smith and P. Tan, Journal of Chemical Education **83**, 1654 (2006).

[26] W. Kaim and M. Moscherosch, Coordination Chemistry Reviews **129**, 157 (1994).

[27] Y. Martin, C. C. Williams, and H. K. Wickramasinghe, Journal of Applied Physics **61** (1987).

[28] F. J. Giessibl, Reviews of Modern Physics **75**, 949 (2003).

[29] L. Gross, F. Mohn, N. Moll, P. Liljeroth, and G. Meyer, Science **325**, 1110 (2009).

[30] M. Schneiderbauer, M. Emmrich, A. J. Weymouth, and F. J. Giessibl, Physical Review Letters **112**, 166102 (2014).

[31] L. Gross et al., Physical Review Letters **107**, 086101 (2011).

[32] V. R. Manfrinato et al., Nano Letters **13**, 1555 (2013).

[33] R. Otero, J. M. Gallego, A. L. V. de Parga, N. Martín, and R. Miranda, Advanced materials **23**, 5148 (2011).

[34] M. De Volder et al., Advanced Materials **22**, 4384 (2010).

[35] A. M. Kalsin et al., Science **312**, 420 (2006).

[36] B. Y. Kim, I.-B. Shim, O. L. a. Monti, and J. Pyun, Chemical Communications **47**, 890 (2011).

[37] R. Helmy, R. W. Wenslow, and A. Y. Fadeev, Journal of the American Chemical Society **126**, 7595 (2004).

[38] S. Krasnikov et al., Nano Research **4**, 376 (2011).

[39] L. Lafferentz et al., Nature Chemistry **4**, 215 (2012).

[40] S.-W. Hla, L. Bartels, G. Meyer, and K.-H. Rieder, Physical Review Letters **85**, 2777 (2000).

[41] J. B. Hendrickson, D. J. Cram, and G. S. Hammond, *Organic Chemistry*, McGraw-Hill, 3rd edition, 1970.

[42] J. Björk, F. Hanke, and S. Stafström, Journal of the American Chemical Society **135**, 5768 (2013).

[43] J. Cai et al., Nature **466**, 470 (2010).

[44] M. Bieri et al., Chemical Communications **47**, 10239 (2011).

[45] J. Eichhorn et al., Chemical Communications **50**, 7680 (2014).

[46] K. Swamy, P. Hanesch, P. Sandl, and E. Bertel, Surface Science **466**, 11 (2000).

[47] M. Kittelmann, P. Rahe, M. Nimmrich, C. M. Hauke, and A. Ku, ACS Nano **5**, 8420 (2011).

[48] C. D. Reddy, S. Rajendran, and K. M. Liew, Nanotechnology **17**, 864 (2006).

[49] N. Savage, Nature **483**, S30 (2012).

[50] A. K. Geim and K. S. Novoselov, Nature Materials **6**, 183 (2007).

[51] C. Berger et al., Science **312**, 1191 (2006).

[52] J. A. Venables, G. D. T. Spiller, and M. Hanbücken, Reports on Progress in Physics **47**, 399 (1984).

[53] K. S. Novoselov et al., Science **306**, 666 (2004).

[54] P. R. Wallace, Physical Review **71**, 622 (1947).

[55] Y. M. Lin et al., Science **327**, 662 (2010).

[56] M. Fujita, K. Wakabayashi, K. Nakada, and K. Kusakabe, Journal of the Physical Society of Japan **65**, 1920 (1996).

[57] K. Nakada, M. Fujita, G. Dresselhaus, and M. Dresselhaus, Physical Review B **54**, 17954 (1996).

[58] M. Igami, M. Fujita, and S. Mizuno, Applied Surface Science **130-132**, 870 (1998).

[59] K. Wakabayashi, K. Sasaki, T. Nakanishi, and T. Enoki, Science and Technology of Advanced Materials **11**, 054504 (2010).

[60] D. Gunlycke and C. White, Physical Review B **77**, 115116 (2008).

[61] J. Alfonsi and M. Meneghetti, New Journal of Physics **14**, 053047 (2012).

[62] M. Han, B. Özyilmaz, Y. Zhang, and P. Kim, Physical Review Letters **98**, 1 (2007).

[63] Z.-S. Wu et al., Nano Research **3**, 16 (2010).

[64] L. Jiao, L. Zhang, X. Wang, G. Diankov, and H. Dai, Nature **458**, 877 (2009).

[65] L. Yang, C.-H. Park, Y.-W. Son, M. Cohen, and S. Louie, Physical Review Letters **99**, 186801 (2007).

[66] M. Born and R. Oppenheimer, Annalen der Physik **389**, 457 (1927).

[67] L. H. Thomas, Cambridge Philosophical Society **23**, 542 (1926).

[68] E. Fermi, Atti della Accademia Nazionale dei Lincei **6**, 602 (1927).

[69] W. Kohn and L. J. Sham, Physical Review **140**, A1133 (1965).

[70] P. Hohenberg and W. Kohn, Physical Review **136**, B864 (1964).

[71] T. Braun, matrixfilereader, http://www.igorexchange.com/project/matrixFileReader.

[72] C. Wöll, S. Chiang, R. J. Wilson, and P. H. Lippel, Determination of atom positions at stacking-fault dislocations on Au(111) by scanning tunneling microscopy, in *Scanning Tunneling Microscopy SE - 15*, edited by H. Neddermeyer, volume 6 of *Perspectives in Condensed Matter Physics*, pages 114–117, Springer Netherlands, 1993.

[73] F. Reinert and G. Nicolay, Applied Physics A **78**, 817 (2004).

[74] W. Chen, V. Madhavan, T. Jamneala, and M. F. Crommie, Physical Review Letters **80**, 1469 (1998).

[75] S. Blankenburg et al., ACS Nano **6**, 2020 (2012).

[76] K. A. Simonov et al., The Journal of Physical Chemistry C **118**, 12532 (2014).

[77] M. Koch, F. Ample, C. Joachim, and L. Grill, Nature Nanotechnology **7**, 713 (2012).

[78] S. Linden et al., Physical Review Letters **108**, 216801 (2012).

[79] D. Basu, M. J. Gilbert, L. F. Register, S. K. Banerjee, and a. H. MacDonald, Applied Physics Letters **92**, 042114 (2008).

[80] L. Talirz et al., Journal of the American Chemical Society **135**, 2060 (2013).

[81] E. Kampshoff, N. Waelchli, A. Menck, and K. Kern, Surface Science **360**, 55 (1996).

[82] D. Broer, G. Mol, and G. Challa, Polymer **32**, 690 (1991).

[83] W. D. Cook, Polymer **33**, 2152 (1992).

[84] L. Lecamp, B. Youssef, C. Bunel, and P. Lebaudy, Polymer **38**, 6089 (1997).

[85] F. Burel, L. Lecamp, B. Youssef, C. Bunel, and J.-M. Saiter, Thermochimica Acta **326**, 133 (1999).

[86] E. Andrzejewska, Progress in Polymer Science **26**, 605 (2001).

[87] R. Zhang et al., ACS Nano **7**, 6156 (2013).

[88] G. R. Tryson and A. R. Shultz, Journal of Polymer Science: Polymer Physics Edition **17**, 2059 (1979).

[89] C. Decker and K. Moussa, Macromolecules **22**, 4455 (1989).

[90] W. D. Cook, Journal of Polymer Science Part A: Polymer Chemistry **31**, 1053 (1993).

[91] H. S. Fogler, *Elements of Chemical Reaction Engineering*, Prentice Hall, 4th edition, 2005.

[92] P. J. Flory, *Principles of Polymer Chemistry*, Cornell University Press, Ithaca, 1st edition, 1953.

[93] G. Moad and D. H. Solomon, *The Chemistry of Radical Polymerization*, Elsevier, 2nd edition, 2006.

[94] N. V. Tsarevsky and B. S. Sumerlin, *Fundamentals of Controlled/Living Radical Polymerization*, Royal Society of Chemistry, 2013.

[95] M. Pan et al., Chemical Society Reviews **42**, 5002 (2013).

[96] E. G. Cox, Review of Modern Physics **30**, 159 (1958).

[97] Y. H. Lu et al., Applied Physics Letters **94**, 122111 (2009).

[98] T. Wassmann, A. Seitsonen, a. Saitta, M. Lazzeri, and F. Mauri, Physical Review Letters **101**, 096402 (2008).

[99] J. R. Ferraro and K. Nakamoto, *Introductory Raman Spectroscopy*, Academic Press, Inc, 1994.

[100] L. Malard, M. Pimenta, G. Dresselhaus, and M. Dresselhaus, Physics Reports **473**, 51 (2009).

[101] M. Vandescuren, P. Hermet, V. Meunier, L. Henrard, and P. Lambin, Physical Review B **78**, 195401 (2008).

[102] L. B. Roberson et al., Journal of the American Chemical Society **127**, 3069 (2005).

[103] X. Wan et al., Chemistry of Materials **24**, 3906 (2012).

[104] H. Huang et al., Scientific Reports **2**, 1 (2012).

[105] I. C. Lewis and T. Edstrom, The Journal of Organic Chemistry **28**, 2050 (1962).

[106] L. D. Field, S. Sternhell, and H. V. Wilton, Tetrahedron **53**, 4051 (1997).

[107] X.-F. Li, L.-L. Wang, K.-Q. Chen, and Y. Luo, The Journal of Physical Chemistry C **115**, 12616 (2011).

[108] X.-F. Li, L.-L. Wang, K.-Q. Chen, and Y. Luo, Journal of Physics: Condensed Matter **24**, 095801 (2012).

[109] P. Ruffieux et al., ACS Nano **6**, 6930 (2012).

[110] Y.-C. Chen et al., ACS Nano **7**, 6123 (2013).

[111] C. Bronner et al., The Journal of Chemical Physics **140**, 024701 (2014).

[112] H. Söde et al., Physical Review Letters , 1 (2014).

[113] R. Denk et al., Nature Communications **5**, 4253 (2014).

[114] J. Neaton, M. Hybertsen, and S. Louie, Physical Review Letters **97**, 216405 (2006).

[115] J. M. Garcia-Lastra and K. S. Thygesen, Physical Review Letters **106**, 187402 (2011).

[116] E. Clar, *The Aromatic Sextet*, Wiley, London, 1972.

[117] I. Gutman, v. Tomović, K. Müllen, and J. P. Rabe, Chemical Physics Letters **397**, 412 (2004).

[118] Z. B. Maksić, D. Barić, and T. Müller, The Journal of Physical Chemistry A **110**, 10135 (2006).

[119] T. Wassmann et al., Journal of the American Chemical Society **132**, 3440 (2010).

[120] A. Konishi et al., Journal of the American Chemical Society **135**, 1430 (2013).

[121] E. Y. Andrei, G. Li, and X. Du, Reports on progress in physics. Physical Society (Great Britain) **75**, 056501 (2012).

[122] G. Buchs, *Local Modification and Characterization of the Electronic Structure of Carbon Nanotubes*, Phd thesis, University of Basel, 2008.

[123] D. Bercioux, G. Buchs, H. Grabert, and O. Gröning, Physical Review B **83**, 165439 (2011).

[124] A. Balatsky, I. Vekhter, and J.-X. Zhu, Reviews of Modern Physics **78**, 373 (2006).

[125] S. Wang, W. Wang, and N. Lin, Physical Review Letters **106**, 206803 (2011).

[126] S. Wang, W. Wang, and N. Lin, Physical Review B **86**, 045428 (2012).

[127] J. Tersoff and D. Hamann, Physical Review B **31**, 805 (1985).

[128] A. Bergvall and T. Löfwander, Physical Review B **87**, 205431 (2013).

[129] J. Perdew, K. Burke, and M. Ernzerhof, Physical Review Letters **77**, 3865 (1996).

[130] The CP2K developers group, http://www.cp2k.org.

[131] K.-i. Sasaki, K. Wakabayashi, and T. Enoki, Journal of the Physical Society of Japan **80**, 044710 (2011).

[132] S. Hamel, P. Duffy, M. E. Casida, and D. R. Salahub, Journal of Electron Spectroscopy and Related Phenomena **123**, 345 (2002).

[133] R. Stowasser and R. Hoffmann, Journal of the American Chemical Society **121**, 3414 (1999).

[134] M. D. S. Price et al., Physica Status Solidi B **250**, 2417 (2013).

[135] K.-T. Lam et al., Electron Device Letters **31**, 555 (2010).

[136] H. Sevinçli, M. Topsakal, and S. Ciraci, Physical Review B **78**, 245402 (2008).

[137] J. Cai et al., Nature Nanotechnology **9**, 896 (2014).

[138] C. Bronner et al., Angewandte Chemie **52**, 4422 (2013).

[139] J. Nelson, Current Opinion in Solid State and Materials Science **6**, 87 (2002).

[140] V. Mihailetchi, L. Koster, J. Hummelen, and P. Blom, Physical Review Letters **93**, 216601 (2004).

[141] F. Findeis et al., Physical Review B **63**, 121309 (2001).

[142] K. Kheng et al., Physical Review Letters **71**, 1752 (1993).

[143] M. Bayer, O. Stern, P. Hawrylak, S. Fafard, and A. Forchel, Nature **405**, 923 (2000).

[144] H. Söde, P. Ruffieux, A. Ferretti, and R. Fasel, ACS nano (2015).

[145] B. R. Nag, *Physics of Quantum Well Devices*, Springer Science, 2000.

[146] C. Latta et al., Nature **474**, 627 (2011).

[147] R. J. Warburton, Nature Materials **12**, 483 (2013).

[148] F. Léonard and a. Talin, Physical Review Letters **97**, 026804 (2006).

[149] M. Gajdos and J. Hafner, Surface Science **590**, 117 (2005).

[150] A. L. Yeyati, A. Martín-Rodero, and F. Flores, Physical Review B **56**, 10369 (1997).

[151] N.-T. Vu, a. Jakalian, and D. B. Jack, The Journal of Chemical Physics **106**, 2551 (1997).

[152] J. Sakamoto, J. van Heijst, O. Lukin, and a. D. Schlüter, Angewandte Chemie **48**, 1030 (2009).

[153] N. Abdurakhmanova et al., Carbon **77**, 1187 (2014).

[154] I. G. Hill and A. Kahn, Journal of Applied Physics **84** (1998).

[155] I. G. Hill, A. Rajagopal, A. Kahn, and Y. Hu, Applied Physics Letters **73** (1998).

[156] C. Shen, A. Kahn, and J. Schwartz, Journal of Applied Physics **89** (2001).

[157] J. Repp, G. Meyer, S. M. Stojković, A. Gourdon, and C. Joachim, Physical Review Letters **94**, 26803 (2005).

[158] X. Li, X. Wang, L. Zhang, S. Lee, and H. Dai, Science **319**, 1229 (2008).

[159] D. Basov, M. Fogler, a. Lanzara, F. Wang, and Y. Zhang, Reviews of Modern Physics **86**, 959 (2014).

[160] J. Hou and A. Zhao, Nano **1**, 15 (2006).

[161] L. Lafferentz et al., Science **323**, 1193 (2009).

[162] P. K. de Boer and R. A. de Groot, Americal Journal of Physics **67**, 443 (1999).

[163] C. Schwennicke, J. Schimmelpfennig, and H. Pfnür, Surface Science **293**, 57 (1993).

[164] M. Henzler, Surface Science **357-358**, 809 (1996).

[165] T. Brugger et al., Physical Review B **79**, 045407 (2009).

[166] B. Borca et al., Physical Review Letters **105**, 036804 (2010).

[167] S. Barja et al., Chemical Communications **46**, 8198 (2010).

[168] G. Hong et al., Nano Today **8**, 388 (2013).

[169] H. G. Zhang et al., Physical Review B **84**, 245436 (2011).

[170] M. Garnica et al., Nature Physics **9**, 368 (2013).

[171] A. K. Geim, Science **324**, 1530 (2009).

[172] S. Marchini, S. Günther, and J. Wintterlin, Physical Review B **76**, 075429 (2007).

[173] E. Sutter, D. P. Acharya, J. T. Sadowski, and P. Sutter, Applied Physics Letters **94**, 133101 (2009).

[174] Y. Niimi et al., Physical Review B **73**, 085421 (2006).

[175] S. Rousset, V. Repain, G. Baudot, Y. Garreau, and J. Lecoeur, Journal of Physics: Condensed Matter **15**, S3363 (2003).

[176] W. Ling et al., Surface Science **600**, 1735 (2006).

[177] B. Premlal et al., Applied Physics Letters **94**, 263115 (2009).

[178] L. Huang et al., Applied Physics Letters **99**, 163107 (2011).

List of Publications

Publications in Journals and Proceedings

- *Termini of Bottom-Up Fabricated Graphene Nanoribbons*, L. Talirz, **H. Söde**, J. Cai, P. Ruffeux, S. Blankenburg, R. Jafaar, R. Berger, X. Feng, K. Müllen, D. Passerone, R. Fasel and C. A. Pignedoli, The Journal of the American Chemical Society **135**, 2060 (2013).

- *Exciton-Dominated Optical Response of Ultranarrow Graphene Nanoribbons*, R. Denk, M. Hohage, P. Zeppenfeld, J. Cai, C. A. Pignedoli, **H. Söde**, R. Fasel, X. Feng, K Müllen, S. Wang, D. Prezzi, A. Ferretti, A. Ruini, E. Molinari and P. Ruffieux, Nature Communications **5**, 4253 (2014).

- *Graphene nanoribbon heterojunctions*, J. Cai, C. A. Pignedoli, L. Talirz, P. Ruffieux, **H. Söde**, L. Liang, V. Meunier, R. Berger, R. Li, X. Feng, K. Müllen and R. Fasel, Nature Nanotechnology **9**, 896900 (2014).

- *Electronic band dispersion of graphene nanoribbons via Fourier-transformed scanning tunneling spectroscopy*, **H. Söde**, L. Talirz, O. Gröning, C. A. Pignedoli, R. Berger, X. Feng, K. Müllen, R. Fasel and P. Ruffieux, accepted for publication in Physical Review B.

- *Structural and Electronic Characterization of Atomically Precise GNR Junctions*, T. Dienel, O. Gröning, S. Kawai, **H. Söde**, P. Ruffeux and R. Fasel, in preparation.

- *From Molecules to Ribbons: Length and Terminus Dependence of the Electronic Band Gap*, L. Talirz, **H. Söde**, J. Cai, P. Ruffeux, S. Blankenburg, R. Jafaar, R. Berger, X. Feng, K. Müllen, D. Passerone, R. Fasel and C. A. Pignedoli, in preparation.

- *Growth and Electronic Investigation of Medium Gap Graphene Nanoribbon*, **H. Söde**, L. Talirz, P. Shinde, C. A. Pignedoli, R. Berger, X. Feng, K. Müllen, R. Fasel and P. Ruffieux, in preparation.
- *Graphen Nanoribbon Heterojunctions via Partial Cyclodehydrogenation*, **H. Söde**, A. Ferreti, R. Berger, X. Feng, K. Müllen, R. Fasel and P. Ruffieux, in preparation.

Patents

- BASF SE, EP Patent: 2014077043 .

Talks

- *Bottom-up Fabrication and Electronic Properties of narrow Graphene Nanoribbons*, University of Zurich, Surface physics group seminar, Prof. Thomas Greber, 20. June 2012, Zurich, Switzerland.
- *Electronic Properties of atomically precise Graphene Nanoribbons*, molCHsurf, 10. June 2013, Bern, Switzerland
- *Electronic Properties of atomically precise Graphene Nanoribbons*, International Vacuum Congress / International Conference on Nanoscience and Technology, 10. September 2013, Paris, France
- *Electronic Properties of atomically precise Graphene Nanoribbons*, 12th International Conference on Frontiers of Polymers and Advanced Materials, 10. December 2013, Auckland, New Zealand
- *Intraribbon band gap variation in atomically precise graphene nanoribbon heterostructures*, Annual Meeting of the Swiss Physical Society, 30. June 2014, Fribourg, Switzerland
- *Intraribbon band gap variation in atomically precise graphene nanoribbon heterostructures*, 30th European Conference on Surface Science, 4. September 2014, Antalya, Turkey

Poster contributions

- *Bottom-up fabrication and electronic properties of graphene nanoribbons*, 26th International Winterschool on Electronic Properties of Novel Materials, 3. - 10. March 2012 Kirchberg, Austria

- *Electronic Properties of atomically precise Graphene Nanoribbons*, 6th Windsor Summer School, 14. - 26. August 2012, Windsor, United Kingdom
- *Electronic properties of atomically precise graphene nanoribbons*, PhD student symposium, 13. November 2012, Dübendorf, Switzerland
- *Electronic Properties of atomically precise Graphene Nanoribbons*, 27th International Winterschool on Electronic Properties of Novel Materials, 2. - 9. March 2013 Kirchberg, Austria
- *Band Gap Evolution and Termini of short Graphene Nanoribbons*, Workshop on Nanostructured Graphene, 21. - 24. May 2013 Antwerp, Belgium

Acknowledgments

About three and a half years ago I started my work at the nanotech@surfaces laboratory at the Swiss Federal Laboratories for Materials Science and Technology (Empa). This thesis reports on the results that I have obtained during time. However, it cannot express the long days spent in the laboratories, the struggles with and the maintenance of the measurement systems, discussions with fellow scientists and friends, the hope for good results, and the sadness and tiredness with each failed attempt. During the whole time I have been supported by many people. At this point I would like to express my thanks to the entire nanotech@surfaces group for being such an open and helpful working group that I always enjoyed working with. I am thankful to everyone who has supported me during my years as a student. In particular I would like to thank

Prof. Dr. Thomas Greber, for being my PhD supervisor. As an external PhD student, our interaction wasn't particular frequent, but he was always interested in my results and helpful by giving an outside view on my progress;

Prof. Dr. Roman Fasel, for giving me the opportunity to work on this fascinating research topic in his group;

Dr. Pascal Ruffieux for the supervision during all stages of this work. I have profited a lot from his broad knowledge in the field and his ideas;

Prof. Dr. Leonhard Grill, for accepting to be member the jury and evaluating my work;

Leopold Talirz, for the numerous simulations and discussions that have greatly helped the analysis of my experimental results;

Dr. Oliver Gröning, for helping me out whenever I had a problem with Igor Pro;

Dr. Shigeki Kawai, for the introduction to our nc-AFM;

My parents, for their never-ending encouragement and ongoing support.

Zürich, January 20, 2015

Hajo Söde